ALFRED-WEGENER-INSTITUT
HELMHOLTZ-ZENTRUM FÜR POLAR- UND MEERESFORSCHUNG

Universität Bremen

Analysis and interpretation of vibroseis data from Kohnen Station, Antarctica

Masterthesis

Rebecca Schlegel
Matrikel Nr.: 2984995

Contact: Rebecca Schlegel
schlegel-rebecca@gmx.de
University Bremen

1. Supervisor: Prof. Dr. Olaf Eisen
2. Supervisor: PD Dr. Karsten Gohl

Submitted: July 15th, 2016

Abstract

In 2011/12 a shallow reflection seismic survey was carried out at Kohnen Station, East Antarctica. A small electrodynamic vibrator source (ElViS) was used to generate seismic waves to determine the physical properties of firn and shallow ice. Depth converted seismic data could be compared to a nearby ice core, radar and wide-angle seismic measurements. Possible reflections are superimposed by strong diving and surface waves, excited by the ElViS. However, a velocity-depth profile was obtained by the analysis of diving waves. Elastic moduli of firn were calculated using diving-wave velocities and densities derived from ice-core measurements. These elastic moduli, as well as the velocities were compared to elastic moduli derived from a finite element algorithm, based on ice-core data. The difference between field derived values and the model values were found to be within the uncertainty range.

Neither the raw nor the processed data shows any signs of englacial reflections. However, the stacked data show aligned high amplitude signals, which were found to be caused by Rayleigh waves. Additionally, a high amplitude signal can be seen at 1.63 s two-way traveltime (TWT). The bed reflection causing this high amplitude signal could be ruled out. The bed reflection for this area was determined by wide-angle data at 1.44 s TWT, corresponding to 2700 m depth which is in agreement with the depth found in radar and ice-core data (Diez, 2013). The calculations in this work suggest that the signal in 1.63 s TWT is possibly caused by a Rayleigh wave that is reflected at nearby containers, but further investigations are necessary.

Results demonstrate the adaptability of the ElViS technique to determine physical properties of firn which highlights the potential of this novel technique to be used in future glaciological research. The results presented here may facilitate improvements for further studies.

Zusammenfassung

Der Anstieg des Meeresspiegels ist ein häufig thematisiertes Thema der Gegenwart. Das zukünftige Verhalten der Eismassen, und der daraus folgende Meeresspiegelanstieg, wird anhand von numerischen Modellen berechnet. Das Ausdünnen der Gletscher und Eisschilde, sowie die Rheologie und das basale Gleiten sind bisher noch wenig erforschte Faktoren. Dies macht eine differenzierte Vorhersage unmöglich. Aufgrund der Unzugänglichkeit sind Messungen an der Basis von Eisschilden und Gletschern unmöglich. Physikalische Eigenschaften von Eis und Firn können unter anderem anhand von Eiskernanalysen ermittelt werden. Diese Messung ermöglicht eine höhere vertikale Auflösung, stellt jedoch nur eine Punktmessung dar. Eine höhere räumliche Auflösung kann mit Hilfe von geophysikalischen Methoden, wie Seismik und Radar, erlangt werden (Cuffey and Paterson, 2010).

Eine reflexionsseismische Messung wurde in der Saison 2011/12 an der Kohnen Station, in der Ostantarktis, durchgeführt. Ein leichter (130 kg) elektrodynamischer Vibrator (ElViS) mit einer Quellsignallänge von 10 s, wurde zur Anregung von P- als auch S-Wellen verwendet. Zwei senkrecht zueinander orientierte Messprofile wurden aufgenommen. Das Profil mit der Länge 420 m, und mit 44 Schusspositionen wurde parallel zur Eisscheide orientiert. Das senkrechte Profil hat eine Länge von 115 m und enthält 56 Schusspositionen. Die beiden Profile unterscheiden sich vor allem in der Anordnung der Schüsse zu den Geophonen. In dem senkrechten Profil wurde nur innerhalb der Geophonlinie geschossen, wobei das parallele Profil zusätzlich Schusspositionen außerhalb der Geophonlinie aufweist. Diese unterschiedliche Anordnung konnte in den Daten gesehen werden. Schüsse mit geringem Abstand zu den Geophonen weisen einen hohen Signalanteil von Oberflächenwellen, Tauchwellen und parasitärer Resonanzen auf. Dem entsprechend weist das senkrechte Profil mehr Rauschen auf, als das parallele Profil, das mit größeren Abständen aufgenommen wurde.

Das starke Signal der Oberflächenwellen und Tauchwellen überlagert mögliche Reflexionssignale. Die Anwendung verschiedener Frequenzfilter, F-k Filter und der K-L Transformation führte zu keinem zufriedenstellenden Ergebnis. Reflexionen konnten nicht sichtbar gemacht werden. Die gestapelten Daten weisen bei bestimmten Laufzeiten hochfrequente Signale auf, die sich vergleichbar zu Reflexionen horizontal ausrichteten. Eine vorläufige Interpretation als Reflexionssignal wurde widerlegt. Der Ursprung dieses Signals wurde in der Oberflächenwelle, genaugenommen der Rayleighwelle bestimmt. Ein zusätzliches Problem während der Datenbearbeitung war, das starke Signal der parasitären Resonanz. Dieses äußert sich durch ein sichtbares Nachschwingen im Seismogramm. Verursacht wird dieses Signal durch Phasensprünge und Sensibilitätsvariationen in der Übertragungsfunktion des Geophons. Hintergrund ist, dass ein vertikal orientiertes Geophon nicht nur vertikale Bewegung aufnimmt, sondern auch Horizontalbewegung. Dieses Signal konnte zum Teil anhand von Frequenzfiltern entfernt werden. Spuren mit einem geringeren Abstand als 30 m zu den Schusspositionen wurden gelöscht um das Signal-Rausch-Verhältnis zu verbessern. Des Weiteren ist bei einer Laufzeit von 1.63 s ein hoch amplitudes Signal zu sehen. Die Eisunterkante befindet sich übereinstimmend in Radar, Eiskern und Weitwinkel Daten in einer Tiefe von 2700 m was unter Anbetracht der seismischen Geschwindigkeiten an der Kohnen Station einer Laufzeit von 1.44 s entspricht (Diez, 2013). Fehler in der Aufzeichnung konnten ausgeschlossen werden. Das Signal bei einer Laufzeit von 1.63 s wurde möglicherweise durch die Reflexion einer Rayleighwelle an naheliegenden Containern generiert. Weitere Untersuchungen sind jedoch notwendig um diese Interpretation zu bestätigen.

Tauchwellen konnten verwendet werden um anhand einer Inversion ein Geschwindigkeits-Tiefen-Profil zu errechnen. Tauchwellen werden durch den stetigen Dichteanstieg mit zunehmender Tiefe in Firn verursacht. Diese Dichtedaten aus dem Eiskern an der Kohnen Station können anhand von Formeln, definiert von Kohnen (1972) und Diez et al. (2013), in seismische Geschwindigkeiten umgerechnet werden. Zusätzlich wurden Komponenten des elastischen Tensors in vier verschiedenen Tiefen des Eiskerns berechnet. Diese Komponenten lassen sich ebenfalls in seismische Geschwindigkeiten umrechnen. Der Vergleich dieser Geschwindigkeiten zeigt geringe Abweichungen zwischen den Geschwindigkeiten aus den Komponenten und den Tauchwellen. Eine große Differenz ist zwischen den Geschwindigkeiten aus den Tauchwellen und den transformierten Dichten aus P-wellen Geschwindigkeiten zu beobachten. Dies zeigt die begrenzte Brauchbarkeit der Formel. Berechnete elastische Moduln aus den Komponenten und der Tauchwellengeschwindigkeit zusammen mit der Kerndichte, stimmen gut überein.

Anhand dieser Arbeit konnte gezeigt werden, dass physikalische Eigenschaften von Firn mit Hilfe eines Vibrators dargestellt werden können. Reflexionen innerhalb von Firn und Eis konnten nicht sichtbar gemacht werden. Dies kann zwei Gründe haben: Entweder ist der Impedanzkontrast nicht groß genug um Reflexionen hervorzurufen, oder das starke Signal der Tauch-, Oberflächenwellen und parasitären Resonanzen überlagert schwache Reflexionen. Ein größerer Abstand zwischen Schuss und Geophonlinie könnte bei zukünftigen Messkampagnen die Datenprozessierung erleichtern und Reflexionen sichtbar machen.

Declaration acc. to § 10 Paragraph 11 Common Part of the Master Examination Regulations

I hereby declare that I wrote my Master Thesis independently and that I did not use other sources and auxiliary means than the ones indicated. This Master Thesis is not submitted in another examining procedure.

Bremen, 15. July 2016

Contents

1. Introduction

The temperature increase since the pre-industrial era is currently one of the most concerning issues in society. A sea level rise of 0.53–0.98 m is expected by 2100 (RCPP85), which will induce coastal floods in inhabited areas. Global sea level change is sensitive to thermal expansion of the oceans and the reduction of land-based ice mass and is thus an indicator for climate change (Mitrovica et al., 2001). As a result of global warming, the mean sea level has increased since 1993 by up to 3 mm per year (Church et al., 2013). In the event of total melting of the Antarctic and Greenland Ice Sheet, the sea level would rise by about 63.5 m due to their immense size (Cuffey and Paterson, 2010; Meier et al., 2007; Pritchard et al., 2012; Raper and Braithwaite, 2013).

The future behavior of ice sheets and glaciers to changing climate is predicted by numerical modelling. The extent and magnitude of thinning of glaciers and ice shelves (floating part of a glacier) as well as their rheology and basal sliding are poorly understood and predictions of glacier evolution are impossible to make without further knowledge. Direct measurements of conditions at the base are impossible due to the inaccessibility of the base (Pritchard et al., 2012). Detailed information about ice properties and englacial structures are achieved by drilling and analyzing ice cores. This is a time, cost and labor consuming method that samples only one point with a very high vertical resolution. A higher spatial coverage can be achieved by the use of geophysical methods like seismics and radar. Seismic reflections represent an impedance contrast, i.e. a change in ice properties. From these changes, information about englacial structures and a velocity-depth profile can be received. In addition, the first breaks of diving waves can be analyzed. The inversion of diving waves enables a velocity-depth profile to be derived, but gives no information about englacial structures. Reflections in radar data and thus changes in electromagnetic impedance provide information about ice properties. The combination of seismic and radar data enables the identification of properties which cause impedance contrasts (such as anisotropy) and the tracing of reflectors over a huge area. By comparing reflections with ice-core data, the age of these reflectors can be determined. In contrast to radar waves the characteristics of seismic waves enables them to penetrate through liquid media, such as through a temperate bed or a water column beneath an ice shelf (Cuffey and Paterson, 2010; Diez et al., 2013).

The seismic method has been used on ice since the early 20th century. Seismic data reveals information about ice thickness, internal structures (melt layers, annual layers, lenses and deformation structures), bed properties (lithology, frozen or temperate beds) and properties of firn and ice. The constant densification of firn and ice impedes the detection of reflections. Firn, which acts like a weathering layer, demands for a detailed velocity profile.

New possibilities for deriving the structural information of firn and ice rose with the first usage of a vibroseis source on ice in 2011. This new technique emits a sweep instead of an impulse, enables high fold measurements which improves the detection of reflections in firn and ice. A vibroseis survey took place in 2011/12 at Kohnen Station in East Antarctica.

This thesis represents a pilot study to evaluate the adaptability of a vibroseis measurement to resolve englacial structures and to investigate physical properties of firn and ice. Structures within the firn pack reveal information about the past mass balance and contribute to the understanding of the firn densification process. The assignment of reflections to a certain depth enables joint interpretation of seismic, radar and ice-core data. For the time-depth conversion

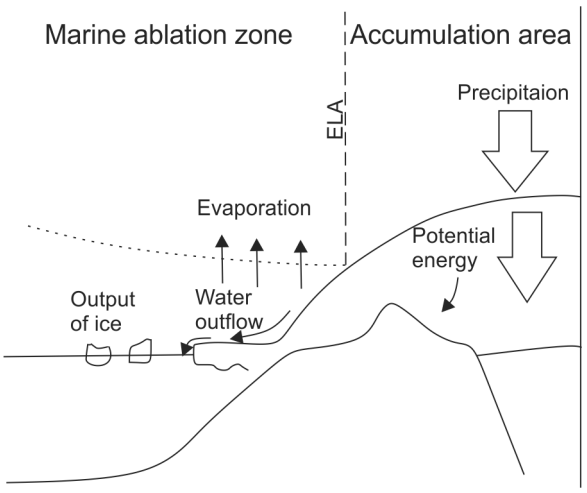

Figure 1.1.: Simplified schematic drawing of the mass and energy system in an ice sheet in Antarctica (Modified after Nelson, 2010).

of seismic data the subsurface velocity model is crucial. Therefore, the determination of seismic velocities is an essential step in dealing with seismic data. So far, an ice core was necessary to detect ice properties and receive detailed information about velocities with depth. A measurement unattached to an ice core would be less time, labor and cost consuming (Cuffey and Paterson, 2010; Diez et al., 2013).

1.1. Ice properties

The state of a glacier (growing or thinning, advancing or retreating) is determined by mass gains, mass loss and a dynamic component (transport of ice) by the glacier itself. The equilibrium line altitude (ELA) is located between the accumulation and ablation area (Figure 1.1). At the ELA the annual accumulation is equal to the annual ablation. The mass balance of a glacier or an ice sheet is calculated from mass losses and gains.

A glacier thins, as soon as the ablation exceeds the accumulation, while a growing glacier has a net mass input (Nelson, 2010). The flow velocity of a glacier depends on the driving force (downslope component of gravitational force) and the resisting force (drag at the margins and the bed of the glacier). The driving stress is a function of the ice thickness and the surface gradient, while the drag on the bedrock depends on the topography of the bedrock.

This thesis evaluates and discusses the propagation of seismic velocities in firn and ice. Seismic waves in firn and ice are mainly influenced by the distribution of density, temperature and anisotropy within the ice and firn. Therefore the following subchapters discuss the densification of snow to ice and the anisotropy in ice briefly. The temperature distribution is not considered in this thesis and therefore not further mentioned.

1.1.1. Densification of snow into ice

The amount of mass input depends on geographical and climatic factors. Snow layers are deposited on layers of previous years. Under appropriate conditions these layers can transform into ice (Nelson, 2010).

During the transformation process of snow into ice an intermediate material evolves, which is called firn. The distinction between snow and firn is still part of an ongoing scientific debate. The first definition of firn was wetted snow that has survived one summer without transforming into ice. Nowadays the customary definition is that snow is material that has

not experienced a transformation, while firn is material that has survived one melt season, being in an intermediate stage of transformation (Cuffey and Paterson, 2010; Nelson, 2010).

The firn densification process is divided into four different stages (Klikauer, 2016) according to their critical densities (Figure 1.2). The load of the overlying material is assumed to be the cause for densification, whereas melting in the dry snow zone is negligible, it is comparable to the hot pressing process of ceramics and metals (Arnaud et al., 2000). The whole process of densification can be described by the thermodynamic principle of free-energy reduction. The following stages introduce the densification effect of dry snow (without water) into ice.

The first stage of transformation is described by densities from the snow density (ρ_{snow}) to the first so-called critical density (ρ_{crit1}) of $550\,\mathrm{kg\,m^{-3}}$ (Benson, 1962; Herron and Langway, 1980). A maximum packing of idealized spherical grains is reached at the ρ_{crit1} by settling and rearrangement. The rounding of the grains is driven by sublimation and surface diffusion until the total surface area is reduced (which reduces the free energy) (Arnaud et al., 2000). Theoretically a density of $550\,\mathrm{kg\,m^{-3}}$ is associated with a porosity of 40 %, while Stanikova et al. (2015) stated that a porosity of 40 % is not realistic, whereas a porosity of 37 % has been achieved by intensive jarring in lab.

In the second stage plastic deformation and recrystallization increases the potential for viscous-plastic flow, melting and volume diffusion. Thereby, the neck between molecules grows with time, until the system is in an equilibrium. Grain boundary sliding is negligible in this stage. The mechanism of grains growing together and the elimination of pore space, which maximizes the contact area and reduces the porosity, is more time consuming than the first densification stage (Arnaud et al., 2000; Bader, 1960; Benson, 1962; Herron and Langway, 1980; Hobbs, 1968).

At the beginning of stage three with the critical density (ρ_{crit2}) of $730\,\mathrm{kg\,m^{-3}}$ a decrease in densification rate is observed. Here the pore space filled with atmospheric air exists as connected channels. Increased stresses enhances ice deformation and ice creep, which separates the pore space and creates isolated, closed off air bubbles (Cuffey and Paterson, 2010; Goujon, 2003; Herron and Langway, 1980).

Stage four is described by the critical density (ρ_{crit3}) of $830\,\mathrm{kg\,m^{-3}}$ and the density increase by bubble compression in ice. The material is defined as ice at a density of $830\,\mathrm{kg\,m^{-3}}$ (Cuffey and Paterson, 2010; Herron and Langway, 1980). The continuous densification process causes a continuous but non-linear increase in density with depth, as illustrated in Figure 1.2.

Depending on the topographic region, air temperatures might exceed the melting point and cause melting of snow. Meltwater then percolates into deeper layers and refreezes again. These ice lenses, layers or glands can contain a different density than the surrounding material (densification with water).

The exact determination of the Firn-Ice Transition zone (FIT), more precisely the bubble close-off, is part of recent research. The air bubbles below the FIT are sealed off from the atmosphere and can be used for climate reconstructions (Arnaud et al., 2000). The determination of a (predicted) density-depth relationship as well as a depth-age relationship is possible with a known accumulation rate, temperature and initial snow density (Herron and Langway, 1980).

1.1.2. Anisotropy in ice

Under natural conditions on earth ice is a hexagonal, anisotropic crystal with the basal plane orientated perpendicular to the ice crystal's c-axis. In an isotropic medium properties are the same when measured from any direction, in contrary to an anisotropic medium, where properties vary, depended on the direction (Okrusch and Matthes, 2010). Anisotropy in ice is used to describe the ice-crystal rotation of the c-axes, due to internal stresses. The c-axis rotates

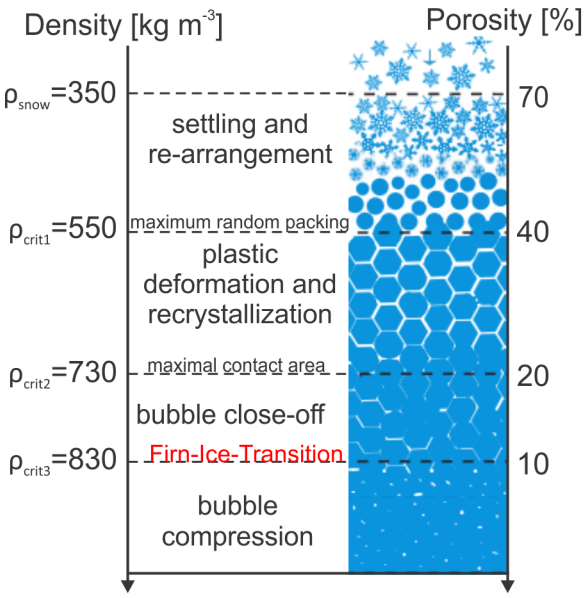

Figure 1.2.: Different stages of densification including the different critical densities and porosities (Modified after Klikauer, 2016).

towards the compression axis, perpendicular to a shear direction, away from the tension axis. Basal drag, controlled by friction is, for most glaciers, the largest resisting force. The basal shear stress is therefore decreasing with distance to the bed. The ice flow of a glacier frozen to the bed is mainly determined by internal deformation. The viscosity, describing the degree of internal deformation, is dependent on many factors, like the crystal orientation fabric (COF). Different COF distributions can evolve depending on the stress regime. Information about the crystal anisotropy distribution is mainly provided by COF measurements from ice cores (Cuffey and Paterson, 2010; Diez et al., 2014; Montagnat et al., 2014).

1.2. State of the art

Over the period of approximately 100 years explosives were the utilized seismic source, either by the detonation of a cord on the surface or by deploying charges in drilled holes (Diez et al., 2013; Eisen et al., 2015). Even though the vibrator seismic (vibroseis) source was used for land seismic exploration since the 1970s, it was first considered unfeasible on ice, since the instantaneous forces and energy are low. It was assumed that these signals would be too weak to penetrate into deeper layers of the ice, particularly in Antarctica, where the firn layer is typically 50–150 m thick (Diez et al., 2013; Eisen et al., 2015). Reflections in ice and firn have been resolved for the first time using vibroseis data in 2011. (Diez et al., 2013, 2014; Eisen et al., 2015; Polom et al., 2014).

The limited bandwidth of the vibroseis signal is a disadvantage compared to the explosive source. Explosive signals can contain very high frequencies and waves that can penetrate to the ice-bedrock interface. The penetration depth of a vibroseis signal is limited but the repeatability of the signal enables a high-fold stack of the signals, and thus, an improvement of the signal-to-noise ratio (SNR). For the detectability of reflections it is of advance to have less diving wave generation of the vibrator compared to the explosive source (Eisen et al., 2010; Kearey et al., 2002; Polom et al., 2014).

In the following, effects of densification on seismic velocities and thus challenges of seismics in ice are discussed. Moreover, a brief introduction on the results of the first vibroseis

measurements on ice is given.

1.2.1. Densification effect on velocities

Seismic velocity is mainly influenced by density and elastic moduli. The acquisition accuracy of a velocity-depth profile with reflection seismics is limited to the number of reflections. Additional to the continuous density and thus velocity increase with depth, porous firn in the upper meters of an ice sheet acts like an acoustic waveguide or trap for seismic energy transmission (Eisen et al., 2010; Picotti et al., 2015), causing a high attenuation and bending of the ray path (Eisen et al., 2015; Polom et al., 2014). The P- and S-wave velocities for firn and ice are listed in Table 1.1.

Table 1.1.: Range of velocity in firn and ice. (Dewart, 1970; Polom et al., 2014)

	v_p $[\mathrm{m\,s^{-1}}]$	v_s $[\mathrm{m\,s^{-1}}]$
Firn	500–3000	<1700
Ice	3000–3800	1700–1900

A detailed velocity-depth profile can be derived from measured densities along an ice core. Robin (1958) and Kohnen (1972) postulated formulas to calculate P-wave velocities from measured ice-core densities. Diez et al. (2014) introduced a relationship between density and the S-wave velocity. These calculated velocities are benchmark to evaluate results from other methods. Robin (1958) stated the following empirical formula with a linear relation between density ρ and P-wave velocity v_p of snow and ice:

$$\rho(z) = 0.221 \cdot 10^{-4} v_p(z) + 59 \tag{1.1}$$

This formula is only adaptable to a density higher then $580\,\mathrm{g\,cm^{-3}}$. An improved empirical relation in density and P-wave velocity was stated by Kohnen (1972). Here the P-wave velocity of pure ice $v_{p,ice}$ is incorporated into the formula :

$$\rho(z) = \frac{\rho_{ice}}{1 + [(v_{p,ice} - v_p(z))/2250\ \mathrm{m\,s^{-1}}]^{1.22}} \tag{1.2}$$

Diez et al. (2014) stated the following relation between density and S-wave velocity v_s of ice. Again the S-wave velocity $v_{s,ice}$ of pure ice is incorporated:

$$\rho(z) = \frac{\rho_{ice}}{1 + [(v_{s,ice} - v_s(z))/950\ \mathrm{m\,s^{-1}}]^{1.17}} \tag{1.3}$$

where $\rho(ice)$ is in the unit of $\mathrm{kg\,m^{-3}}$ and $v_{p,ice}$ as well as $v_{s,ice}$ are in the unit of $\mathrm{m\,s^{-1}}$. Kohnen (1972) suggested $\rho_{ice} = 915\,\mathrm{kg\,m^{-3}}$.

1.2.2. Experience with seismics on ice

Since the density is increasing with depth, explosives are deposited in 10–20 m depth during explosive measurements, to reach an area of higher density and thus overcome signal attenuation. This advanced measurement setup improves the penetration of waves and improves the detection of the ice-bedrock interface.

Diez et al. (2013) and Picotti et al. (2015) used the arrivals of diving waves and surface waves to calculate velocity-depth profiles applying the Herglotz-Wiechert inversion. However, statements about structures in the firn and ice cannot be made by this inversion due to the velocity gradient found in firn (Bormann, 2002; Diez et al., 2013; Kearey et al., 2002; Picotti et al., 2015).

Vibroseis measurement on Colle Gnifetti in 2010

In 2010 a measurement with a vibrator source generating P and SH waves took place on the glacier saddle Colle Gnifetti on the border between Italy and Switzerland. The study results are briefly summarized below, for further information see Diez et al. (2013, 2014); Polom et al. (2014).

Colle Gnifetti is often used for methodological tests, due to its comparability of physical properties with ice in polar regions. Preceding the vibroseis measurement an ice core was drilled in 2008 and a seismic impulse source system (SISSY) and radar measurements were performed to evaluate the joint investigation of radar and seismic method.

The SISSY generates strong diving waves which overlay possible signals of englacial and bedrock reflections. In contrast, the processed vibroseis seismogram from Colle Gnifetti shows the arrival of diving and surface waves but not as strong as in the seismogram of the impulse source. Additionally, clear FIT reflections and englacial stratigraphy are visible within firn and ice. The ice-bedrock interface in 62 m depth is determined using ice-core data. Furthermore, the same depth of the interface was derived from SH-wave data (vibrator source), which is in good agreement with the ice core data. In contrast, the bedrock reflector depth derived from the P wave is 6 m too shallow (Diez et al., 2013, 2014; Polom et al., 2014).

Reasons for the deviation in bedrock depth

Diez et al. (2013) discuss reasons for the deviation in depth, such as the effect of lateral inhomogeneities and anisotropy due to variations in COF. The assumption of the occurrence of anisotropy as a possible cause of depth deviations was underpinned by the occurrence of reflections without significant density variations. This leads to the assumption that reflections in this depth interval are caused by changes in the seismic velocity, due to changes in elastic properties. Hence, changes in the COF or changes caused by the pore close-off at the FIT could be possible reasons for reflections without significant density variations (Diez et al., 2013).

The wavefronts in an anisotropic media are no longer spherical. Therefore, the traveltimes for different incoming angles depends on the longer travel paths due to increasing offsets and on the angle of the velocities. The SH-wave velocity is minimal for a SH wave travelling parallel to the c-axis of an ice crystal, whereas the P-wave velocity is maximal in this direction. Waves traveling perpendicular to the c-axis increase the SH-wave velocity by 6 % and decrease the P-wave velocity by 4 %. Diez et al. (2014) stated that information about the anisotropic fabric of the firn and ice can be derived by the use of P- and SH-wave data. If anisotropy occurs, the assumption of stacking velocity for the depth-conversion leads to incorrect depth values. The difference of stacking velocities and RMS velocities vary between the different wave types, thus a difference in reflector depth for different wave types is observed. An additional parameter in the velocity analysis, the Thomsen parameter, is used to describe for the anisotropy in a medium (Tsvankin, 1997). In case of the Colle Gnifetti the calculated Root Mean Square (RMS) velocity, taking anisotropy into account, differs from the stacking velocity by 7 % for the P wave and by 1 % for the SH wave (Diez et al., 2014).

The traveltime difference of a bended ray path (Figure 1.3, blue line) due to the density gradient in firn and a straight ray path (Figure 1.3, green line), which could have explained the depth offset, was stated to be negligible (Diez et al., 2014). The difference is less than 5 % and is decreasing with depth (Anja Diez, pers. comm.).

Vibroseis measurement at Halvfarryggen in 2010/11

Hofstede et al. (2013) compared explosive seismics and vibroseis measurements at Halvfar-

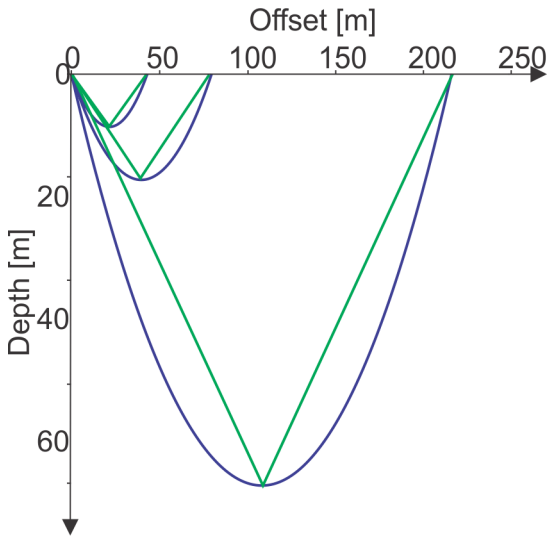

Figure 1.3.: Illustration of the difference of bended (blue) and straight (green) raypath (Anja Diez, pers. comm.).

ryggen, a 910 m thick local ice dome, in 2010/11. The englacial reflectors, detected in the explosive source data are not visible in the vibroseis data. The analysis of the frequency spectrum of the reflections showed a high frequency content of the englacial reflections. The frequency bandwidth of the vibroseis sweep was 10–100 Hz. Bandpass filtered explosive data, with a similar bandwidth like the sweep, showed only one englacial reflection. A wider bandpass filter of 10–400 Hz included clear englacial reflections. Less englacial reflections are visible, the lower the second cut-off frequency. Hofstede et al. (2013) concluded that with a sweep up to 300 Hz the same reflectors would presumably be detectable.

1.3. Scientific objectives

The primary aim of this study is to derived a velocity-depth profile for the whole firn column using seismic data from Kohnen Station, East Antarctica. Elastic moduli can be calculated based on these velocities and densities, derived from the ice core. The elastic moduli will then be compared to elastic moduli calculated by an finite element algorithm. Deviations indicate inhomogeneities or anisotropy.

The combination of seismic reflection data in firn and the availability of an ice core is unique. Therefore the second study aim is the detection of reflections in firn via seismic data. These reflections can probably be correlated to anomalies in the ice core which improves the understanding for reflections in firn.

The detection of structures in firn introduces the next aim: the accuracy of depth determination of reflectors. Firn acts like a weathering layer, causing a high attenuation and bending of the rays. This can result in deviations in velocities, and thus an erroneous depth-conversion. A precise velocity-depth profile over the firn layer will reduce the errors in ice-thickness calculations. The elimination of such deviations is of special importance since drilling of an ice core down to the ice-bedrock interface requires extensive planning and funding. Additionally, the relation of density and velocity postulated by Kohnen (1972) and Diez et al. (2014) will be evaluated.

1.4. Thesis structure

The following five Chapters are structured as followed:
Chapter 2 describes the physical basis with focus on seismic wave propagation, the system of vibroseis source and the method used to derive physical propertied from an ice core. Details of the data acquisition at Kohnen Station and a brief data description are given in Chapter 3. From there on the thesis focusses on two different aspects. First the detection and evaluation of seismic events and second the inversion of diving waves. The method of both can be found in the second part of Chapter 3.
The evaluation of events seen in the stack, as well as results of the data processing are shown in Chapter 4. Furthermore results of diving-wave inversion are displayed. This contains the comparison of velocities and elastic moduli calculated by diving wave inversion velocities and densities derived from X-ray Computed Tomography (XCT) as well as values derived by a finite element algorithm (FEA), under the assumption of an isotropic medium.
The chapter presenting the results of this thesis is followed by the interpretation ot these results (Chapter 5). Here reasons for the lack of reflections are discussed. Furthermore, the evaluation of possible reasons for high amplitude events are presented. The second part of the interpretation focusses on the results of the diving-wave inversion. The validity of an isotropic medium is discussed.
The thesis concludes with a conclusion and an outlook for further studies. A list of abbreviations and variables can be found in the Appendix, furthermore they are explained when they appear for the first time.

2. Theoretical background

The seismic method has many different application areas, among others, the determination of changes in lithology with depth. The principle of changing lithology can also be applied in the field of glaciology to determine ice thicknesses (Diez et al., 2013; Eisen et al., 2010; Telford et al., 1990).

The seismic measurement set up consists of a receiver and a source. Parts of the emitted waves are reflected to the surface and recorded by geophones or seismometers. Under the assumption of a known velocity, the depth down to which the waves propagated can be calculated by means of the TWT (Telford et al., 1990).

2.1. Seismic waves

The seismic wave field consists of waves propagating through the body of a medium, called body waves, and waves propagating along the surface, called surface waves (Biot and Lowrie, 2007). The principle of both will be explained in the following:

Body waves can be divided into P waves, also called longitudinal or compressional waves, and S waves, also called transversal or shear waves. As the names imply, the P wave has a particle motion in the direction of wave propagation (longitudinal). The S waves particle motion is perpendicular (transverse) to the direction of wave propagation, here two different types of particle motion can be observed. The particle motion (Figure 2.1) of the horizontally shear waves (SH wave) oscillates purely in the horizontal plane, while the vertically shear waves (SV wave) induces an up- and downward particle oscillation in the vertical plane (Bormann, 2002). The velocity of P and S waves depends on density and elasticity of the medium. The P-wave velocity v_p is higher than the S-wave velocity v_s ($v_p > v_s$), resulting in the name assignment primary and secondary wave. The P-waves can propagate through all three aggregate states, while the S-wave cannot propagate through liquids or gases, since they cannot be sheared (Biot and Lowrie, 2007). The variables influencing the velocity are given in Chapter 2.3.

Surface waves can be divided into Rayleigh and Love waves, which both have different directions of polarization. The particle motion of Rayleigh waves is elliptical in a plane perpendicular to the surface, containing the direction of propagation (Figure 2.2 (A)). The propagation is along a free surface or along a boundary of two dissimilar solid media. The velocity of propagation is lower than the S-wave velocity while the amplitude is decreasing exponentially with depth.

In contrast, the polarization of Love waves is parallel to the free surface and perpendicular to the direction of wave propagation (Figure 2.2 (B)). Love waves are generated if the shear wave velocity of the surface layer is lower compared to the underlying layer. The velocity of the Love wave is intermediate between the S-wave velocity of the deeper layer and the surface layer, but in general higher than the Rayleigh wave velocity (Kearey et al., 2002; Sheriff and Geldart, 1995).

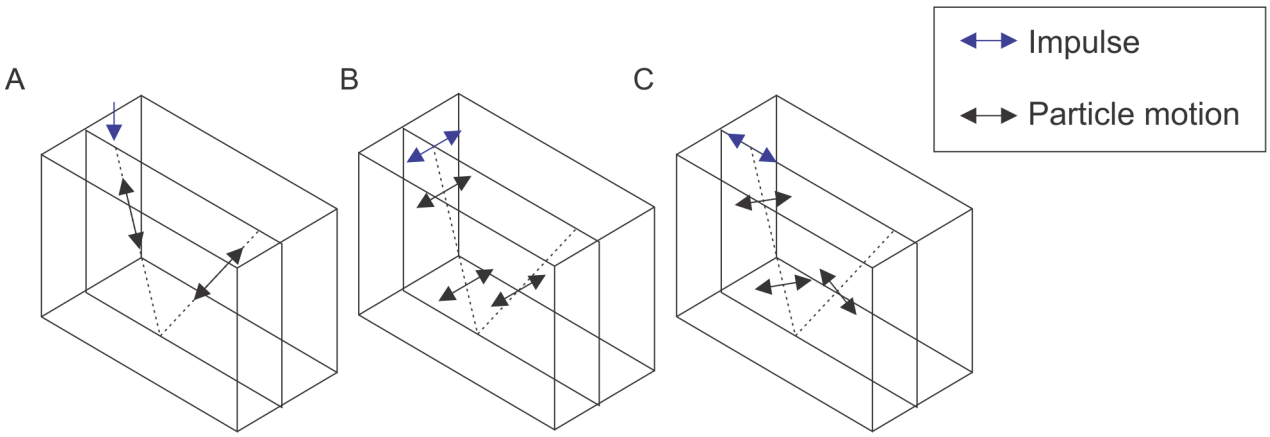

Figure 2.1.: Description of the particle motion and impulse direction: A) Particle motion of the P wave, B) of the SH wave and C) of the SV wave. The P wave propagates parallel to the direction of propagation, with particles being moved back and forth. The S wave particle motion is perpendicular to the direction of propagation, with the horizontal polarized S wave oscillating in the horizontal plane and vertical polarized S waves oscillating up and down in the vertical plane (Modified after Tatham and McCormack, 1991).

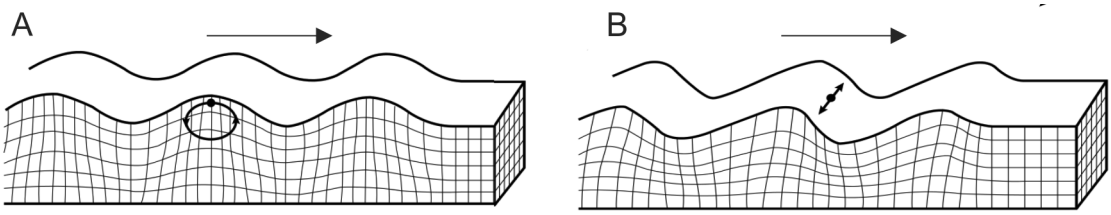

Figure 2.2.: Different types of particle motion for A) Rayleigh wave and B) Love wave. The particle motion of Rayleigh waves is elliptical in a plane perpendicular to the surface, containing the direction of propagation. The particle motion of Love waves is parallel to the free surface and perpendicular to the direction of wave propagation (Modified after Kearey et al., 2002).

Both wave types are classified as groundroll, a signal that can be characterized by coherent, linear and dispersive nature. Dispersive means that the wave velocity is dependent on the frequency. The higher the frequency, the lower the velocity of the wave. Groundroll often superimposes the signal of reflections. It can be identified in the seismogram by a straight alignment, similar to those of reflections. In contrast to reflections the apparent velocity of groundroll is lower and the envelope decays slowly with depth (dos Santos and Porsani, 2013; Kearey et al., 2002; Porsani and Silva, 2010; Sheriff and Geldart, 1995).

2.2. Wave propagation in an isotropic medium

Huygens' principle states that every single point of a wave can be considered as a new source of waves. Accordingly with a known wavefront position at time t_1 the location of the wave after a certain time difference can by calculated by means of the velocity (Telford et al., 1990).

The wave propagates through different lithologies with different elastic properties. Abrupt changes in impedance, e.g. at a lithological boundary, cause the wave energy to be partly reflected and refracted. In glaciology such a contrast can be the ice-bedrock interface. The

impedance Z is defined by:

$$Z = \rho \cdot v \tag{2.1}$$

where ρ is the density of the medium and v the seismic velocity of the medium. Therefore, a change in impedance can be caused by a change in density and/or velocity, i.e. elastic properties.

The reflected wave energy propagates back to the surface (green ray path in lower part of Figure 2.3). The law of reflection states that the angle of incidence equals the angle of reflection.

The refracted wave energy in contrast propagated into the next layer. Snell's law describes the ratio of change in the diffusion angle according to the change in properties of the material, as seen in the following equation:

$$\frac{\sin \Theta_1}{v_1} = \frac{\sin \Theta_2}{v_2} = p \tag{2.2}$$

where Θ_1 is the angle of incidence, Θ_2 the angle of refraction with v_1 and v_2 as the velocities in the upper and lower media and p is the constant ray path parameter.

If the angle of refraction Θ_2 reaches 90°, the so called critically refracted wave travels along the interface of the two media (red ray path in the lower part of Figure 2.3). The angle of incidence, in this case referred to as critical angle, providing an angle of refraction (90°), can be calculated by Equation 2.2 and known velocities for the upper and lower media.

Diving waves or continuously refracted waves are a special type of refracted waves with a bended ray path. This ray path generated by a continuous increase in velocity, bends away from the vertical until the maximum penetration depth is reached. Afterwards the wave ascends back to the surface, with a bended ray path (violet ray path in Figure 2.3). Snell's law (Equation 2.2) expresses, that the ray parameter p of waves remain constant for every single ray. Since the angle of refraction is 90° at the turning point the ray parameter is equal to the reciprocal of the velocity at the deepest point (Greenhalgh and King, 2001; Picotti et al., 2015). Diving waves usually contain a higher amplitude compared to a refracted wave, without a curved ray path (head wave) (Bormann, 2002; Eisen et al., 2010; Kearey et al., 2002).

Traveltime curves of reflected and refracted waves are shown in the upper part of Figure 2.3. The curves display the different traveltimes over offset velocities of a direct (blue), reflected (green), refracted (red) and diving (violet) wave. The refracted wave has a linear relation between offset and traveltime. The traveltime curve of the reflection is hyperbolic. The traveltime depends on the velocity and length of the travel path (Kearey et al., 2002; Telford et al., 1990).

The Reflection and Transmission coefficient (R and T) are given by the ratio of incident and reflected and refracted energy respectively (Equation 2.3). These coefficients are calculated by the impedance contrast (Equation 2.1) of two different media:

$$\begin{aligned} \text{Reflection coefficient: } R &= \frac{(Z_2 - Z_1)}{(Z_2 + Z_1)} \\ \text{Transmission coefficient: } T &= \frac{2Z_1}{(Z_2 + Z_1)} \end{aligned} \tag{2.3}$$

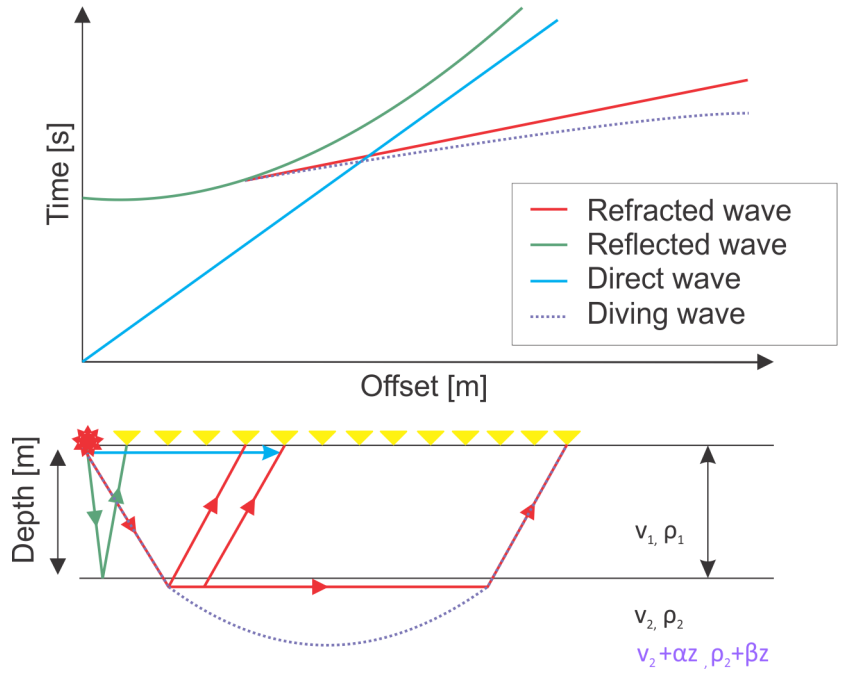

Figure 2.3.: Illustration of the ray path and traveltime curves of the direct (blue), reflected (green) and refracted (red) wave. v_1 and v_2 are the velocity in layer one and two with the densities ρ_1 and ρ_2. In the case of a continuous density increase by the factor β the velocity also increases by the factor α (Modified after Kearey et al., 2002).

where Z_2 is the impedance of medium 2 that is overlain by medium 1 with the impedance Z_1 (Reynolds, 2011; Telford et al., 1990). These laws do not apply if the wavelength is smaller or comparable to the radius of curvature of an object. In this case diffraction would occur (Telford et al., 1990).

2.3. Hook's law and basics of elasticity

Hook's law is defined in terms of stress and strain and relates the applied force to the resulting deformation. Hook's law is given by the following equation:

$$\sigma_{ij} = c_{ijkl} \cdot \epsilon_{kl} \quad with\ i, j, k, l = 1, 2, 3 \tag{2.4}$$

where σ_{ij} is the stress tensor, c_{ijkl} the stiffness tensor or elastic tensor and ϵ_{kl} the strain tensor. The elastic tensor holds the elastic constants of a medium. The number of independent entries in the elastic tensor depends on the symmetry of the medium under investigation.

Only three symmetry classes are important in seismics: orthorhombic, transversal and isotropic (Kaselow, 2004; Thomsen, 1986; Thomsen et al., 2002). In the following the elastic properties of isotropic, transversal isotropic media will be introduced. For more details see Diez et al. (2015); Kaselow (2004); Thomsen (1986); Thomsen et al. (2002).

2.3.1. Elastic properties in isotropic media

The isotropic media is the simplest case of symmetry, where the elastic behavior is independent of direction. Only two independent elastic moduli, the Lamé constants μ and λ exist for the isotropic media. The elastic tensor S for an isotropic media is given as follows:

$$\begin{pmatrix} c_{33} & c_{12} & c_{12} & 0 & 0 & 0 \\ c_{12} & c_{33} & c_{12} & 0 & 0 & 0 \\ c_{12} & c_{12} & c_{33} & 0 & 0 & 0 \\ 0 & 0 & 0 & c_{55} & 0 & 0 \\ 0 & 0 & 0 & 0 & c_{55} & 0 \\ 0 & 0 & 0 & 0 & 0 & c_{55} \end{pmatrix} \tag{2.5}$$

with c_{11}=c_{22}=c_{33}= $2 * \mu + \lambda$, $c_{44} = c_{55} = c_{66} = \mu$ and $c_{12} = c_{21} = c_{13} = c_{31} = c_{23} = c_{32} = c_{33} - 2c_{55} = \lambda$ (Yilmaz, 2001). The shear or rigid modulus μ (Lamé constant) is given by:

$$\mu = c_{55} = \frac{\tau}{\epsilon} \tag{2.6}$$

where the total strain ϵ and the corresponding shear stress components τ are proportional.

For the description of P- and S-wave velocities only the two Lamé constants and the density are necessary:

$$\begin{aligned} v_p &= \sqrt{\frac{c_{33}}{\rho}} = \sqrt{\frac{\lambda + 2\mu}{\rho}} \\ v_s &= \sqrt{\frac{c_{55}}{\rho}} = \sqrt{\frac{\mu}{\rho}} \end{aligned} \tag{2.7}$$

Other elastic moduli can all be expressed in terms of the Lamé constants (Yilmaz, 2001). The bulk modulus K is given by following relation:

$$K = c_{33} - \frac{4}{3}\mu = \frac{-P}{\Delta L} \tag{2.8}$$

where K is the constant of proportionality between the hydrostatic pressure P and the dilatation ΔL. The reciprocal of the Bulk modulus gives the compressibility, which indicates the elasticity of the volume.

The Young's modulus E (Equation 2.9) declares a proportionality of the longitudinal stress and the corresponding strain:

$$E = \frac{\mu(3\lambda + 2\mu)}{(\mu + \lambda)} = \frac{\sigma}{\epsilon} = \frac{\frac{F}{A}}{\frac{\Delta L}{L}} \tag{2.9}$$

where σ describes the stress, defined by the quotient of force F applied on an object with an area A and the strain ϵ,defined as the quotient of the change of the length of an object ΔL and the length L. Poisson's ratio is the ratio of lateral contraction and longitudinal extension:

$$\nu = \frac{\lambda}{2(\mu + \lambda)} = \frac{-\epsilon_{yy}}{\epsilon_{xx}} = \frac{-\epsilon_{zz}}{\epsilon_{xx}} \tag{2.10}$$

where lateral contraction ϵ_{yy} or ϵ_{zz} in an elastic body is dependent on the longitudinal extension ϵ_{xx}. The rigidity modulus μ is zero for fluids and gasses, since these cannot sustain shear stress. In this case the bulk modulus K equals the Lamé constant λ (Biot and Lowrie, 2007; Hearst et al., 2000; Kearey et al., 2002; Mavko et al., 2009; Reynolds, 2011; Telford et al., 1990).

2.3.2. Elastic properties in VTI medium

Most seismic studies of anisotropy are limited to the transversely isotropic (TI) models, with different symmetry-axis orientations. Horizontally layered media can be described by

a TI medium with a vertically (VTI) symmetry axis (Thomsen, 1986; Tsvankin, 1997). The anisotropic fabric of a medium has an influence on the seismic wave propagation. The wavefronts in an anisotropic medium are no longer spherical. Therefore, the traveltimes for different incoming angles depends on the longer travel paths due to increasing offsets and on the angle of the velocities.

Thus, the travel times for different incoming angles do not only depend on the longer travel paths due to increasing offsets, but are also influenced by the angle dependency of the velocities. The elastic tensor for the VTI media has five independent coefficients:

$$\begin{pmatrix} c_{11} & c_{12} & c_{13} & 0 & 0 & 0 \\ c_{12} & c_{22} & c_{22} & 0 & 0 & 0 \\ c_{13} & c_{32} & c_{33} & 0 & 0 & 0 \\ 0 & 0 & 0 & c_{55} & 0 & 0 \\ 0 & 0 & 0 & 0 & c_{55} & 0 \\ 0 & 0 & 0 & 0 & 0 & c_{66} \\ \end{pmatrix} \tag{2.11}$$

with $c_{44} = c_{55}$. In a VTI medium the phase and group velocity of P and S waves are defined as follows:

$$\begin{aligned} v_P(\theta = 0) &= \sqrt{\frac{c_{33}}{\rho}} \\ v_{SH}(\theta = 0) &= \sqrt{\frac{c_{55}}{\rho}} \\ v_{SV}(\theta = 0) &= \sqrt{\frac{c_{55}}{\rho}} \\ v_P(\theta = 90) &= \sqrt{\frac{c_{11}}{\rho}} \\ v_{SH}(\theta = 90) &= \sqrt{\frac{c_{55}}{\rho}} \\ v_{SV}(\theta = 90) &= \sqrt{\frac{c_{66}}{\rho}} \end{aligned} \tag{2.12}$$

where $\theta = 0$, describes the velocity in vertical direction and $\theta = 90$ in horizontal direction (Tsvankin, 1997; Yilmaz, 2001).

These equations allow for a calculation of elastic velocities in a VTI medium. To get an assumption about the degree of anisotropy Thomsen (1986) introduces three anisotropy parameters, ϵ, γ, δ in terms of the five independent components.

$$\begin{aligned} \epsilon &= \frac{c_{11} - c_{33}}{2c_{33}} \\ \gamma &= \frac{c_{66} - c_{44}}{2c_{44}} \\ \delta &= \frac{(c_{13} + c_{55})^2 - (c_{33} - c_{55})^2}{2c_{33}(c_{33} - c_{55})} \end{aligned} \tag{2.13}$$

The three parameters are nondimensional and for most sedimentary rocks of the same order of magnitude and usually much less than 0.2. The Thomsen parameter ϵ gives the difference between vertical and horizontal P-wave velocity, γ gives the difference between vertical and horizontal SH-wave velocity. δ is defined as the second derivation of the P-wave velocity, and thus describes the near vertical dependency on the phase angle of the P-wave velocity (Thomsen, 1986).

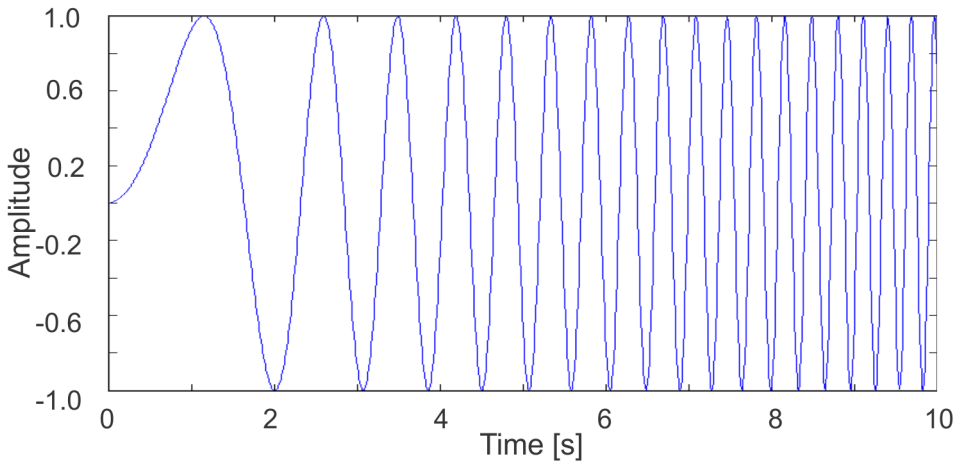

Figure 2.4.: The signal of the electrodynamic vibrator system, called sweep, without a taper applied.

2.4. Vibroseismic source

The generation of seismic waves can be achieved among others by surface energy sources like explosives, hammer blows or vibrator seismic (vibroseis). Most surface energy sources produce a low energy density (Telford et al., 1990). This chapter will concentrate on the vibroseis source and its difference to other sources.

2.4.1. The source signal

One difference between the vibroseis source and other sources is the duration of the source signal. The vibroseis emits what is known as a sweep. A sweep consists of a sine wave with increasing frequency over a predefined time (Figure 2.4). Baeten (1989) describes the signal of the sweep $q(t)$ as:

$$q(t) = a(t)sin[2\pi\theta(t)] \tag{2.14}$$

where $a(t)$ is the taper function, which will be further explained at the end of this section. $\theta(t)$ describes the frequencies as a function of time. The first derivative of $\theta(t)$ equals the instantaneous frequency and can thus be substituted by the following equation:

$$\frac{\partial\theta(t)}{\partial t} = f_0 + \frac{f_1 - f_0}{T}t \tag{2.15}$$

A linear sweep consists of a linear relation of frequency and time (Figure 2.4). In contrast a non-linear sweep has a non-linear relationship between time and frequency, with the effect of depressed amplitudes where frequency changes slowly (Brittle et al., 2001; Goupillaud, 1976). The function of a linear sweep is given by substituting Equation 2.15 in Equation 2.14:

$$q(t) = a(t)sin[2\pi(f_0 + \frac{1}{2}\frac{f_1 - f_0}{T}t)t] \tag{2.16}$$

An upsweep is a sweep where frequencies increase from the start frequency f_0 to the last frequency f_1. Vice versa a downsweep is a sweep where frequencies decrease from f_0 to f_1.

The reduction of the Gibbs phenomenon (ringing at the edges of the filtering) can be performed by the application of a taper to the beginning and end of the sweep. The upper graph in Figure 2.5 includes a taper of 0.5 s whereas the taper of the lower function has a length of 5 s. Tapering of the ends induces a smoothing of the spectrum of the sweep (Baeten, 1989; Goupillaud, 1976).

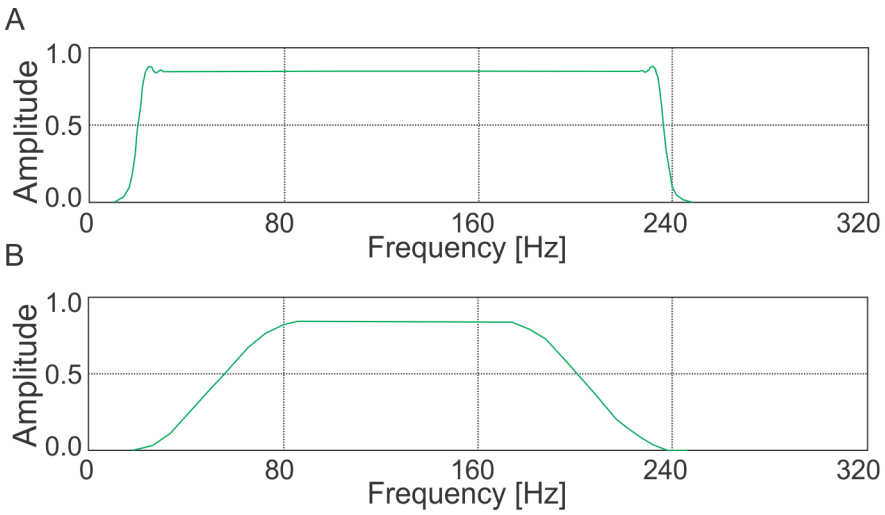

Figure 2.5.: Two linear sweeps with applied tapers. A) sweep with taper length of 0.5 s. B) sweep with taper length 5 s. The taped ends of the sweep aim to control the Gibbs phenomenon (Modified after Brittle et al., 2001).

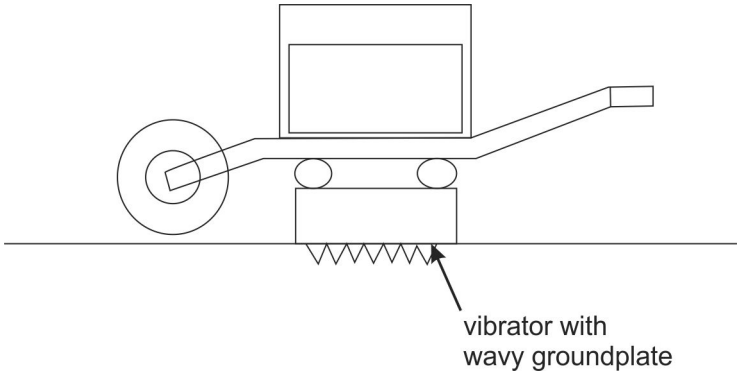

Figure 2.6.: The setup of the electrodynamic vibrator system (ElViS): A wheelbarrow-like frame with a rough groundplate to improve the groundplate-ice coupling (Modified after Druivenga et al., 2005).

2.4.2. The usage of the electrodynamic vibrator system (ElViS)

According to Telford et al. (1990) the usage of a vibroseis source has turned out to be the most popular energy source for seismic measurements on land, since it has been developed in the 1970s.

Figure 2.6 shows the schematic construction of the electrodynamic vibrator system (ElViS). The technique of the ElViS is comparable to a vibroseis source on a vehicle. The reallocation is enabled by mounting it on a wheelbarrow-like frame, movable by one person. The ground coupling occurs by the groundplate that has a wavy surface (Figure 2.6), to improve the coupling the person moving the source can sit on top of the device, increasing the weight (Druivenga et al., 2005). When emitting a sweep, electrodynamic energy is converted into mechanical energy, which forces the base plate of the ElViS to vibrate. The vibration of the baseplate can be performed in P- and S-wave mode. For the P wave the motion of the baseplate is in vertical direction, while the motion for the S wave is in horizontal direction. For the SH-wave mode the ElViS is orientated parallel to the profile, while for the SV-wave mode the ElViS is orientated vertically to the profile (Gadallah and Fisher, 2009).

Comparison of the vibroseis to the explosive source

Often mentioned distinctions between vibroseis and explosive source are of logistical, administrative and physical nature. Vibroseis measurement can be used in inhabited areas, where an extensive damage due to an explosive source would be immense (Eisen et al., 2005; Telford et al., 1990). Higher safety standards are valid for explosive surveys compared to the vibroseis survey. Therefore, the logistic and administrative effort is higher for explosive seismics (Eisen et al., 2015).

In contrast to explosives, the source signal of the vibroseis is known and repeatable, which enables stacking of seismic traces, and thus, an improvement in SNR. During explosive surveys the coupling as well as the absorption of energy in the snow are unknown factors, especially if a measurement is taken twice at the same position. Since the ElViS is a surface source it does not require drilled boreholes to place the dynamite in ice. Therefore, no ghost signal is created, in contrast to an explosive source.

The energy of the signal of a vibrator is mostly elastic, and thus causing wave propagation, whereas much of the explosive energy causes inelastic deformation by breaking ice bounds. The instantaneous forces generated by a vibrator are smaller but spread over time when compared to an impulsive source. Integrating the instantaneous forces over time results together with the lower loss by inelastic deformation and less spurious noise, into a higher total energy level for the vibrator source compared to an impulse source (Eisen et al., 2010; Greenhalgh and King, 2001; Picotti et al., 2015; Polom et al., 2014). The nature of the sweep with its limited bandwidth reduces the resolution of the seismogram, when compared to an explosive source (Diez et al., 2013; Hofstede et al., 2013).

2.4.3. Cross-correlation for vibroseis data

The seismogram showing vibroseis data differs from a seismogram showing explosive seismic data, due to the difference in length of the sweep compared to the impulse. Reflections and other wave signals are not directly detectable in the seismogram of a vibroseis source. To receive a signal comparable to an explosive source signal (as indicated in Figure 2.7, line 6), a cross-correlation has to be applied. Figure 2.7 shows the method of cross-correlation. Line 1 shows the inital sweep signal with a length of 10 s. Three exemplary earth responses, recorded as reflections are shown. At a sufficient impedance contrast every part of the sweep is reflected, resulting in a reflection signal as shown in line 2–4. The first arrival of a reflection at layer 2 is superimposed by the long duration of the reflection signal of layer 1. These individual reflected signals are received as one superimposed signal (line 5) (Telford et al., 1990).

Mathematically the cross-correlation is the summation of the product of cross-multiplication of two digital waveforms, x_i and y_i, over a common time interval. The sum is a similarity measure between x_i and y_i, where traces only contain common information of x_i and y_i (after the cross-correlation). The cross-correlation is similar to a convolution operation, but without folding of the waveforms. A high and positive correlation value will be achieved if the waveforms of x_i and y_i are nearly the same. A low correlation value is achieved if the waveforms are not alike (Kearey et al., 2002; Telford et al., 1990).

The traces $x(t)$ in a seismogram, recorded by geophones (Figure 2.7, line 5) are composed of the initial seismic sweep $s(t)$ convolved (*) with the earth impulse response $r(t)$ as shown in the following equation:

$$x(t) = r(t) * s(t) \tag{2.17}$$

The cross-correlation $x_{CC}(t)$ of Equation 2.17 is given by the cross-multiplication $\otimes$ of Equation 2.17 with $\bar{s}(t)$, the sweep input into the ground.

$$x_{CC}(t) = x(t) \otimes \bar{s}(t) \tag{2.18}$$

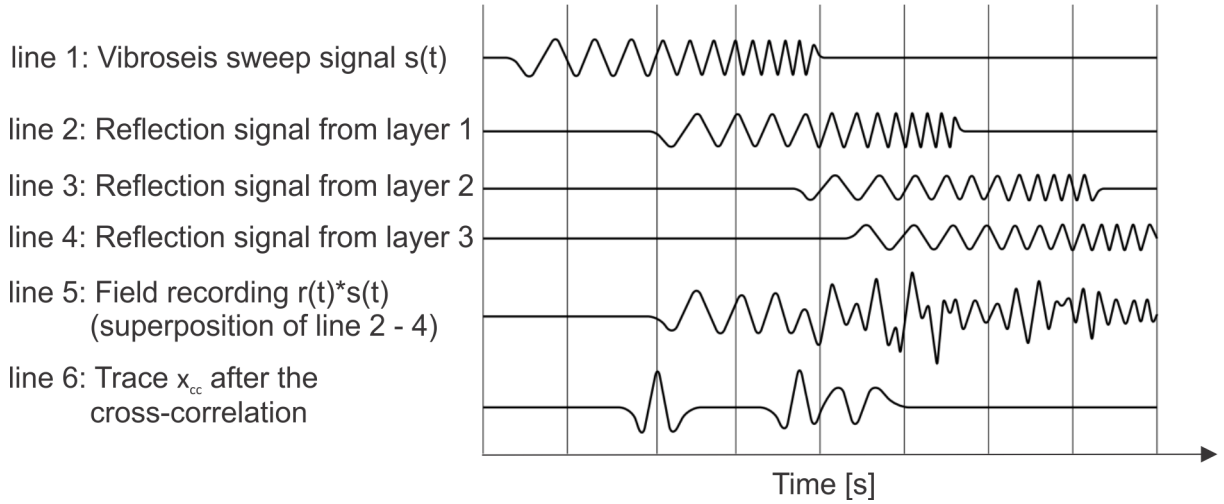

Figure 2.7.: Cross-correlation sequences for vibroseis: Line 1 shows the initial sweep (pilot sweep), this sweep is reflected by 3 layers, indicated in line 2–4. The recorded signal is the sum of line 2–4 and is shown in line 5. The signal after the cross-correlation of line 5 with line 1 (the pilot sweep) is shown in line 6 (Modified after Kearey et al., 2002).

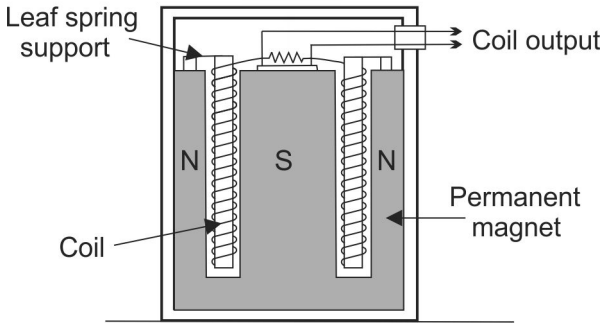

Figure 2.8.: Technical drawing of a geophone: The grey shaded area is the permanent magnet with the coil hanging fixed to the spring into the field of the permanent magnet (Modified after Kearey et al., 2002).

The cross-correlation of the same signal at different points in times is called auto-correlation, which equals the convolution with a Klauder wavelet $k(t)$ for a linear sweep.

$$x_{CC}(t) = r(t) * k(t) \tag{2.19}$$

The output of this cross-correlation (Figure 2.7, line 6) is comparable to traces of an impulse source (Brittle et al., 2001; Goupillaud, 1976; Telford et al., 1990).

2.5. Geophones

Generally, seismic signals are recorded by geophones, hydrophones or seismometers. A geophone converts recorded ground motion into an electrical signal without distorting the amplitudes or frequencies. Depending on the type of geophone, the ground motion can be measured in three dimensions; vertical, east-west and north-south (three-component geophones). The physical principle of most geophones is based on the moving coil.

A small permanent magnet is fastened to the casing of the geophone (Figure 2.8). This permanent magnet provides a magnetic field, in which a cylindric coil is suspended by a leaf-spring. The geophones are either simply placed on the ground or connected to the ground by spikes on the bottom of the geophone. A movement of the ground, caused by e.g. a seismic wave is transferred to the permanent magnet in the geophone as the casing to which the magnet is attached is moving with the ground. Since the coil shows some inertia, there is a movement of the magnet relative to the coil. This relative movement between the magnet and the coil generates a voltage. The geophone is orientated according to the desired wave type. For P waves, which effect a vertical displacement, the geophone is orientated vertically. For S waves, in contrary, it is orientated horizontally (Kearey et al., 2002; Reynolds, 2011).

2.6. Ice-core data

This section briefly introduces the analysis of the ice core B34 and B40 drilled at Kohnen Station. Different methods were used to derive the density, three-dimensional (3-D) structural data and elastic tensors. The density of the ice core was derived from radioscopic imaging of the ice core B40, performed by a X-ray microfocus computer tomograph (ICE-CT) at the Alfred Wegener Institute (AWI) in Bremerhaven. For this method, the sample is mounted and illuminated from bottom to top. The transmitted radiation is captured and displayed in a greyscale-coded intensity image, from which porosity can be calculated. The density can be calculated by the following equation:

$$\rho = (1 - n) \cdot \rho_{ice,bfi} \tag{2.20}$$

where n defines porosity and $\rho_{ice,bfi} = 919\,\mathrm{kg\,m^{-3}}$ the density of bubble-free ice at T=−14°C. The vertical resolution is 0.15 mm for ice core B40, where scanning takes about 15 min (including preparation) per meter. Other methods to derive a density profile is the non-destructive gamma-absorption method or the volumetric method (Freitag et al., 2004; Hoerhold et al., 2011).

3-D structural data was obtained from 3-D XCT. The difference to the ICE-CT measurement is, that the sample is illuminated from different angles. The sample is placed in a cold room on a movable plate between source and detector. The plate rotates in a certain interval while the detector moves in vertical steps during scanning. More than 32000 shadow images are captured during sampling one depth interval, which are then transformed into a series of horizontal cross-sections by a digital convolution algorithm. These represent the 3-D structure of the object based on the local differences in X-ray absorption. During processing the images are separated in voxels (volume pixel) representing ice and air. The porosity is then defined as the ratio of voxels representing void and the total number of voxels (Freitag et al., 2004). 3-D structural data was obtained at four different depths for B34 at the AWI, whereby one 3-D XCT measurement takes several hours.

The elastic tensor (with components $c_{11}, c_{33}, c_{55}, c_{12}, c_{13}$) for a TI medium was calculated in four different depth by the Institute for Snow and Avalanche Research (SLF) in Davos, Switzerland, with 3D structural data for B34 measured at AWI. The elastic tensors were calculated by a finite element algorithm (FEA) developed by the National Institute of Standards and Technology (in the United States). The algorithm assigns material properties to different materials determined by 3-D XCT and conducts virtual experiments to characterize the response of the microstructure as a whole to various boundary conditions. The input parameters are the 3-D structural data, as well as the bulk and shear modulus of air and polycrystalline ice, defined by Schulson and Duval (2009). Under the assumption of an isotropic medium, elastic moduli can be calculated from these elastic tenors (Chapter 2.3.2). Detailed explanation of the three methods can be found in Freitag et al. (2013, 2004); Torquato et al. (1996).

3. Data acquistion and data

3.1. Measurement at Kohnen Station

The LIMPICS (Linking micro-physical Properties to macro features in ice sheets with geophysical techniques) research group carried out seismic measurements in 2011/12 at Kohnen Station, Antarctica. The following chapter introduces the study area. Furthermore, details of the measurement setup at Kohnen Station are shown.

3.1.1. Study area: Kohnen Station

Kohnen Station is located at 75°00'06"S, 0°04'04"E (Figure 3.1) in Dronning Maud Land (DML), East Antarctica and is the German summer base operated by the AWI, Bremerhaven (Germany). It was built for the EPICA (European Project for Ice Coring in Antarctica) deep drilling operation in 2001/02 (Oerter et al., 2009). The ice cores EDML (EPICA Dronning Maud Land), B34 and B40 drilled at Kohnen Station, were utilized for the evaluation of the seismic data acquired at Kohnen in previous as well as in this study.

The study area is located 2892 m a.s.l. (WGS84) on the high-altitude plateau of Antarctica (>2500 m a.s.l). The smooth surface topography including small features like snow dunes (10–15 cm heigh) shaped by the wind, indicates a moderate mean wind velocity. The wind is influenced by the cyclonic system that moves along the Atlantic coast of Antarctica (Freitag et al., 2008; Rotschky et al., 2007).

The ice thickness of 2782 ± 10 m (Steinhage et al., 1999) and the accumulation rate of $65\,\mathrm{kg\,m^{-2}\,a^{-1}}$ (Eisen et al., 2005) was determined by airborne radio-echo sounding measurements. The surface flow velocity for the drill site EPICA is denoted with $0.756\,\mathrm{m\,a^{-1}}$ and the annual mean temperature with -44.6 °C. Since the temperature is year-round below freezing point, no melting occurs in the surface layers (Oerter et al., 2009).

Weiler (2008) determined the depth of the FIT to be at about 87.6 m by CO_2 inclusions sampled at an ice core. Since the ice core represents only a point measurement a firn thickness of about 80–90 m can be expected for the study area under the assumption of small lateral variations.

3.1.2. Data acquisition

The data acquisition systems consisted of 24 geophones, a recording system and the electrodynamic vibrator system ElViS III.

The three-component (3-C) spiking geophones produced by Geospace Technologies with a recording frequency of 40 Hz were used. A vertical as well as two horizontal (perpendicular to each other) components are fixed in one casing. The geophones were attached by cables to a Geode recording system produced be Geometrics. The Geode records in total 72 channels: 24 channels for the vertically orientated components of the geophone and 2 x 24 channels for the horizontal components (1 x 24 horizontally in line and 1 x 24 perpendicular to the line). During measurement all three components recorded unattached to the mode. The sampling interval is chosen to be 0.25 ms, while the listening time is 2–5 s.

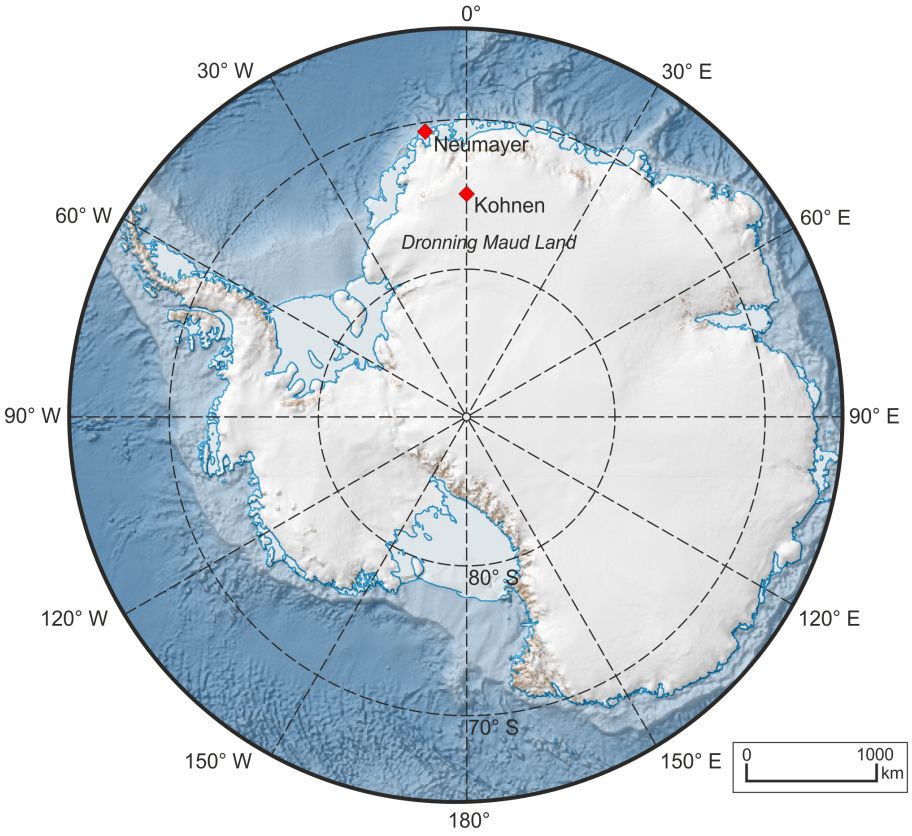

Figure 3.1.: Location of the study area: Kohnen station, DML, situated in the Atlantic sector of Antarctica (Modified after Amante, C. and B.W. Eakins, 2009. ETOPO1 1 Arc-Minute Global Relief Model: Procedures, Data Sources and Analysis. NOAA Technical Memorandum NESDIS NGDC-24. National Geophysical Data Center, NOAA. doi:10.7289/V5C8276M).

The source was the electrodynamic vibrator system, ELVIS III P 8 for the P-wave mode and ElViS III S 8 for the S-wave mode (see Chapter 2.4). ElViS III has a peak force of around 450 N and a weight of 130 kg. The source signal consists of a linear upsweep, over a 10 s time period with P-wave frequencies between 30–240 Hz (Figure 2.4) and S-wave frequencies between 40–300 Hz. A 0.5 s taper function (Figure 2.5 (A)) was applied to the sweep.

Measurement Setup

A measurement setup with two profiles perpendicular to each other was chosen. The focus of the measurement procedure was a high fold of coverage. The measurement setup described below and in Table 3.1 resulted in a maximum fold of 23.

The first profile was taken parallel to the ice divide and has a total length of 420 m (from now on referred to as parallel profile). The geophones as well as the shot points have a spacing of 10 m, while the shots occur between two geophones. The arrangement of 11 additional shot points beyond the geophones results in a maximum offset of 325 m. Channel 72 recorded the pilot sweep, which is needed for the cross-correlation. At each shot location in the parallel profile, two sweeps with alternating polarity were generated for the S wave (SH and SV wave) and three sweeps for the P wave. This resulted in 44 shot points and 66 common midpoint (CMP) with a spacing of 2.5 m.

The second profile was taken perpendicular to the ice divide (from now on referred to perpendicular profile). It has a length of 115 m with a geophone spacing of 5 m while the shot spacing is 1 m. Shot locations of the P-wave mode are only within the profile as illustrated

in Figure 3.2. In this measurement setup the geophones were arranged on an unusual order resulting in the following sequence of geophones: 24-1-23-2-22-3 and so on. This sequence can be adjusted while processing. The maximum offset for the perpendicular profile is 85 m. In contrast to the parallel profile only one shot was taken at every shot point position in P-wave mode and two sweeps with alternating polarity were taken in SH-wave mode. No shots were taken in SV-wave mode. This setup resulted in 56 shot positions and 171 CMPs with a spacing of 0.5 m.

Table 3.1.: Details of the data acquisition.

	parallel profile	**perpendicular profile**
geophone spacing	10 m	5 m
shot spacing	10 m	1 m
number of shots	3 x P- & 2 x SH- & 2 x SV wave	1 x P- & 2 x SH wave
number shot position	44	56
max. offset	325 m	85 m
profile length	420 m	115 m
number of CMP	66	171

3.2. Data description

Figure 3.3 shows the P-wave seismogram for shot 70 in the parallel profile with frequencies ranging from 30–240 Hz. No reflection hyperbolas are visible, also not in the lower part of the seismogram (Figure A.1 in the Appendix). The seismograms of the SH- and SV wave with a frequency range from 40–300 Hz do not show reflection hyperbolas (Figures A.2-A.5 in the Appendix). Diving waves (red) and multiple diving waves (blue, according to Picotti et al. (2015)) are highlighted in Figure 3.3, as well as the approximated area superimposed by groundroll, mostly Rayleigh and Love waves. Multiple diving eaves are generated when a diving wave is reflected at the firn-air interface.

The densities obtained by XCT measurements at ice core B40 down to a depth of approximately 90 m can be seen in Figure 3.4. In 87 m depth the density equals 0.83 g cm^{-3}, which corresponds to the critical density for the FIT (Chapter 1.1.1) and is consistent with CO_2 inclusion measurements (Weiler, 2008).

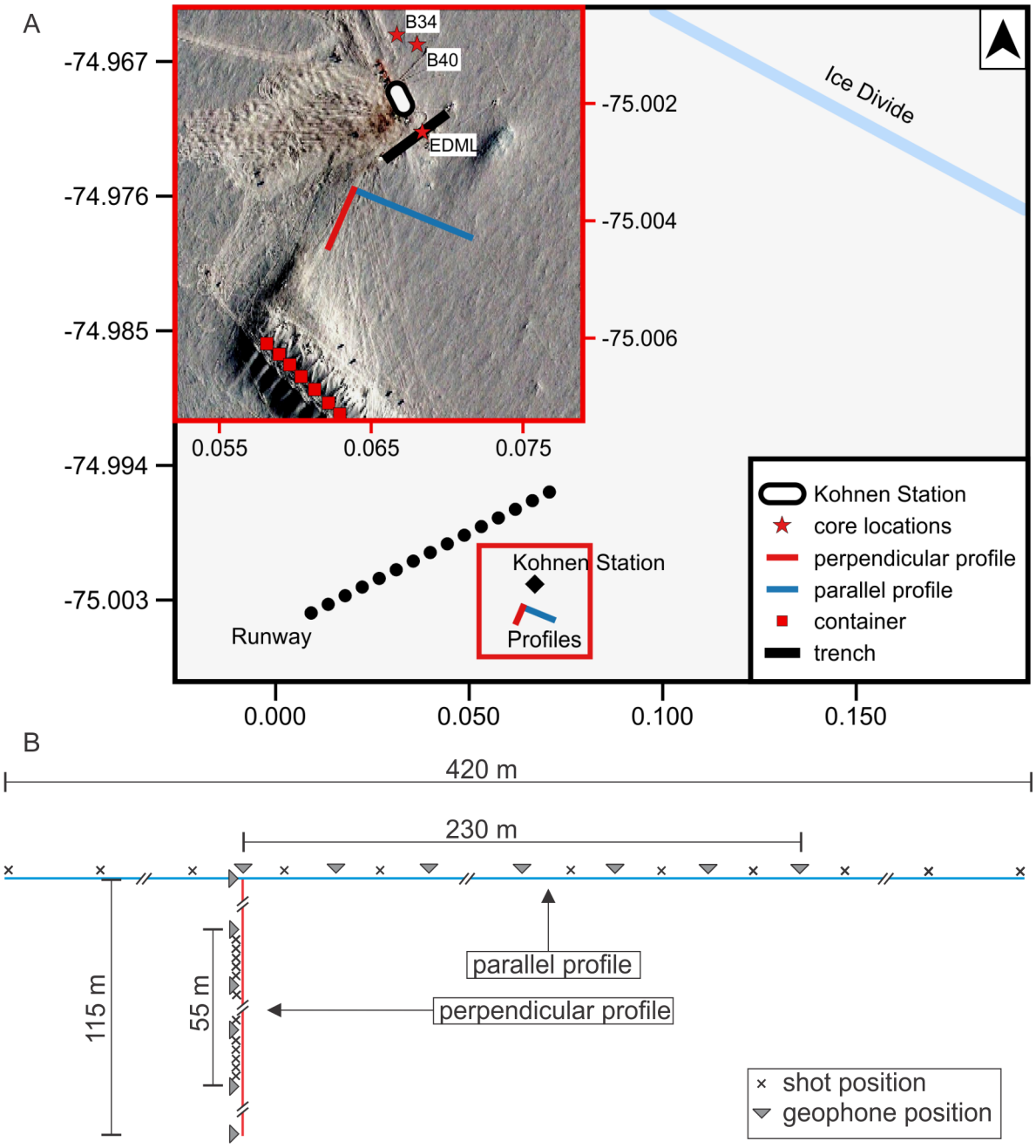

Figure 3.2.: Geometry of the data acquisition of the profile parallel and perpendicular to the ice divide, triangles show geophone positions, crosses shot positions. Details of the data acquisition can be found in Table 3.1.

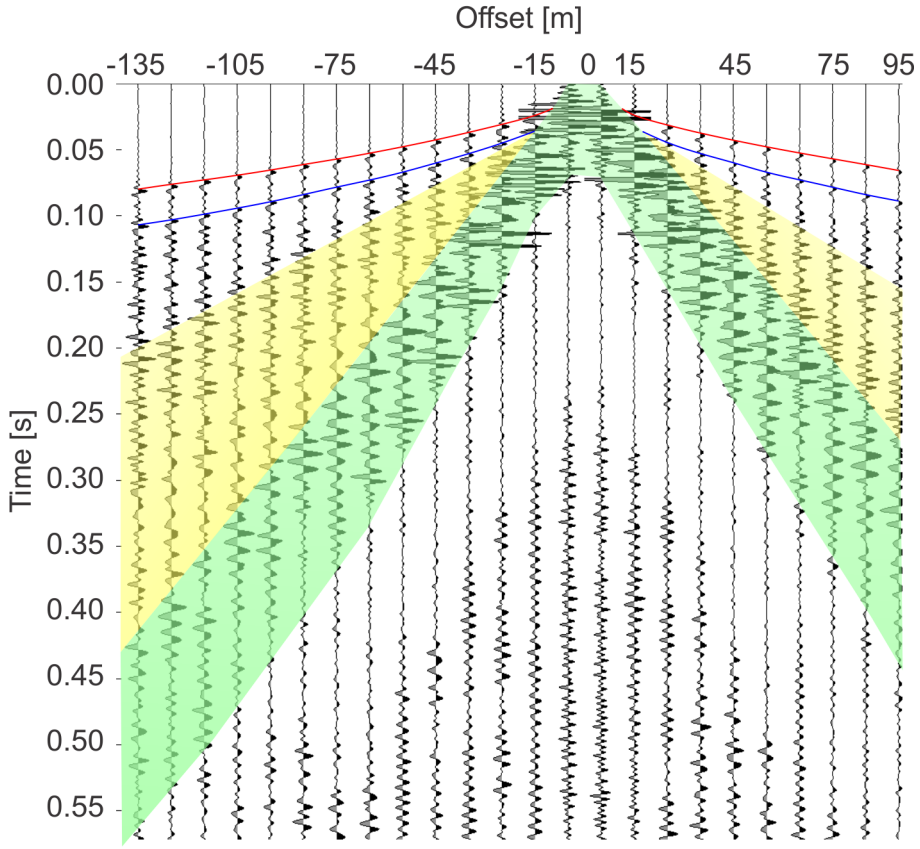

Figure 3.3.: Vertical component of P-wave shot 70 of parallel profile. Diving wave first breaks (red lines), multiple diving waves (blue lines) and the approximated area containing high amplitude groundroll (surface waves, yellow and green shaded) are highlighted. The green shaded groundroll appears to be slower and contains a higher velocity than the yellow shaded groundroll.

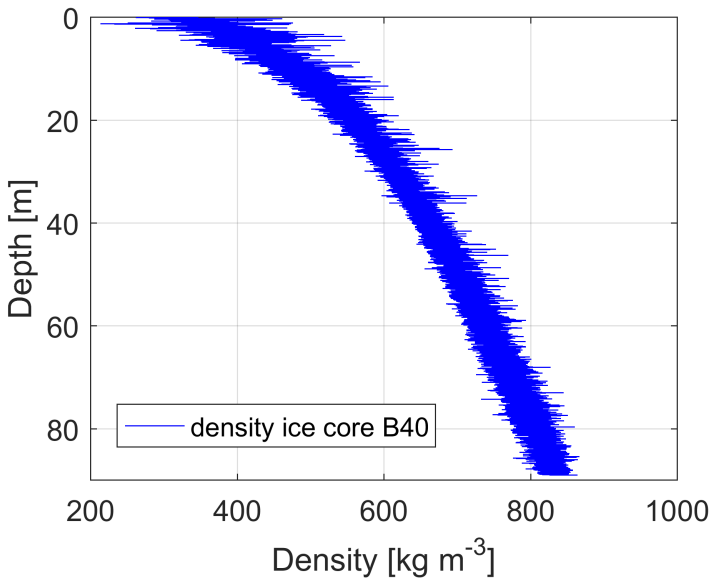

Figure 3.4.: Density profile at Kohnen Station measured by XCT on ice core B40.

4. Data processing

The processing of the data has been performed by the commercial software Paradigm EPOS 2011.3. ECHOS is a software incorporated in EPOS, which is designed to process seismic data in the time domain. The software contains several subprograms like GEODEPTH, which supplies additionally tools for the velocity analysis, depth migration and interpretation.

Preceding to filtering and muting the data, the vibroseis data has to be cross-correlated. The cross-correlation was done with a synthetic sweep because the recorded sweep in the field had a bad quality. The synthetic sweep for the cross-correlation was composed of a linear upsweep with frequencies from 30–240 Hz for the P-wave mode and 40–300 Hz for the S-wave mode, with a taper function of 0.5 s. Henceforward, raw data describes cross-correlated data.

Data processing is essential, because the data are very noisy. Additionally, no reflection hyperbolas are visible in the raw data. Possible reflections are superimposed by groundroll. I divided the data acquired on the parallel seismic profile into three groups, according to their shot positions. Figure 4.1 shows exemplary P-wave shots of the parallel profile of the three groups with their corresponding energy spectra. Shots taken outside the geophone line with offsets larger than 250 m, from now on referred to as first group, show less ringing due to the larger offset and less high amplitude groundroll caused by Love and Rayleigh waves. Shots outside the geophone line, but with offsets smaller than 250 m, from now on referred to as second group (Figure 4.1 (B)), contain more high amplitude noise than the first group. Characteristic differences for different offset ranges resulted in an individual processing routine. Shots within the geophone line are attributed to group three. Group three (Figure 4.1 (C)) is characterized by lots of ringing and high amplitude groundroll, which resulted in a different amplitude spectrum compared to other groups. Frequency spikes at different frequencies can be observed in all groups.

In general, the P-wave shots of the perpendicular profile contain more noise than the shots of the parallel profile. Additionally, in the perpendicular profile all shots were taken within the geophone line, thus, containing more surface-wave signal. Therefore, I invested more time in processing of the data parallel to the ice divide, especially the P-wave data. The SH-wave data of the perpendicular profile was not processed since the workload would be too time-consuming.

The different components and waves described in the following could lead to confusion, therefore, Figure 4.2 shows a schematic drawing of the different types of profile, mode, group and component. The P-wave signal is best recorded by the vertical component of the geophone. Therefore, if referred to a P-wave shot, the vertical component of the P-wave shot is considered, if not mentioned differently.The SV wave is best recorded by the first horizontal component, the SH wave by the second horizontal component. In the following a S-wave shot describes the recorded horizontal component of a S-wave shot. Nevertheless, all components recorded during shooting, which enabled a comparison of the different components.

Hereafter, the theory of processing as well as processing steps applied to the data to make reflections detectable (Chapter 4.1) are described. This is followed by the analysis of the origin of high amplitude signals and the diving-wave inversion.

The time recorded by the geophone, is from now on referred to as measured traveltime (mTT). Reflections would be described by TWT, but reflections cannot be identified clearly and since refractions are also described in this thesis, the term mTT is established.

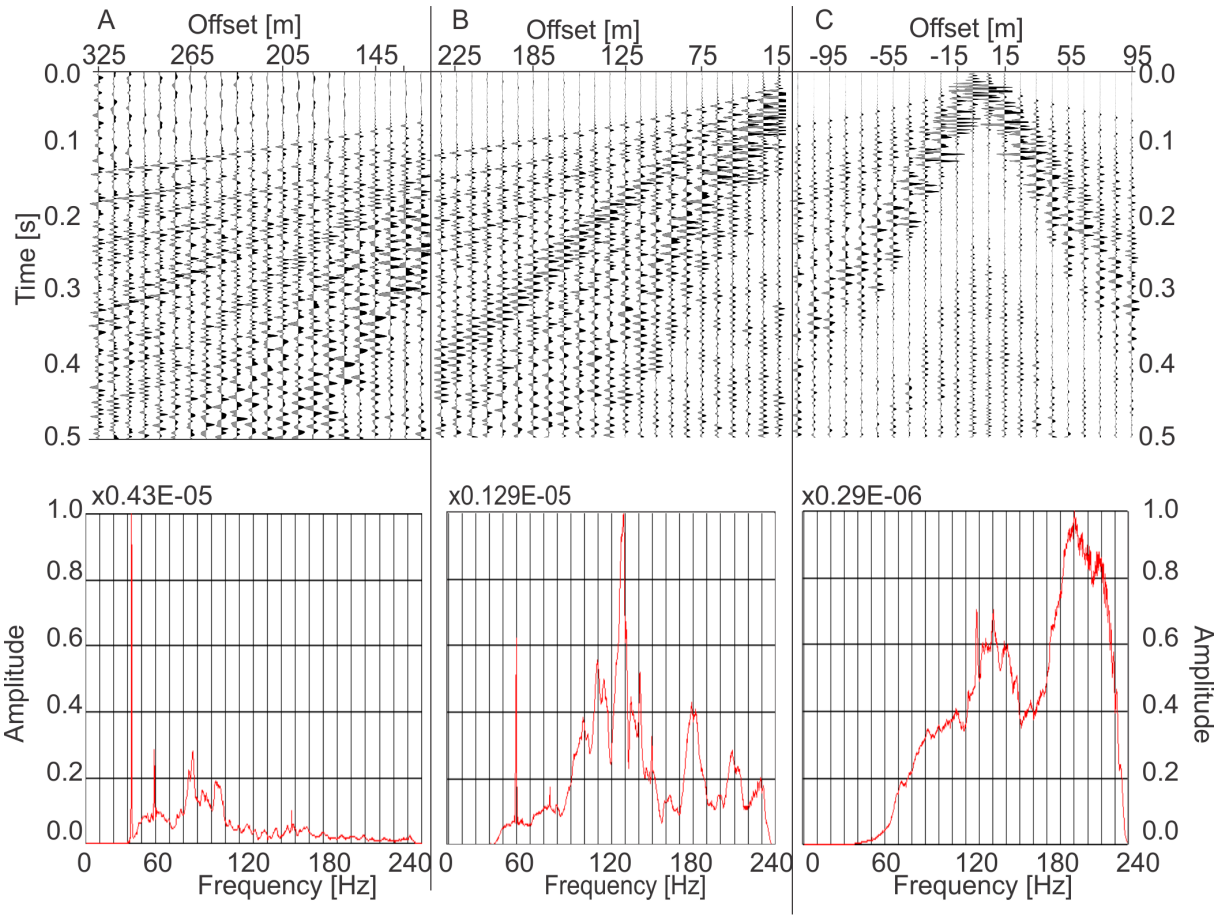

Figure 4.1.: Exemplary vertical component and amplitude spectra of P-wave shots of the parallel profile. Shots are displayed in the upper figure, whereas the lower graph represents the amplitude spectrum: A) Shot 1, classified as first group, with shots containing large offsets to the geophone line. B) Shot 27, classified as second group, with shots outside the geophone line, but offset smaller than 250 m and C) Shot 70, classified as third group, with shots taken only within the geophone line.

4.1. Processing of reflection seismic data

This subchapter concentrates on the processing applied to enhance the detection of reflections. The processing was adapted to every group individually, which resulted in 10 processing sequences. Details of the individual processing sequences are listed in Table 4.1. Examples of values used for processing, as well as the method of choosing values is described in the following. In advance to the applied processing a different domains used during processing as well as short introduction into the Fourier transformation is given.

4.1.1. Domains and Fourier transformation

For processing of seismic data different dimensionalities and domains can be used. 1-D filters affect traces individually, while 2-D filters affect a collection of traces, like for instance a shot. For 2-D filters the design window as well as the application window is chosen to include more than one trace. Thus neighboring traces affect each other.

To enhance the visualization of the signal in the seismogram different domains can be used. Most often the t-x (time-space) domain is used. Here the time is shown against offset, where the strength of the events is displayed by the amplitude.

Table 4.1.: Parameters of applied filters. Flanks of the bandpass filter are chosen between 20–40 Hz. Repetition of application of the notch filter is noted in brackets for every notch frequency.

	bandpass frequencies [Hz]	**notch frequencies [Hz]**	**f-k filter**	**velocity moveout groundroll**	**mute/edit traces**
P wave					
parallel profile					
group 1	80-100–240-260	170 (once), 190 (once)	linear events	220	diving wave first breaks, occasional shots
group 2	140-180–240-260	130 (once), 230 (twice)	not used	220	diving wave first breaks, occasional shots
group 3	not used	50 (twice), 130 (twice), 230 (twice)	not used	not used	diving wave first breaks, occasional shots
perpendicular profile	100-120–240-260	130 (once), 230 (once), 155 (once)	not used	not used	diving wave first breaks, several channels and shots
SH wave					
parallel profile					
group 1	50-75–300-320	147 (once), 250 (twice)	weak linear events	not used	diving wave first breaks, several channels and shots
group 2	50-75–300-320	110 (once), 235 (once)	not used	not used	diving wave first breaks, several channels and shots
group 3	50-75–300-320	140 (once), 160 (once), 255 (once)	not used	not used	diving wave first breaks, several channels and shots
SV wave					
parallel profile					
group 1	80-90–300-320	100 (once), 150 (once), 250 (once)	linear events	not used	diving wave first breaks, several channels and shots
group 2	80-90–300-320	100 (once), 235 (once)	not used	not used	diving wave first breaks, several channels and shots
group 3	not used	115 (once), 140 (once)	not used	not used	diving wave first breaks, several channels and shots

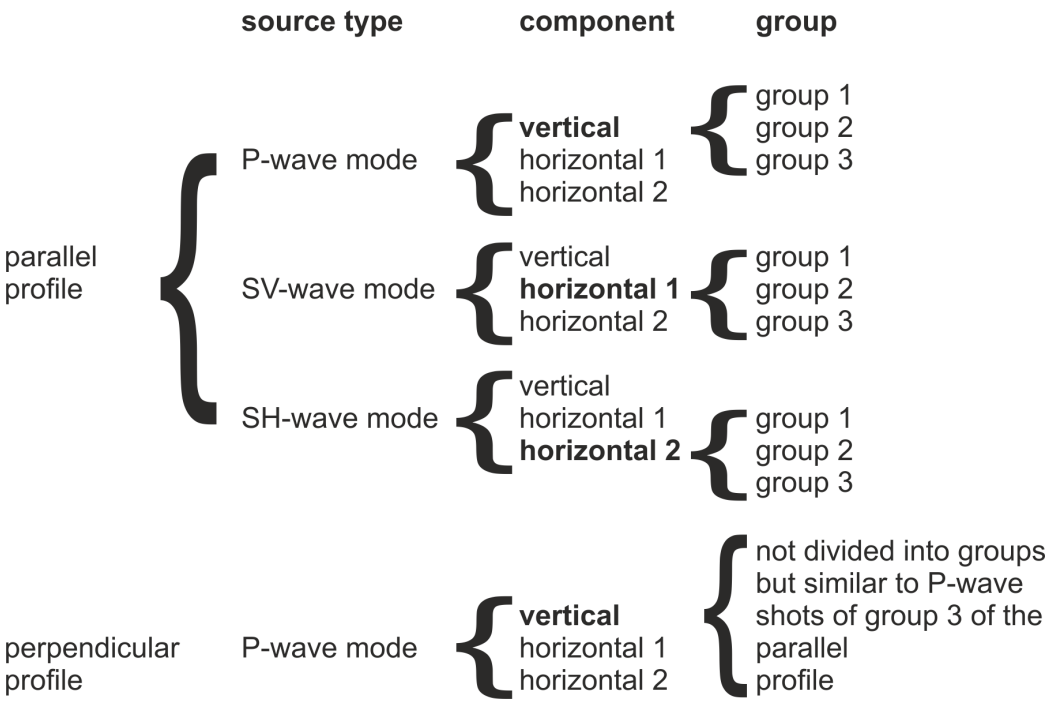

Figure 4.2.: Schematic drawing of different types of profile, mode, group and component. The component referred to, if not mentioned differently, is written in bold type for every mode.

When filtering, a frequencies that could be suppressed is chosen. Therefore, the signal x(t) needs to be transformed into a function of frequency. The theory of the Fourier transformation states that every signal can be described as a series of sine functions. Removing some of these sine functions enables to remove specific frequencies from the wave signal. After removing specific frequencies the wave signal is transformed back into a function of time.

The f-k (frequency-wavenumber) domain can be used to identify waveforms by their velocity and frequency, which will be described in detail in Chapter 4.1.4. The transformation from $x(t)$ into $f(k)$ domain is called 2D Fourier transformation over time and space.

The Karhunen-Loève transformation (K-L transformation) is based on the theory that a signal can be described by many eigenfunctions, each describing a different characteristic. The K-L transformation transforms the data from the t-x domain into a number of eigenfunctions, which combined represent the most important characteristics of these signals (Al-Yahya, 1991; Yilmaz, 2001). Each eigenfunction consists of the same number of traces as considered before the transformation. The first eigenfunction contains events with the highest correlation value, further eigenfunctions contain events with less degree of correlation. After correcting the traces for linear moveout, flattened signals will have the highest value of correlation, and thus, map into the first eigenfunction (Yilmaz, 2001).

The filtering of into eigenfunctions will be described in Chapter 4.1.5 Another domain is the tau-p domain (Yilmaz, 2001), which will not be discussed in this thesis.

Common midpoint

A CMP represents a series of traces (also called gather) which are reflected at the same location in the subsurface (Figure 4.3). The fold of coverage describes the number of traces in one CMP gather (Kearey et al., 2002).

The common depth point (CDP) resembles the CMP in a homogeneous subsurface with

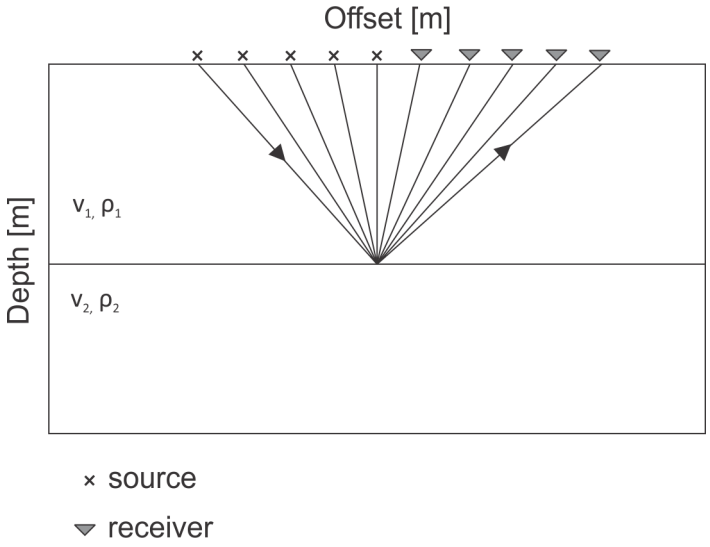

Figure 4.3.: Schematic drawing of a CMP gather, with source (crosses) and receiver position (triangles) on the surface (Modified after Yilmaz, 2001).

horizontal layering (Yilmaz, 2001).

4.1.2. Frequency filters

Frequency filters are defined by the preservation of a desired bandwidth and the suppression of others.

Bandpass filters are widely used frequency filters incorporating a high and low pass filter. It is often used because a high percentage of data contains some low frequency noise like groundroll and some high frequency ambient noise (Yilmaz, 2001). A bandpass filter is defined by two cut-off frequencies (Figure 4.4). The range between these frequencies is known as the passband, where the amplitudes of the signal are multiplied by one, whereas the amplitudes outside the passband are multiplied by zero. To avoid the Gibbs phenomenon slopes on both sides of the passband are assigned, resulting in a trapezoid shape of the filter (Hatton et al., 1991; Yilmaz, 2001).

Notch filters (Figure 4.5) attenuate the recorded data at a given frequency, the notch frequency. The amplitude of this frequency is multiplied by zero, while the other amplitudes are multiplied by a factor of one. This filter can be applied if a noise signal is seen in the seismogram containing one specific frequency. The notch-filter tool in ECHOS provides the possibility to apply the notch filter one, only forward, or twice, forward and backward. The backward application is supposed to remove phase effects caused by the forward application. Ringing is referred to a noise caused by the spurious frequency or parasitic resonance of a geophone. A vertical geophone is designed to record movements in vertical direction. To allow the coil to move freely a lateral movement cannot be prevented. The resonance frequency of the spring in working direction is called the natural frequency, while the resonance perpendicular to the working direction is called spurious or parasitic resonance. Ground motion (e.g. a high energy groundroll) can cause the geophone to resonate at this frequency, which can be seen in the seismogram as a single strong frequency. This resonance frequency depends on the spring design thus changes with different geophone types (Faber and Maxwell, 1997; Hatton et al., 1991).

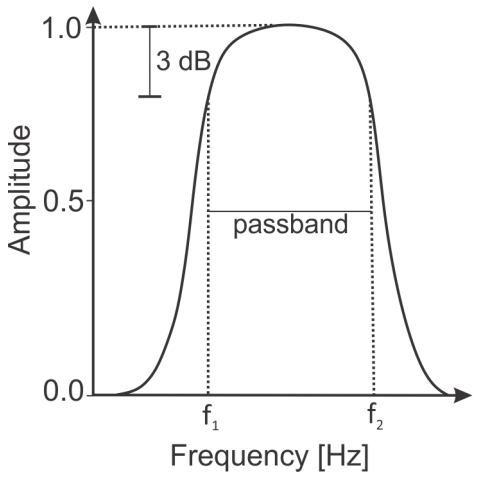

Figure 4.4.: Spectrum of a bandpass filter with the cut-off frequencies f_1 and f_2 (Modified after Hatton et al., 1991).

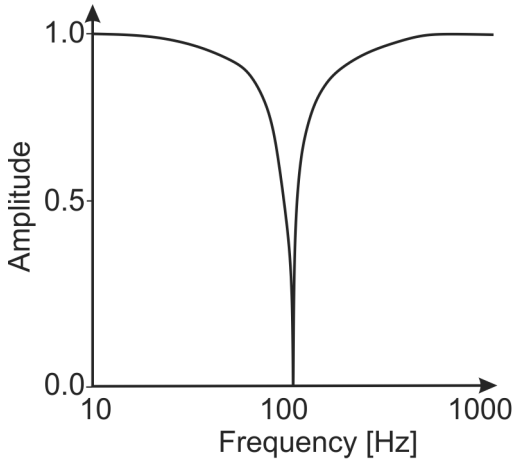

Figure 4.5.: Spectrum of a notch-filter (Modified after Hatton et al., 1991).

Ringing caused by the parasitic resonance can be observed in several traces in this dataset, especially after the high amplitude groundroll and before the first breaks of diving waves. The amplitude spectra for different groups show ringing at different frequencies (Figure 4.1). I identified parasitic resonances by a spike in the amplitude spectrum. An exemplary section of SH-wave shot 49 of the second group with ringing is shown in Figure 4.6 (A). The amplitude spectrum in Figure 4.6 (B) of this section shows two peaks at frequency 116.5 Hz and 230 Hz. I applied notch-filters with these frequencies. Some ringing is also observed in the low frequency area. To remove this, I applied a bandpass filter with a passband between 50–320 Hz, with a ramp of 20 Hz.

The amplitude spectrum of shots of the third group shows higher amplitudes for frequencies larger than 160 Hz, compared to frequencies below 160 Hz (Figure 4.1 (C)). The seismogram shows high amplitudes for the surface waves. Since shots in the third group contain only near offset shots they also contain a lot of surface-wave signal. To investigate the frequency content of the surface waves I applied a bandpass filter with a passband between 100–240 Hz and 160–240 Hz individually on raw data (this step is not part of the processing sequence).

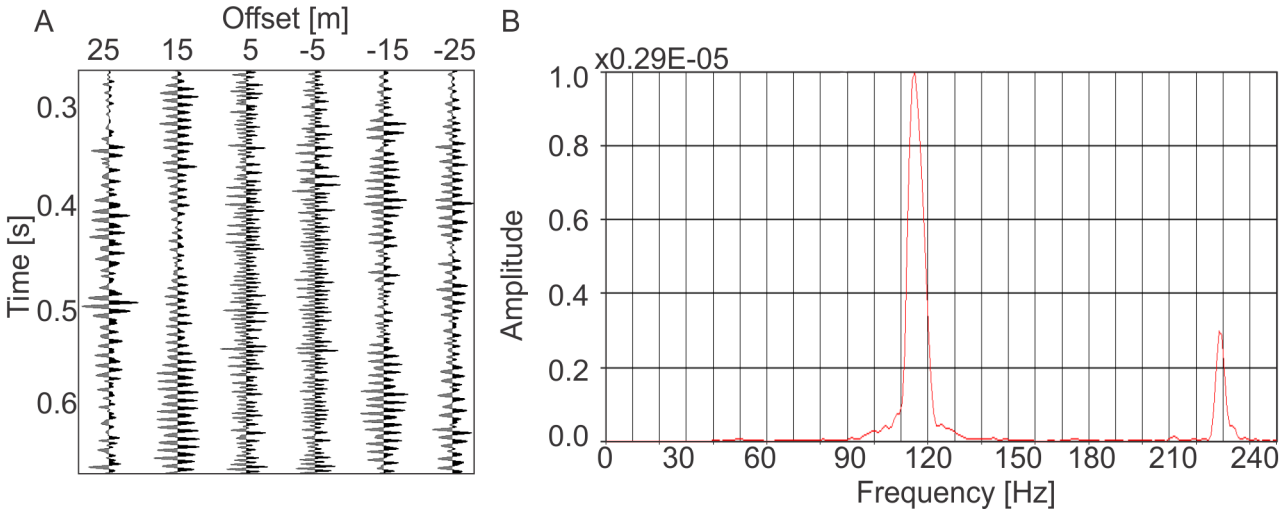

Figure 4.6.: A) Part of the vertical component of SH-wave shot 49 of the second group after the high amplitude groundroll. Ringing of traces can clearly be seen. B) Spectrum of (A). Spikes represent frequencies of parasitic resonance.

4.1.3. Editing and muting traces

The removal of parts of the seismogram in the t-x domain can be done by muting. In this case the amplitude of the picked signal is multiplied by zero. This can be useful to eliminate, for instance, the direct wave. However, while muting not only a specific signal, but the whole signal at the time is muted. The tools IEDIT and MUTE are capable to mute complete traces, specific parts of traces or complete trace series (von Hartmann et al., 2015).

Shots or channels with bad quality and high noise level before the diving wave first breaks are observed in the raw data. I muted certain channels or in special cases complete shots, if the above mentioned filtering did not improve the data significantly. Exemplary is channel 53 in all shots inside the geophone line for the S wave. Ringing could not be removed, thus this channel was muted.

4.1.4. F-k filter

The f-k filter belongs to the velocity filters, which removes coherent noise by the dip angle of these events in the f-k domain. Several noise types, such as groundroll, guided waves and side-scattered energy might be more visually separated in the f-k domain than in the t-x domain. An exemplary plot of frequency f against wavenumber k can be seen in Figure 4.7. Waves travelling towards the source, like backscattered waves, have a negative wavenumber. Waves with a movement in spread direction, travelling away from the source, have a positive wavenumber. Noise dominated areas in the f-k plot are selected manually and afterwards filtered (dos Santos and Porsani, 2013; Kearey et al., 2002; Yilmaz, 2001).

Figure 4.8 (A) shows the f-k spectrum of a P-wave shot of group three. Frequencies higher than 160 Hz show higher amplitudes, compared to the lower frequencies. This is consistent with the amplitude spectrum in Figure 4.1. No clear separation between groundroll (usually low velocities, and thus, higher wavenumbers than reflections) and reflections can be seen. I tried to get information about the velocity and frequency of the surface waves from the seismogram and used these for the f-k filter. This induced noise (Figure A.7, in the Appendix), therefore the f-k filter was not used for the third group shots. The shots within the first and partly the second group show some linear events in the f-k plot, as can be seen in Figure 4.8 (B).

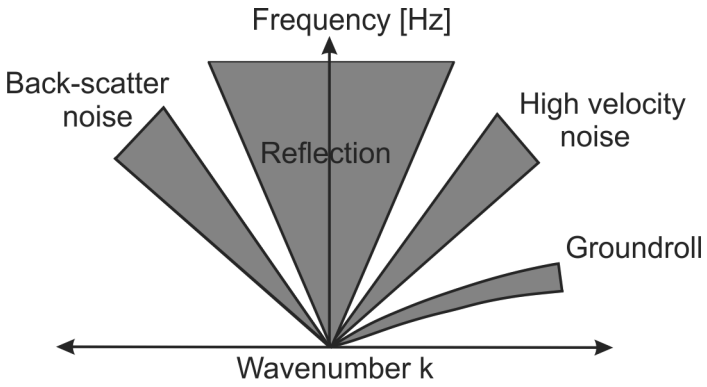

Figure 4.7.: Different type of signals in the f-k spectrum. The separation of noise, groundroll and reflections is visible (Modified after Kearey et al., 2002).

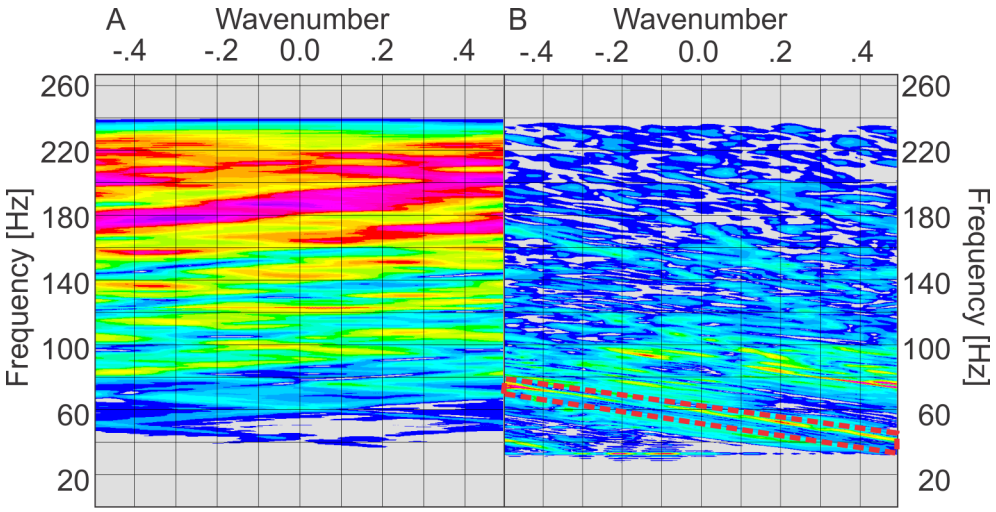

Figure 4.8.: F-k spectra generated from raw data. Violet and red colour represent high amplitude, whereas blue represents low amplitude A) F-k spectrum of shots of the third group. B) F-k spectrum of a shot of the first group.

4.1.5. Filtering of eigenfunctions

The seismic signal can be transformed into eigenfunctions by the K-L transformation. By discarding selected eigenfunctions it is possible to eliminate signals like groundroll or multiples from the data, if their propagation velocity is known. Conventional frequency filters, like f-k filter and bandpass filters, can also be used to remove groundroll from the signal, but in cases of a low SNR the f-k filter could cause serious distortion of the signal. Reflections canceled out by these filters might also contain these frequencies, which are lost by filtering. To overcome this problem, the K-L transformation separates the reflection from the groundroll permitting to suppress only the groundroll signal (Al-Yahya, 1991; Londoño et al., 2005; Naderpajouh et al., 2011; Yilmaz, 2001).

The K-l transformation was applied on raw data. I calculated velocities for the high amplitude groundroll, in the P-wave shots of the second group, marked in Figure 4.9. A moveout correction with these low velocities would shift traces in the far offsets above 0.0 s and data would be lost. This issue was solved by shifting the data 1.5 s deeper. The calculated velocities are only an approximation. A velocity range for the moveout correction can be defined. The best moveout correction, that lines the signals horizontally, can then be chosen. I chose a velocity range of 200–600 $\mathrm{m\,s^{-1}}$ for the moveout correction. Afterwards I chose the velocities resulting in a horizontal alignment of the surface and diving waves and filtered the first

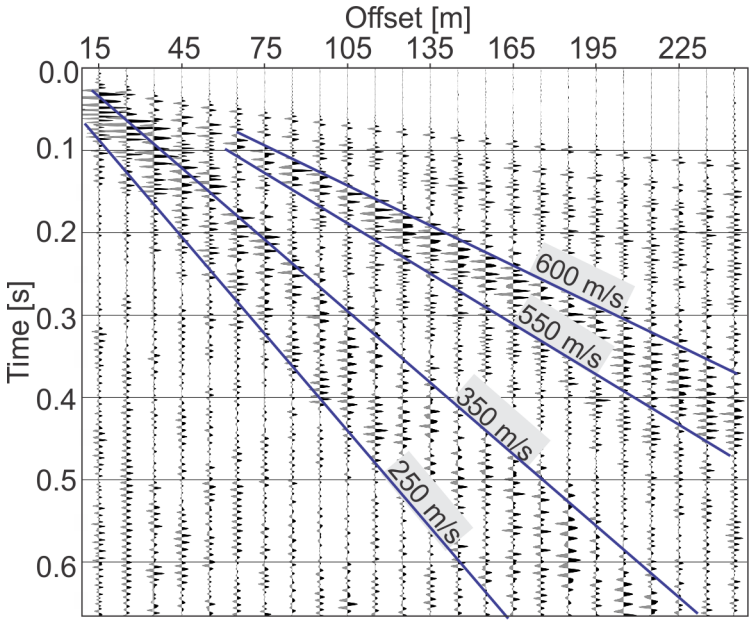

Figure 4.9.: P-wave shot 25 of the second group after the application of a bandpass filter. Exemplary velocities for the high amplitude groundroll are calculated from offset-traveltime pairs (under the assumption of a linear moveout).

eigenfunction of the data. This is followed by the reversal of the moveout correction and time shift.

4.1.6. Velocity analysis and NMO correction

To introduce the importance of a precise velocity analysis the procedure of NMO correction is described first. Afterwards two different methods, CVS and HVA, to derive velocities from seismic data are described.

Normal moveout correction

Normal moveout (NMO) describes the method of removing the time difference between the TWT at zero offset and a given offset, caused by the greater travel path. The NMO correction is usually done in the CMP domain. Assuming a horizontal homogeneous layer, the traveltime curve has a hyperbolic shape (Figure 4.10 (A)), as can be seen in Equation 4.1, the formula describing the traveltime curve of a reflected wave:

$$t^2 = t_0^2 + \frac{x^2}{v^2} \tag{4.1}$$

where t_0 is the traveltime at zero offset, t the traveltime at a given offset x and v the velocity the wave travels with in the present underground. The reflection TWT must be corrected for NMO, thus reflections are horizontal in a CMP gather (Figure 4.10 (B)).

In seismics two different velocities are related to NMO correction. The stacking velocity v_{stack} describes the velocity that fits the reflection hyperbola over the entire spread length, while the v_{NMO} is based on the small-spread hyperbolic traveltimes. The difference in v_{stack} and v_{NMO} is negligible for this dataset (Kearey et al., 2002; Taner, M.T. & Koehler, 1969).

Moreover, the RMS velocity describes the velocity the wave travels with. v_{RMS} can be calculated by the following equation:

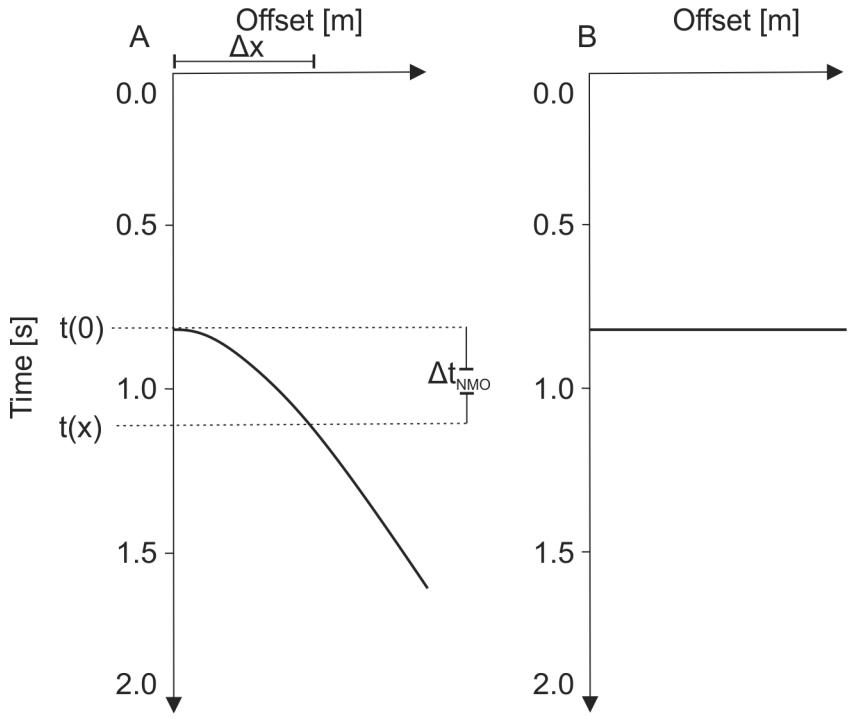

Figure 4.10.: Concept of the NMO correction. A) Traveltime curve with normal moveout. Δt_{NMO} is the time difference of the traveltime at zero offset x_0 and the traveltime at a given offset x. B) Traveltime curve corrected for NMO (Modified after Yilmaz, 2001).

$$v_{RMS} = \sqrt{\frac{\sum_n v_{int,n}^2 t_n}{\sum_n t_n}} \tag{4.2}$$

where $v_{int,n}$ and t_n represent the interval velocity and the traveltime in layer n. By multiplying the velocity with the traveltime, the thickness of the layer with a certain interval velocity is calculated. Therefore, v_{RMS} does not represent the mean of all velocities down to a certain depth but does also incorporate the thickness of the layers and thus their contribution to the velocity. v_{stack} should be equal to v_{RMS} for small offsets and horizontal layers (von Hartmann et al., 2015; Yilmaz, 2001).

Constant velocity stack

One way to derive the stacking velocity is the constant velocity stack (CVS). Panels containing a certain number of CMP gathers are stacked with a range of velocities, from the lowest to the highest velocity. A comparison of the stacked sections (Figure 4.11) allows to choose the appropriate velocity for every reflector (Hatton et al., 1991; Yilmaz, 2001). The first column in Figure 4.11 displays the original data, the next column was corrected with a velocity of $1500\,\mathrm{m\,s^{-1}}$ until a maximum velocity of $3400\,\mathrm{m\,s^{-1}}$ in the last column. The detection of horizontal reflections through the different column derives the best stacking velocity for this certain reflector, like indicated by the orange circles and arrows.

Horizon velocity analysis

Another method to determine the velocities of reflections is the horizon velocity analysis (HVA). In contrast to the CVS, the focus is pointed to the analysis of a particular horizon

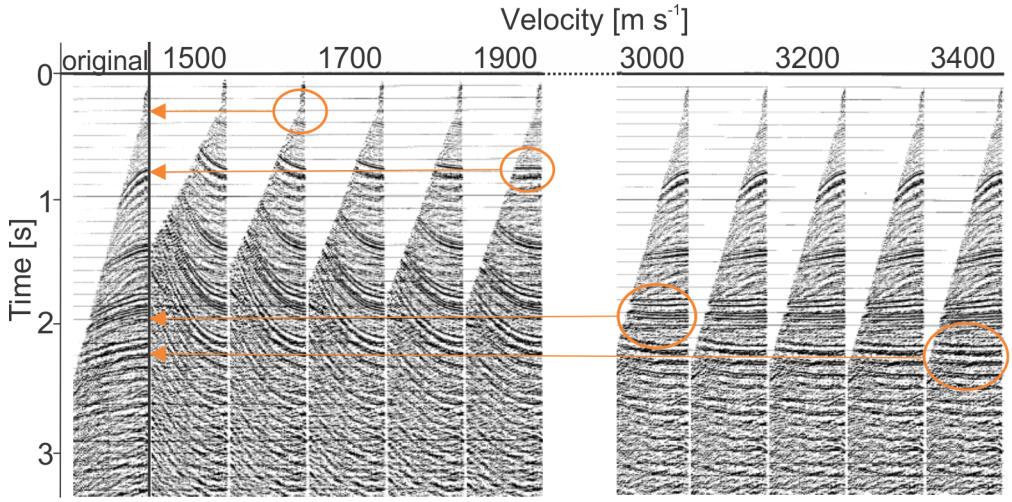

Figure 4.11.: Example of a CVS. The column on the left displays the original data. The second to the last column are NMO corrected with velocities ranging from 1500 to 3400 m s^{-1} (Modified after Yilmaz, 2001, Fig. 3.2-4. page 293–294).

through the whole dataset. A higher accuracy in velocity at every CMP, not only at selected (like CVS) can be achieved. To determine the velocity, the semblance spectrum of the traces is incorporated. Semblance is the ratio of output and input energy and is a measure of coherency. The semblance is illustrated in a coloured plot of velocity against depth (Figure 4.12 (B)). Figure 4.12 (A) shows a CMP gather with visible reflections, to which red hyperbolas are fitted. A hyperbola is fitted to a reflection by assuming a velocity. In the corresponding semblance plot (Figure 4.12 (B)) the velocity is marked by a cross. Dark colour like green represent a high semblance value respectively a high energy/coherency. Interval velocities, automatically calculated by the picked RMS velocities, are displayed as a blue line in the semblance plot. The initial CMP gather after the NMO correction on base of the picked velocities is shown in Figure 4.12 (C).

No reflections are visible within this dataset. Hence fitting hyperbolas to reflections using the HVA is not possible. Consequently, the semblance analysis, incorporated in the HVA, as well as the CVS are the remaining tools to analyze the velocity.

I chose a velocity range for the CVS between 500 and 3500 m s^{-1} for the first 0.1 s of all shots of the P-wave. The FIT is expected to be in approximately 90 m depth, which would correspond (depending on the velocity) to a TWT of approximately 0.1 s. Since it was not clear which signals should be lined up, it was not possible to derive velocities using the CVS method.

Finally, I applied the NMO correction by means of velocities derived from measured core densities. From these densities I calculated the P- and S-wave velocities based on Equation 1.2 by Kohnen (1972) and Equation 1.3 by Diez et al. (2014).

4.1.7. Stack and depth conversion

Stack

During stacking the trace amplitudes in a NMO corrected CMP gather are summed up and divided by the number of traces along the offset axis. Thereby, reflections are amplified, since they should contain the same phase whereas random noise, containing random amplitudes and phase might be canceled out. This results in one remaining trace per CMP.

A high fold of coverage may improve the SNR for most data in the stacking process. The before described method is called a mean stack (here just referred to as stack). In contrast a

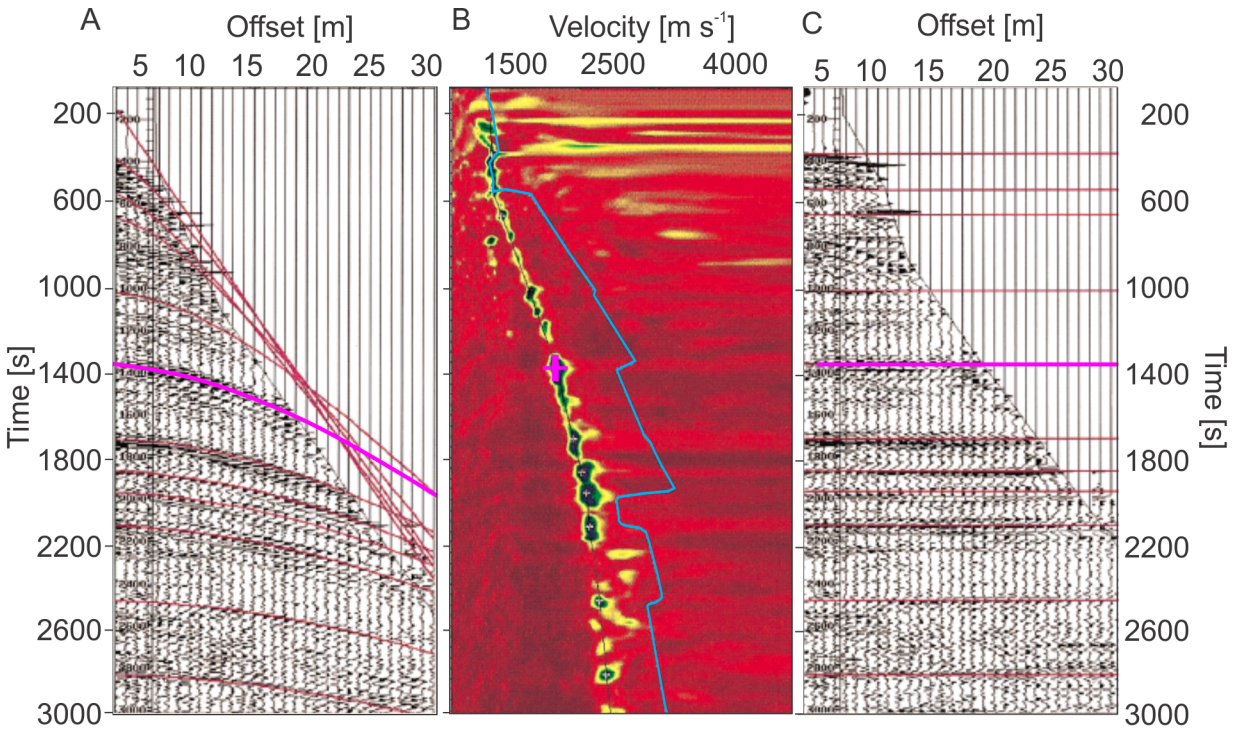

Figure 4.12.: Method of the HVA. A) A CMP gather with fitted hyperbolas (red). The velocities corresponding to the moveout of the hyperbolas are marked in B) the velocity-depth plot (RMS velocity) by a cross. The colours in the plot display the semblance. Green and blue represent good coherence, with decreasing value to yellow and red. The blue line displays the corresponding interval velocities. C) CMP gather as in (A), but after the correction for NMO, with the picked RMS velocities. E.g. a pink hyperbola is fitted to a reflection and the corresponding RMS velocity is marked by the pink cross (Modified after Yilmaz, 2001, Fig. 3.2–27. page 313).

median stack delineates that the amplitude is less decisive but the amount of occurrence of a certain amplitude plays a role. Consequently, a single trace with a high amplitude at a certain time, but only very low amplitude values at the same time in other traces of the CMP does not affect the median stack as much as the mean stack would be, since these two stacks differ in the way of scaling amplitudes (Kearey et al., 2002; Reynolds, 2011).

Depth conversion

The interpretation of seismic data is most often done in the t-x domain. An inconstant velocity model can produce false height. For instance a thick high velocity layer could be mapped as a layer overlying a topographic height in the t-x domain. Therefore, data should be converted into depth. The depth model derived after conversion minimizes the difference between times derived by normal-incidence ray tracing and zero-offset picked traveltimes. For the conversion a velocity model, defining interval velocities for different mTT and thus layers is needed (Etris et al., 2001; Keydar et al., 1989).

Similar to the NMO correction, the depth conversion was carried out by means of velocities derived from ice-core densities. The results in NMO correction and depth conversion based on velocities derived from core density and diving waves (Chapter 4.2) are compared.

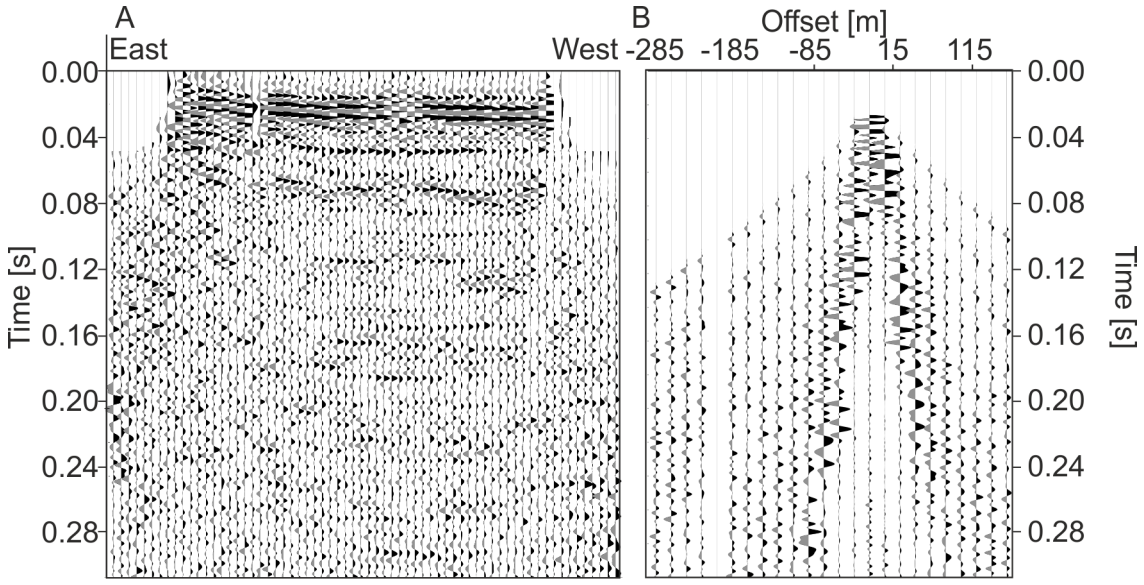

Figure 4.13.: Comparison of stacked NMO-corrected P-wave data and a P-wave CDP gather corrected for NMO. A) Stack of raw P-wave CDP gathers corrected for NMO of the parallel profile down to a depth of 0.3 s. B) NMO corrected P-wave CDP gather.

4.1.8. Evaluation of high amplitude signals in the unfiltered stack

The stack of raw CDP gathers corrected for NMO shows some high amplitude signals, which could be identified as possible reflection signal (for instance like done by Schulz (2013)). The evaluation of the high amplitude signals was done by the comparison of the mTT of the signal in the stack and the signal at this mTT in a CDP gather or shot, example shown in Figure 4.13. High amplitude signals are here referred to as "events". An event at 0.06 s mTT can be observed in the stack, referred to as event 5 (Figure 4.13 (A)). Signals in the NMO corrected CDP gather at 0.06 s mTT (Figure 4.13 (B)) were examined. In the following shots and CDP gathers will be considered and a possible origin of this signal is proposed. Therefore, the amount of traces containing a signal at this time as well as the appearance of this signal in the t-x domain was evaluated. This was done for events to a depth of 0.3 s. Additionally, a median stack and a far offset stack (containing only the far offsets) are created for comparison. Diving wave and multiple first breaks are muted with a ramp length of 0.004 s.

4.2. Diving-wave analysis

Diving-wave inversion consists of two different processing steps. The first step is fitting an exponential curve to offset-traveltime pairs of diving waves. Based on the slope of this curve the velocity is calculated. The second step is the Herglotz-Wiechert inversion. This inversion uses the fact that the velocity at the deepest point of the ray equals the reciprocal of the ray parameter p. An assumption for both processing steps is an increasing velocity with depth, further information can be found in Diez et al. (2013); Kirchner and Bentley (1990); Slichter (1932).

The persistent densification of firn (Chapter 1.2.1) results in a continuous, but non-linear increase in velocity with depth. The ice core B40 at Kohnen Station shows small scale density variations (Figure 3.4). These variations cannot be resolved in the vibroseis data. Hence, the fluctuations can be neglected and a continuous velocity increase is feasible. An assumption of a homogeneously layered model for the firn column is inaccurate because it depends on the number of layers describing the firn column. Therefore, a mathematical idealization of curved ray path is applied.

The picking of offset-traveltime pairs was performed with ECHOS. The processing was performed with the Software MATLAB R2016a, developed by MathWorks. The fit of the offset-traveltime pairs was performed by the Curve Fitting Toolbox, an in-build function of MATLAB. The used MATLAB scripts can be found in the Appendix A.3.

In the following sub-chapter the picking of diving waves as well as the related data processing is described. The processing should enhance first break visibility. Furthermore, the fitting of these picks to the exponential function and the Herglotz-Wiechert inversion is described. Finally, the calculation of seismic velocities and elastic moduli is described.

4.2.1. Pick of diving waves

The first break visibility of diving waves was improved by bandpass filtering. The amplitude spectrum above the first breaks showed differences for shots inside the geophone line and shots outside the geophone line, that is why the shots are separated in the same groups (group 1–3) already described before. The passband contained frequencies between 120–240 Hz and 140–240 Hz with a ramp of 20 Hz. The diving wave spectrum contained a high amplitude around frequencies of 160 Hz, which was observed to be more or less continuous over the whole profile. For consistency reasons I picked first breaks always at the phase transition of a small positive amplitude to a higher negative amplitude, as it is shown in Figure 4.14 (A). First breaks could not be picked for offsets smaller than 15 m in the parallel profile. In the perpendicular profile the first breaks were picked for offsets between 17 and 85 m.

Traveltime discontinuities for traces with the same offset, but different directions (W-E, E-W) on the same profile, could be observed for some shots. Offsets in the western direction are from now on referred to as negative offsets, whereas offsets in eastern direction are referred to as positive offsets. Figure 4.14 shows shot 20 and 22 with picked first breaks of the diving wave. Corresponding positive and negative offsets in shot 22 present similar traveltimes, in contrast, traveltimes of equal absolute offsets in shot 20 differ. Therefore, the secondary header for the pick was chosen to be SOFFSET (specifies the source to receiver signed offset) to enable separate picking for negative and positive offsets.

I picked the first breaks of P waves for every shot in the vertical component, likewise for the horizontal component of the S wave (longitudinal component for the SV wave and transverse for the SH wave). There are two different ways for traveltime picking. Firstly, the tool MUTE enables traveltime picking for every shot separately. This tool projects a predicted pick on base of former picks (if available). This is helpful in noisy data or in cases, where it is

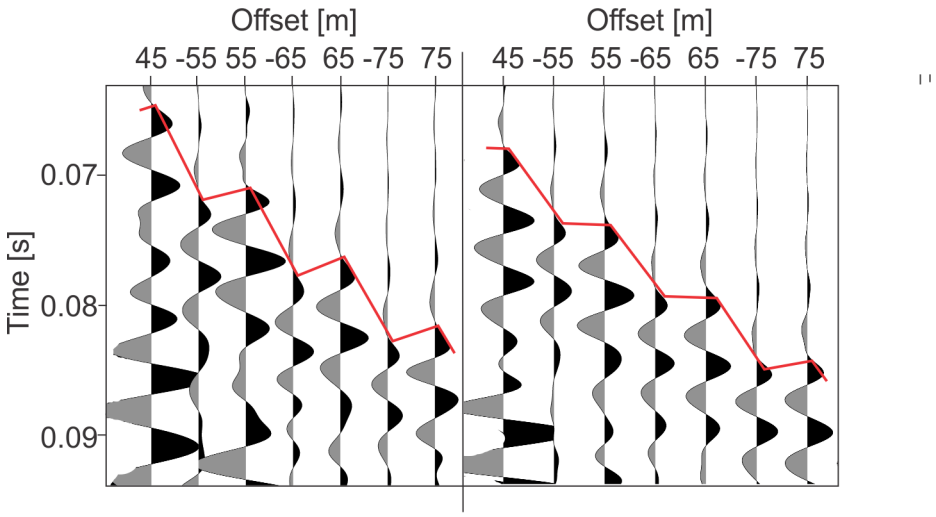

Figure 4.14.: Comparison of offset-traveltime pairs of shot 20 and 22. A) SH-wave shot 20 with picked traveltime for the diving wave first breaks in red. Same positive and negative offsets do not show the same traveltime. B) SH-wave shot 22 with picked traveltime for the diving wave first breaks in red. Same positive and negative offsets do show the same traveltime. Shot 20 and 22 have a spacing of 20 m while the geophones remain in the same position.

likely to pick the wrong phase. The disadvantage of this picking method is, that it does save the suggested pick, if it is not deleted manually. This results in saved traveltimes for offsets suggested from the former shot, even if there is no traveltime recorded. Secondly, the FILTER tool TraceWidget pick utility can be used for traveltime picking. The method is less time consuming and more precise. Mute picking is possible when the processing flow is stopped at a specific processing step. For this data the processing flow was stopped at a FILTER tool and a mute was picked. This procedure also improves the pick quality, because data picked in the interactive MUTE tool provides three decimal digits, whereas a mute created by TraceWidget pick tool provides five decimal digits. Therefore, I chose to pick in the TraceWidget tool.

4.2.2. Herglotz-Wiechert inversion

Figure 4.15 (A) illustrates the diving wave principle as already introduced in Chapter 2.2. The figure introduces two different velocity types. First, the velocity v_D, derived from the curve-fitting Equation 4.6. Second, the apparent velocity $\tilde{v}$, defined as $\tilde{v}(x) = \frac{x}{t}$. Moreover, the wave front before emergence is described by S (Figure 4.15 (B)). The ratio of wave velocity to apparent velocity can be calculated by means of the initial angle of incidence i_o. At the deepest point of any ray path ($sin\ i = 90\ °$) the wave velocity equals the apparent velocity equals the inverse of the ray parameter p.

$$\tilde{v} = v_D = \frac{1}{p} \tag{4.3}$$

This relation enables assigning velocities to the corresponding depth and offsets. The depth can be calculated by the following equation (Slichter, 1932):

$$z_p = -\frac{1}{\pi} \int_0^D (\cosh^{-1}(\frac{v_D}{\tilde{v}(x)}))^{-1} dx \tag{4.4}$$

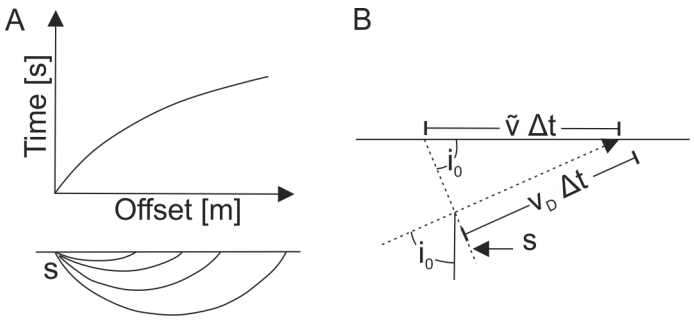

Figure 4.15.: Principle of diving waves: A) Exemplary diving wave with traveltime curve. B) Geometric relation of the gradient of the traveltime at the greatest offset D, v_D, and the apparent velocity, $\tilde{v}$ with the angle of incidence i_0 are shown. Δt describes the traveltime difference (Modified after Slichter, 1932).

where v_D is defined as the gradient of traveltime at the greatest offset D and $\tilde{v}$ the apparent velocity.

4.2.3. Curve fitting

Different algorithms exist for the fit of the data. The algorithm used here is called Levenberg-Marquardt algorithm, here narrowing of the variables is not possible, but start values can be provided by the user, or will be suggested/proposed by the algorithm. The picked offset-traveltime pairs are fitted with an exponential smoothing function:

$$t = a(1 - e^{-bx}) + c(1 - e^{-dx}) + ex \tag{4.5}$$

where a, b, c, d, e are constants and t and x the traveltime and offset. According to Kirchner and Bentley (1990) the velocity described by the slope of this function is increasing monotonically with depth (which was already mentioned as a mandatory). The velocity (v_D) is calculated by the derivations of time with offset:

$$v_D = (\frac{dt}{dx})^{-1} \tag{4.6}$$

Fitting of all shots separately for the individual components often diverge. The parameters in Equation 4.5 should be positive, additionally the parameters b and d should be larger than 0.2. These rough coefficients bounds were determined by analyzing the different fits. The variables for all shots of the corresponding component were used as start values for single-shot fitting. This was necessary because one shot did not provide enough grid points for the algorithm to calculate appropriate start values.

4.2.4. Calculation of velocity, density and elastic moduli

The derived variables were used for the calculation of velocity, depth and offset. Thus the empirical formula by Kohnen (1972) was used for the P-wave velocity. For S-wave velocities the relation postulated by Diez et al. (2014) was used.

Elastic moduli like the bulk modulus, shear modulus and poisson's ratio were calculated under the assumption of an isotropic medium using Equation 2.10–2.10. To avoid additional uncertainties the density from XCT measurements were used in combination with the velocities derived from diving-wave inversion.

Elastic moduli can be calculated from components of the elastic tensor under the assumption of an isotropic medium. These elastic moduli will be compared to elastic moduli derived by diving-wave velocities and XCT densities.

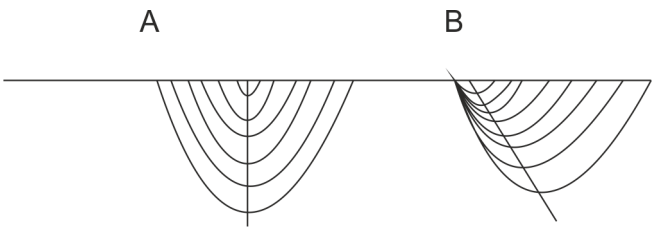

Figure 4.16.: Different diving-wave paths: A) Diving-wave path with the deepest point of the diving wave below one location. The velocity profile obtained by this diving wave is vertically orientated, as shown by the straight vertical line. B) Diving-wave path with an oblique orientated velocity profile.

I calculated the velocity and elastic moduli based on all picked offset-traveltime pairs for P, SH and SV wave independently. To analyze lateral variations I calculated velocities and elastic moduli based on data from three different locations. One in the west (location 303), one in the east (location 112) and one in the central part (location 267) of the parallel profile. For this calculation I sorted offset-traveltime pairs according to their distance to the first shot position. Location 303 has a distance of 303.5 m, location 267 a distance of 267.5 m and location 112 a distance of 112.5 m to the first shot position in the east. Thereby offset-traveltime pairs referred to location 303 contain the deepest point of their ray path below the position of location 303. Therefore the obtained velocity-depth profile is orientated vertically (Figure 4.16 (A)) and not oblique (Figure 4.16 (B)) within the subsurface.

5. Results

The primary aim of this thesis was to derive a velocity-depth profile and elastic parameters of firn and ice at Kohnen Station based on vibroseis measurements. For that purpose, reflections and diving waves can be used. The first part of this chapter describes the detection of reflections within the firn and ice at Kohnen Station. Therefore, intensive processing was necessary to make reflections detectable (Chapter 5.1.1). The shallow central part of the parallel stacked profile shows linear high amplitude signals (Chapter 5.1.2). The deeper part of the P-wave stack did also show a high amplitude signal. These high amplitude signals will be analyzed of their origin.

Another method to derive velocities is by diving-wave inversion (Chapter 5.2), which represents the second part of this thesis. The derived velocities are compared to velocities derived from ice-core densities. Furthermore, elastic moduli are calculated from velocities and XCT densities. These moduli are compared to moduli derived by the FEA.

5.1. Processing of reflection seismic data

The first subchapter is divided into two parts. In the first part the results of making reflection hyperbolas visible within the shots and CDP gathers (Chapter 5.1.1) are presented. The second part deals with the result of the evaluation of high amplitude signals in the shallow part and the evaluation of the high amplitude signals in the deeper part of the stack (Chapter 5.1.2).

5.1.1. Detection and identification of reflections

No reflection hyperbolas are visible within the raw data. The first attempt was to visualize potential reflections. Therefore, I tried to suppress ringing and groundroll. The groundroll has a very concise signal, influencing the whole shot in the f-k and t-x domain. Notch filters removed ringing for most shots outside the geophone line (first and second group). The application of notch and bandpass filters altered the amplitude spectrum of every group of shots. Table 5.1 summarizes the results of the processing steps applied to the data briefly. Figure 5.1 shows the amplitude spectrum of shot 1 (first group) after the application of notch and bandpass filters. The frequency content decreased from 30–240 Hz to 70–160 Hz as well as some low amplitude signal between 200–230 Hz (see for comparison the initial amplitude spectrum in Figure 4.1). The ringing in the third group is more persistent, especially at offsets less than 20 m. Therefore, for most traces of the third group, the ringing could only be removed by the application of a mute. The bandpass filter with a passband 100–240 Hz, applied for shots of the third group, weakened the signal of the groundroll but did not remove the high amplitude groundroll or lead to the visibility of reflections.

Targeted f-k filtering of linear events in the f-k spectrum of shots of the first group resulted in weakening of the low frequency, and faster part of the surface wave, highlighted in the blue edging in Figure 5.2. Figure 5.2 (A) shows the initial seismogram of a shot of group one and Figure 5.2 (B) the filtered seismogram. The comparison of shots before and after the application of a f-k filter also showed some time shifts in signals. The removal of linear events in the second group induced noise and was, thus, not used.

Table 5.1.: Results of the applied processing.

	initial frequency content [Hz]	**frequency content [Hz] after processing**	**result removal of ringing**	**result removal of groundroll**
P wave				
parallel profile				
group 1	30–240	70–160 & 200–230	notch & bandpass filter: removed ringing	f-k & K-L: removed partly but K-L induced noise
group 2	30–240	80–110 & 140–220	notch filter: removed ringing	f-k & K-L: no results
group 3	30–240	30–120 & 140–220	notch filter & mainly mute: removed ringing	f-k & K-L: no results
perpendicular profile	30–240	160–220	notch filter & mainly mute: removed ringing	f-k & K-L: no results
SH wave				
parallel profile				
group 1	40–300	50–130 & 160–240	notch & bandpass filter: removed partly ringing but induced noise	f-k & K-L: no result
group 2	40–300	140–210 & 240–300	notch filter & mute: removed partly ringing but induced noise	f-k & K-L: no results
group 3	40–300	40–120 & 140–300	notch & bandpass filter & mainly mute: removed partly ringing but induced noise	f-k & K-L: no results
SV wave				
parallel profile				
group 1	40–300	150–180 & 220–280	notch & bandpass filter: removed ringing	f-k & K-L: removed partly but K-L induced noise
group 2	40–300	150–220 & 240–300	notch filter & mute: removed ringing	f-k & K-L: no results
group 3	40–300	160–300	notch filter & mainly mute: removed partly ringing but induced noise	f-k & K-L: no results

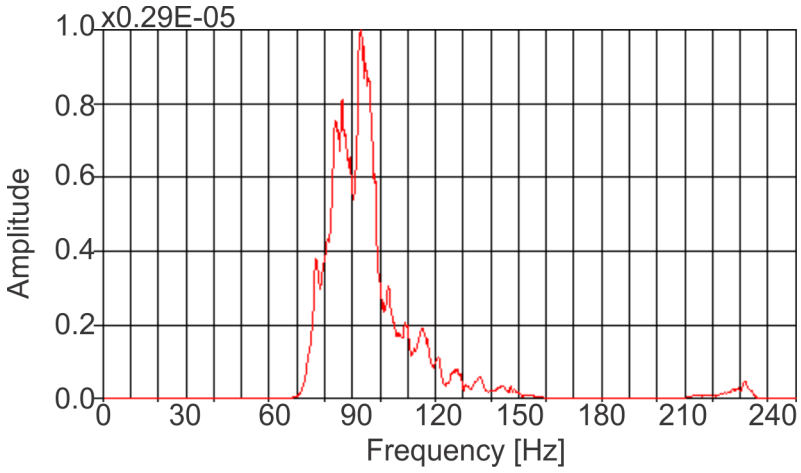

Figure 5.1.: Amplitude spectrum of P-wave shot 1 of the first group after applying notch filters with frequencies of 50 Hz, 130 Hz and 230 Hz.

One of the two sections marked in Figure 4.9 lined up by correcting the shots for linear moveout. This section could be removed by filtering of eigenfunctions, which is shown in Figure 5.3(blue edging). A velocity of 200 m s^{-1} was chosen for the moveout correction. During moveout correction the bending of high amplitude groundroll was clearly visible. A change in signal can be observed by comparing for instance the first trace between 0.00–0.05 s before (Figure 5.3 (A)) and after (Figure 5.3 (B)) the filtering of eigenfunctions. The first break of the diving wave can be observed in the original trace at about 0.02 s mTT, which represents the first recorded signal, the high amplitudes observed before 0.02 s mTT after the filtering of eigenfunctions can be associated to induced noise. Furthermore, the signal of the first breaks of diving waves is lost in some traces. The induction of noise and the loss of signals in individual traces highlights the sensibility of the transformation. The attempt to remove the signal of the diving wave along the whole shot by filtering of eigenfunctions did not remove the signal, because these do not appear linear in the seismogram and thus cannot align horizontally by a linear moveout correction.

The effect of different processing steps applied for different offsets became obvious after sorting the data for CDP. A significant change in trace amplitude could be observed between traces of the second and third group. The described processing routine did not improve the SNR in shots of the third group, thus traces with offsets less than 50 m were muted. In contrast, the shots of the first and second group showed a lower amplitude after processing for the surface wave, compared to the raw data.

These processing tools did not enhance the detection of reflections in the parallel and perpendicular profile. This led to poor results for the semblance calculations and inhibited the velocity analysis by means of the HVA or CVS. A plot of the semblance for P-wave shots of the second group (parallel profile) is shown in Figure 5.4. A maximum in coherence is visible for velocities between 900–1300 m s^{-1} above 0.3 s mTT. These values are not consistent with empirical values (Table 1.1). The CVS with a certain velocity range aligned a few high amplitude signals, but an alignment along the whole CDP gather or shot could not be observed. Data corrected for NMO with velocities derived from ice-core measurements and data corrected with velocities form diving-wave inversion did not show any significant change.

Anomalies observed during processing

During data processing a polarity reversal of the P wave in the parallel profile was observed. Figure 5.5 shows shot 29 and 31, with a zoom on the first breaks. From shot 1–30 (Fig-

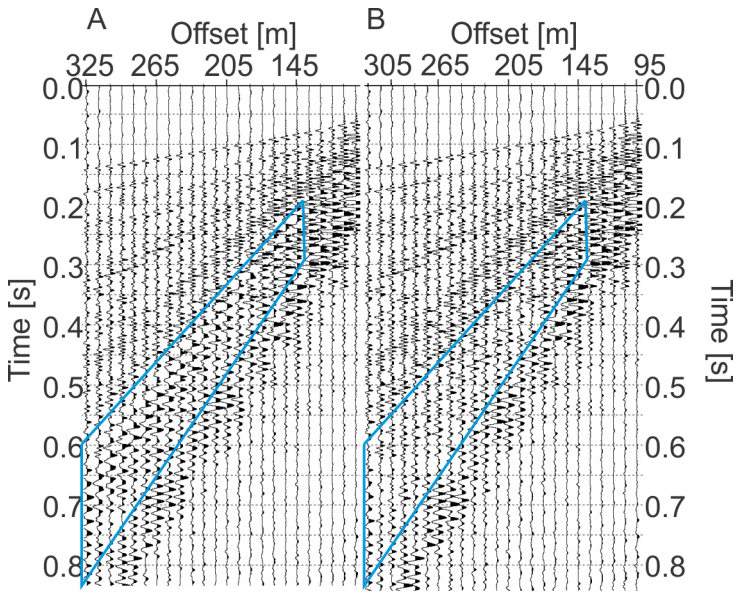

Figure 5.2.: A) Seismogram of a raw P-wave shot of the first group. B) Seismogram after the f-k filter. The area in the f-k spectrum that is supposed to be removed by the f-k filter can be seen highlighted in red in Figure 4.8. The blue edging inside the seismogram marks the area of the most striking change.

ure 5.5 (A)) the signal is defined by a phase sequence positive-negative-positive. From shot 31 to shot 129 (Figure 5.5 (B)) the polarity changes to negative-positive-negative. A signal with a positive polarity at a certain time would be canceled out during stacking if a signal with a similar amplitude but negative polarity occurs at the same mTT (after NMO correction). Thus, a polarity reversal was applied on the first 30 shots by the tool EDIT before stacking. This did not improve the stack.

The first five P-wave shots of the perpendicular profile showed some noise with a hyperbolic shape (Figure 5.6). The hyperbola apex is not located at the smallest offset but somewhere outside the recording. The structures can be seen through the whole shot gather. The hyperbolic shape is highlighted in violet (Figure 5.6). Determining velocities of hyperbolic structure 1 results in a velocity of 450 m s^{-1} at 0.56 s mTT and 1070 m s^{-1} at 1.10 s mTT. These hyperbolas can be seen in all three components with the similar velocities at the same mTT. The amplitude spectrum of these structures indicate a low frequency, less than 80 Hz. I applied a bandpass filter, with a passband from 80–240 Hz to remove this signal.

Additionally, the stacked P-wave data of the perpendicular profile shows a wavy structure, highlighted in blue in Figure 5.7. These structures are enhanced by individual muting of bad traces. Nevertheless, the non-linear high amplitude trend creates a scattered stack. These structures might be characterized by two phases and can be seen in all three components. The amplitude spectrum of these wavy structures at traveltime 1.55–1.70 s shows a peak between 180–220 Hz. In contrast, shallower wavy structures at 0.55–0.7 s show a frequency peak at 120 Hz. Therefore, these structures could not have been removed by frequency filtering.

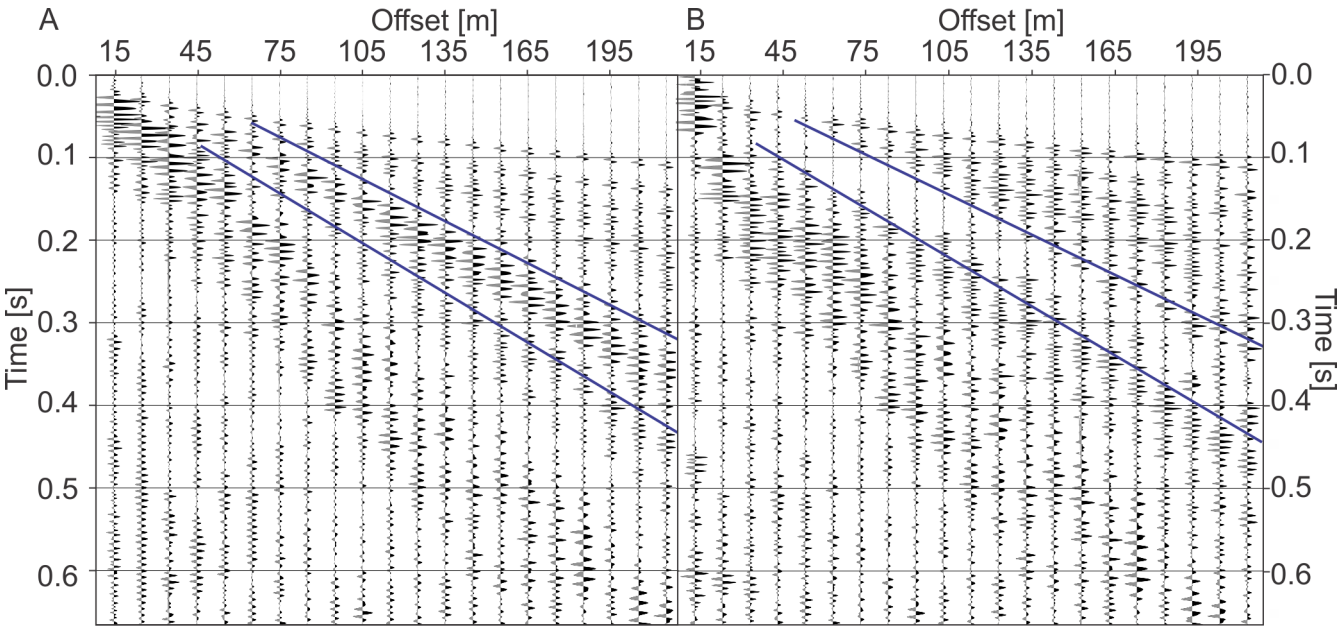

Figure 5.3.: A) Bandpass filtered P-wave shot of the first group. B) Shot 25 after filtering of eigenfunctions with a moveout correction with a velocity of 200 m s^{-1}. The blue edging inside the seismogram marks the area of the most striking change.

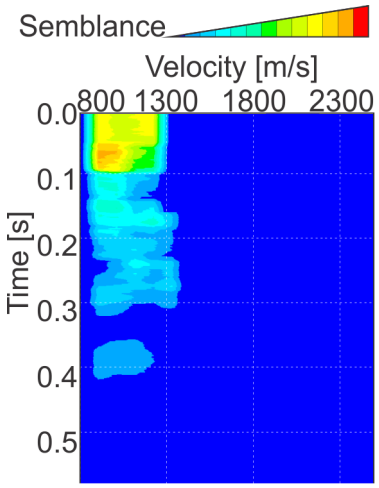

Figure 5.4.: Semblance plot of second group P-wave shot. The plot displays velocity on the horizontal and time on the vertical axis. Red colour represent high semblance value, decreasing to blue, with a low semblance value.

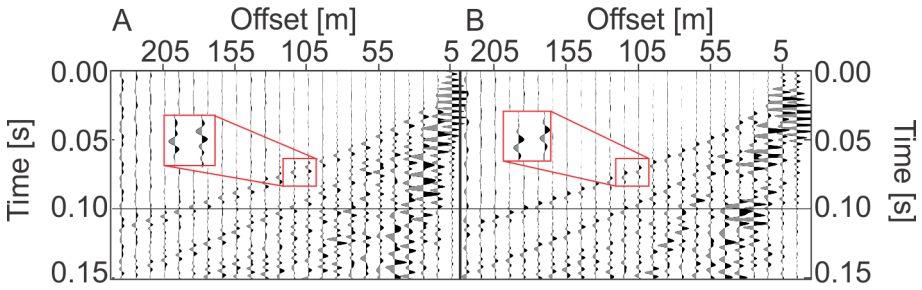

Figure 5.5.: Comparison of the vertical component of A) P-wave shot 29 and B) P-wave shot 31 in the profile parallel to the ice divide. Close up (red box) shows the first breaks polarity reversal.

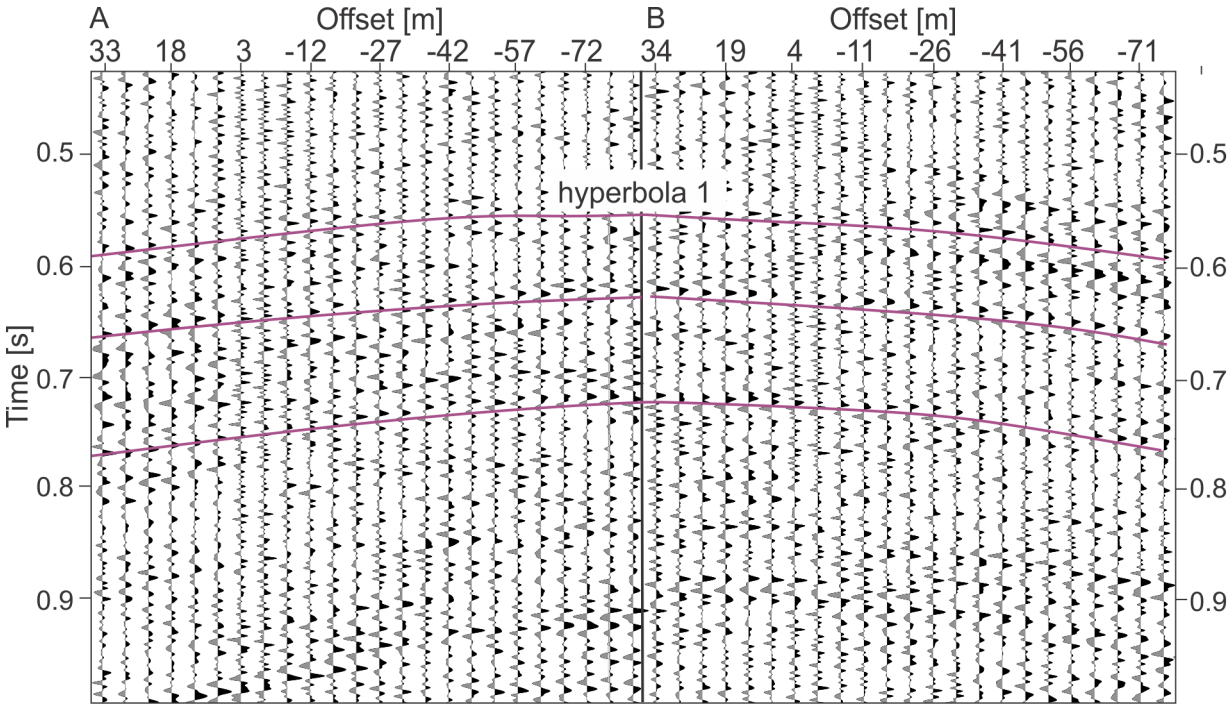

Figure 5.6.: Hyperbolic structures seen in the first five shots of the P wave in the perpendicular profile.

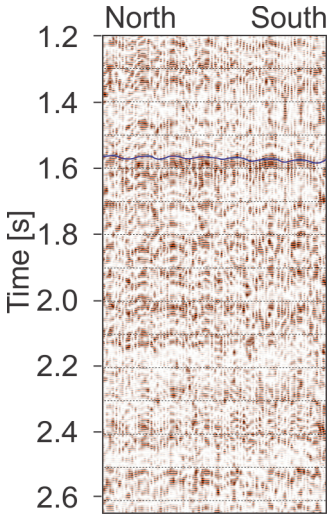

Figure 5.7.: Stack of processed vertical component P-wave data of the perpendicular profile. The wavy structure, highlighted in red, can be seen for several traveltimes.

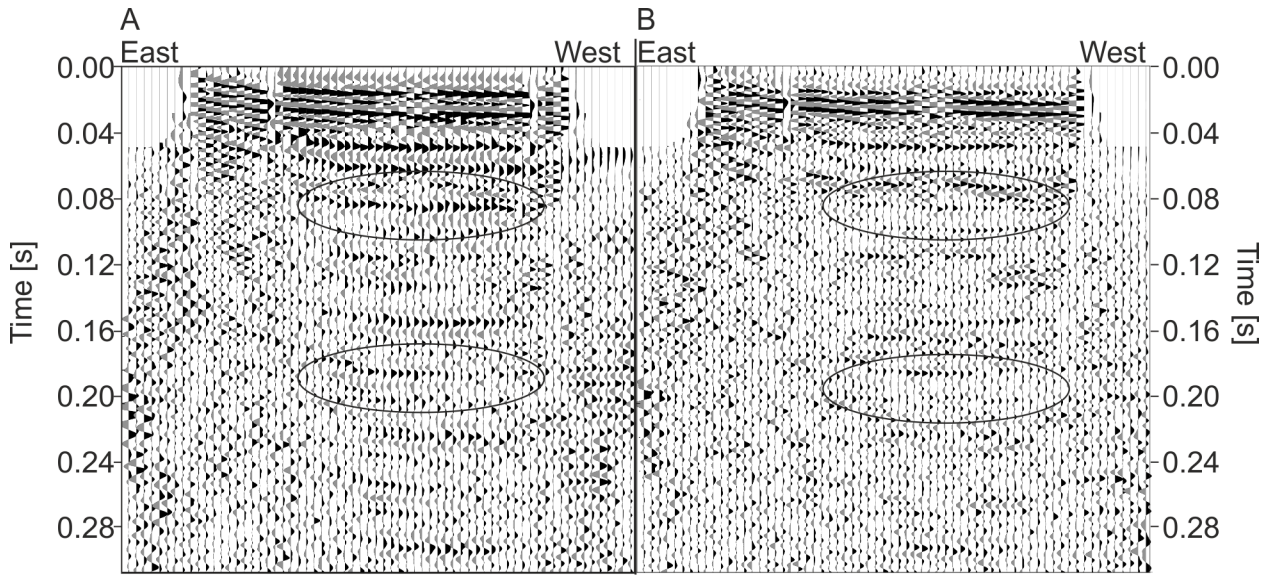

Figure 5.8.: A) Stack of the vertical P-wave component after processing. B) Stack of the unfiltered vertical P-wave component. Ellipses highlight exemplary areas of change.

5.1.2. Evaluation of the stacked data

The stack of the processed NMO-corrected data differs from the stack of raw data corrected for NMO. The events in the two stacks are partly time shifted and the event amplitudes are weaker (Figure 5.8). Induced noise above 0.02 s mTT can be traced back to the K-L transformation. Since the described processing did not significantly improve the SNR or remove the groundroll, the investigation of the origin of the high amplitudes signal was performed with the stack of NMO-corrected raw data, raw shots and CDP gathers.

High amplitude signal in the shallow part of the stack

The occurrence of the high amplitude signal in the shallow part of the stack is summarized in Table 5.2 but also described in the following. Figure 5.9 (A) shows the stack of raw P-wave data of the parallel profile with labelling of the high amplitude events described below. Figure 5.9 (B) shows an exemplary NMO corrected shot for the comparison of different high amplitude signals. The profile shows a trough flank shape of the subsurface (Figure 5.9 (A), solid blue line). The signals at the ends of the stacked profile are more scattered and not as clear as in the central part. Additionally, with increasing depth the signal gets more scattered towards the center and the flank shape seems to shift towards the central part of the stack with increasing depth (indicated by the dashed line in Figure 5.9 (A)). For the first 0.045 s mTT the median stack shows a similar result compared to the mean stack (Figure 5.10). Below that depth the median stack shows a quiet zone (marked by the rectangle in Figure 5.10 (A)) until 0.24 s mTT for CDP gather 9–58. Higher amplitudes are visible in the median stack when scaling is adapted, nevertheless, not as clear as in the (mean) stack.

Diving waves first breaks in P-wave shots can be observed at 0.034 s mTT for offsets larger 25 m (Figure 5.9 (B)). Muting of the diving wave resulted in no events above 0.09 s mTT in the stacked profile in Figure 5.9 (A). Consequently, events 1-7 disappear.

Back tracing of event 8 at 0.112 s mTT (Figure 5.9 (A)) showed that 3 of 8 traces of a CDP gather contain a high amplitude at this mTT (Figure 5.9 (B)). These high amplitudes have their origin in the high amplitude, low velocity groundroll. Similar is the case for the following events (event 9–13).

Events 1–13 disappear, if all traces with offsets smaller than 150 m are muted. If only the

Table 5.2.: Comparison of shallow high amplitude signals in the different stacks.

	parallel profile P wave	**parallel profile S wave (SH & SV)**	**perpendicular profile P wave**
stack raw data all offsets	several horizontal events	several horizontal events	events with wavy structure, stack looks very scattered
stack raw data only far offsets	no clear horizontal events	no clear horizontal events	
stack raw data only near offsets	very clear periodic individual events	very clear periodic individual events	periodic events, hard to detect due to wavy structure
median stack raw data all offsets	no clear horizontal events below 0.04 s	no clear horizontal events below 0.04 s	no clear horizontal events and very scattered stack
stack of filtered data	similar events as in raw data stack but partly weaker amplitude	similar events as in raw data stack but partly weaker amplitude	more scattering than in raw data stack

traces of the first group are stacked (in total 384 traces), no continuous high amplitude signals or horizontal sections with higher amplitude can be seen. Stacking only traces with offsets smaller than 50 m, the events above 0.2 s become more clear. A periodicity of the events at an interval of approximately 0.04 s is clearly visible in the vertical, as well as horizontal components (Figure 5.11 (A-D)). The mTT of the high amplitude signals of the near offset traces matches with the traveltime of a high amplitude signal in the stack.

The periodic signals in the S wave of the parallel profile shows a similar time interval when compared to the P-wave data. Again the time of the stacked signal matches the signal in the near offset traces (Figure 5.11 (E-H)). The high amplitude signals are visible in all three components (vertical, horizontal 1 and horizontal 2) for P and S waves. Additionally, an amplitude decay proportional to the reciprocal of traveltime can be observes (under the assumption of a linear moveout).

After depth conversion, the depth for events in the P-wave data is not consistent with the depth of events in the S-wave data. Lateral variations of the high amplitude signals can be seen along the parallel profile generating a trough flank shape (Figure 5.12 (A)). The amplitude spectrum of these signals is shown in Figure 5.12 (B). The high amplitude signals seen in shots in the east of the parallel profile shows shorter mTT when compared to shots in the west. Under the assumption of a linear moveout I estimated a velocity of this signals of 490 $\mathrm{m\,s^{-1}}$ for shot 31 in the east and 260 $\mathrm{m\,s^{-1}}$ for shot 88 in the west.

The stack of the perpendicular profile, shows lots of scattering and no individual events, as seen in the stacked parallel profile. The near offset traces in this profile show even more high amplitude signals in a periodic interval of 0.02 s, decreasing with depth (Figure A.6 in the Appendix).

High amplitude signal at 1.63 s mTT

A high amplitude signal at approximately 1.63 s mTT is pronounced after stacking of vertical components of P-wave CDP gathers with offsets smaller 30 m. This high amplitude signal seems to be dipping upwards towards the east, although no continuous event can be seen dipping upwards (Figure 5.13 (A), an additional stack in wiggle mode is shown in Figure A.8

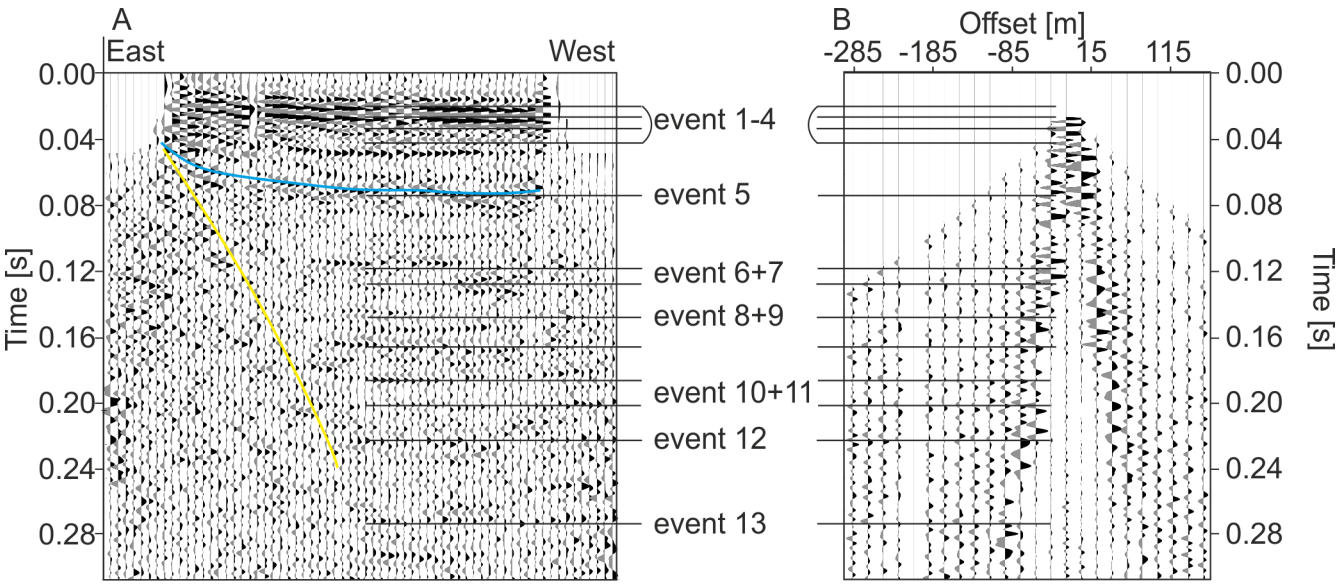

Figure 5.9.: Comparison of stacked NMO-corrected P-wave data and a P-wave shot corrected for NMO. A) Stack of raw P-wave CDP gathers corrected for NMO of the parallel profile down to a depth of 0.3 s. Events numbered from 1 to 13 are described below. The blue solid line indicates the shape of the trough flank that can be seen in the profile. The dashed line indicates the shift of the trough flank with depth. B) NMO corrected P-wave CDP gathers.

in the Appendix). The occurrence of this signal for different stacking techniques is summarized in Table 5.3. Low frequency noise around 80 Hz is visible at far offsets in the vertical component of the parallel profile (Figure 5.13 (C)). I applied a bandpass filter with a passband from 100–240 Hz to remove this noise. After filtering of the traces the high amplitude signal in 1.63 s traveltime can still not be seen when stacking all offsets. Therefore, investigations concerning this signal are always referred to the stack of traces with an offset less 30 m. Similar to the high amplitude signal at 1.63 s mTT a signal with lower amplitude can be seen for a mTT of 1.85 s.

The comparison of stack of traces with offset less 30 m and the median stack of theses traces shows a weaker amplitude in the median stack, but the signal in 1.63 s mTT is still visible. I tried to apply a CVS to this high amplitude signal, but the resulting moveout of different applied velocities is too small to observe changes in the stacked data.

The horizontal components of the P wave do not contain a higher amplitude signal at 1.63 s mTT. No high amplitude signal at mTT 1.63 s can be seen in the stack of S-wave data in all components but a slightly higher amplitude, compared to the surrounding amplitudes at 3.33–3.37 s as well as 4.40–4.44 s. These higher amplitudes appear in the raw data stack at a frequency around 160 Hz. During processing I applied a notch filter with 160 Hz to remove ringing. Therefore, this event is not visible in the filtered stack. In comparison, the spectrum of the high amplitude signal at 1.63 s in the P wave does not consist of a spike (Figure 5.13 (B)). Therefore the high amplitude signal in the P-wave data can still be seen after processing, including notch filters.

The stacked perpendicular profile shows a higher amplitude at 1.58–1.65 s and 1.8–1.85 s for the vertical component of the P wave. This high amplitude is not as clear as in the parallel profile, especially when the wavy structure interferes with the high amplitude event. An increased amplitude can also be seen in the horizontal components, albeit not as clear as in the vertical component.

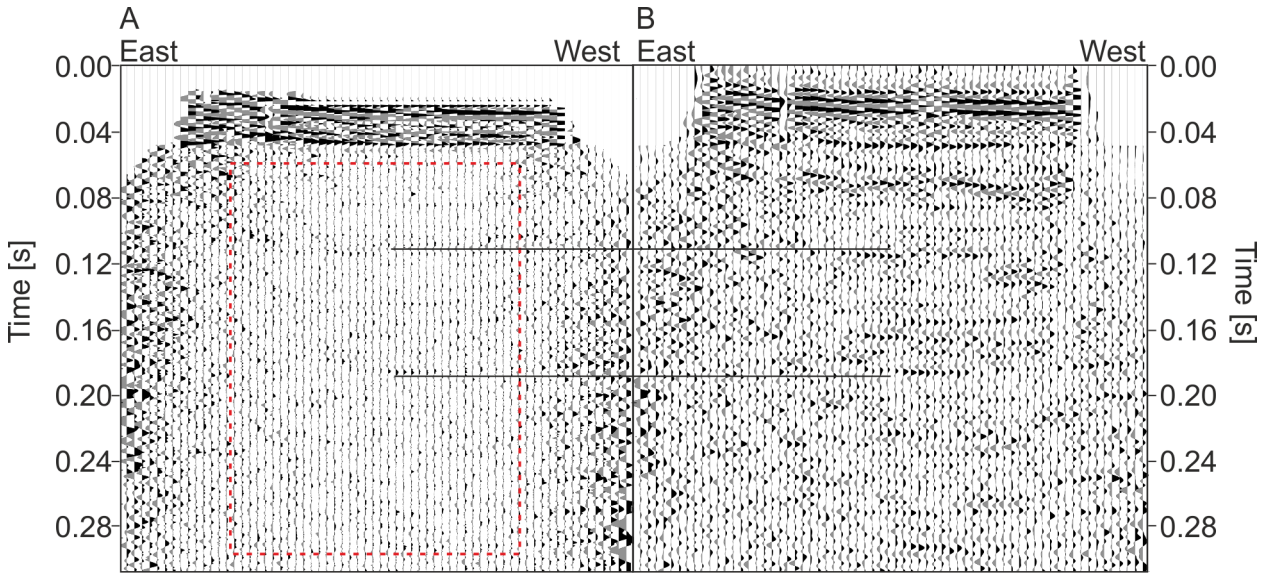

Figure 5.10.: Comparison of mean and median stack of NMO corrected P-wave data (parallel profile). A) Median stack of P-wave data in the parallel profile. The red rectangle indicates the quiet zone B) (Mean) stack of P-wave data in the parallel profile.

Table 5.3.: Comparison of deep high amplitude signals in the different stacks.

	parallel profile P wave	**parallel profile S wave (SH & SV)**	**perpendicular profile P wave**
stack raw data all offsets	no high amplitude signal visible	no high amplitude signal visible	weak amplitude increase at 1.63 s mTT, stack looks very scattered
stack raw data near offset	high amplitude event at 1.63 s mTT	no high amplitude signal visible	weak amplitude increase at 1.63 s mTT, no linear event, stack looks very scattered
mean stack near offsets raw data	high amplitude signal at 1.63 s mTT	no high amplitude signal visible	weak amplitude increase at 1.63 s mTT, scattered signal

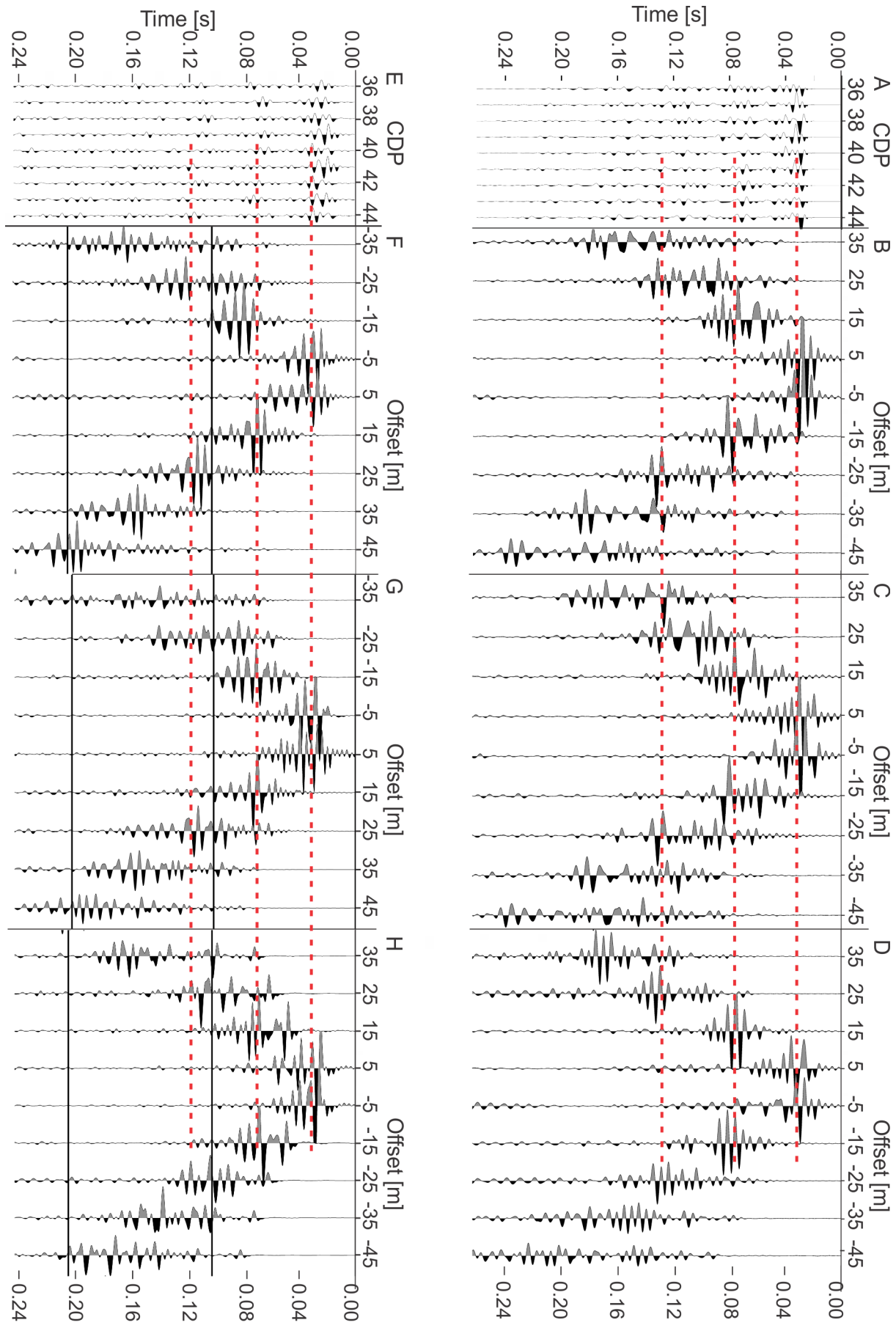

Figure 5.11.: Stack and components of P- and S-wave shots in the parallel profile. A) Stack of P-wave CDP gathers 36–44 until a depth of 0.25 s B-D) CDP gather 40 in the vertical (B) and horizontal (C and D) components. E) Stack of SH-wave CDP gathers 36-44 down to a depth of 0.25 s F–H) CDP gather 40 in the vertical (B) and horizontal (C and D) components.

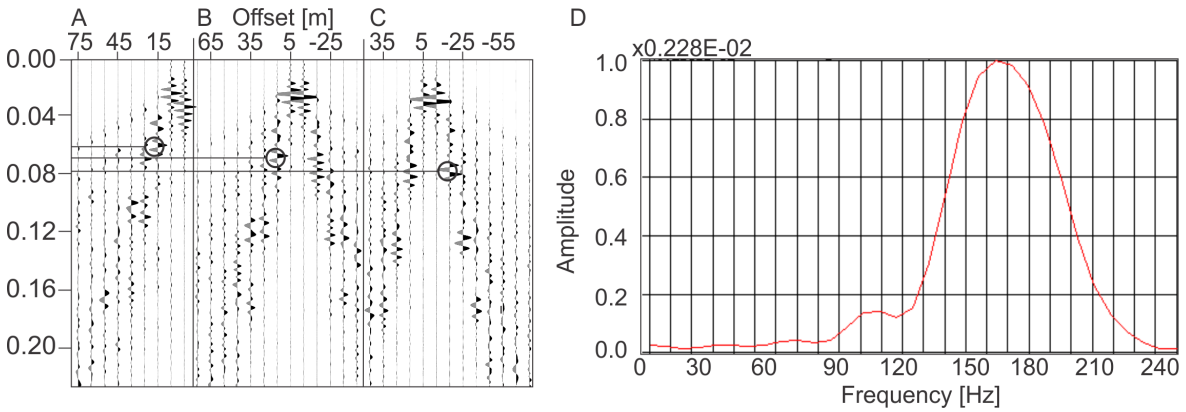

Figure 5.12.: Changes in the high amplitude signal in the vertical component of A) P-wave shot 31, B) P-wave shot 46 and C) P-wave shot 88. The high amplitude signal at an offset of 15 m is highlighted for every shot to visualize the change D) Amplitude spectrum of the high amplitude signal.

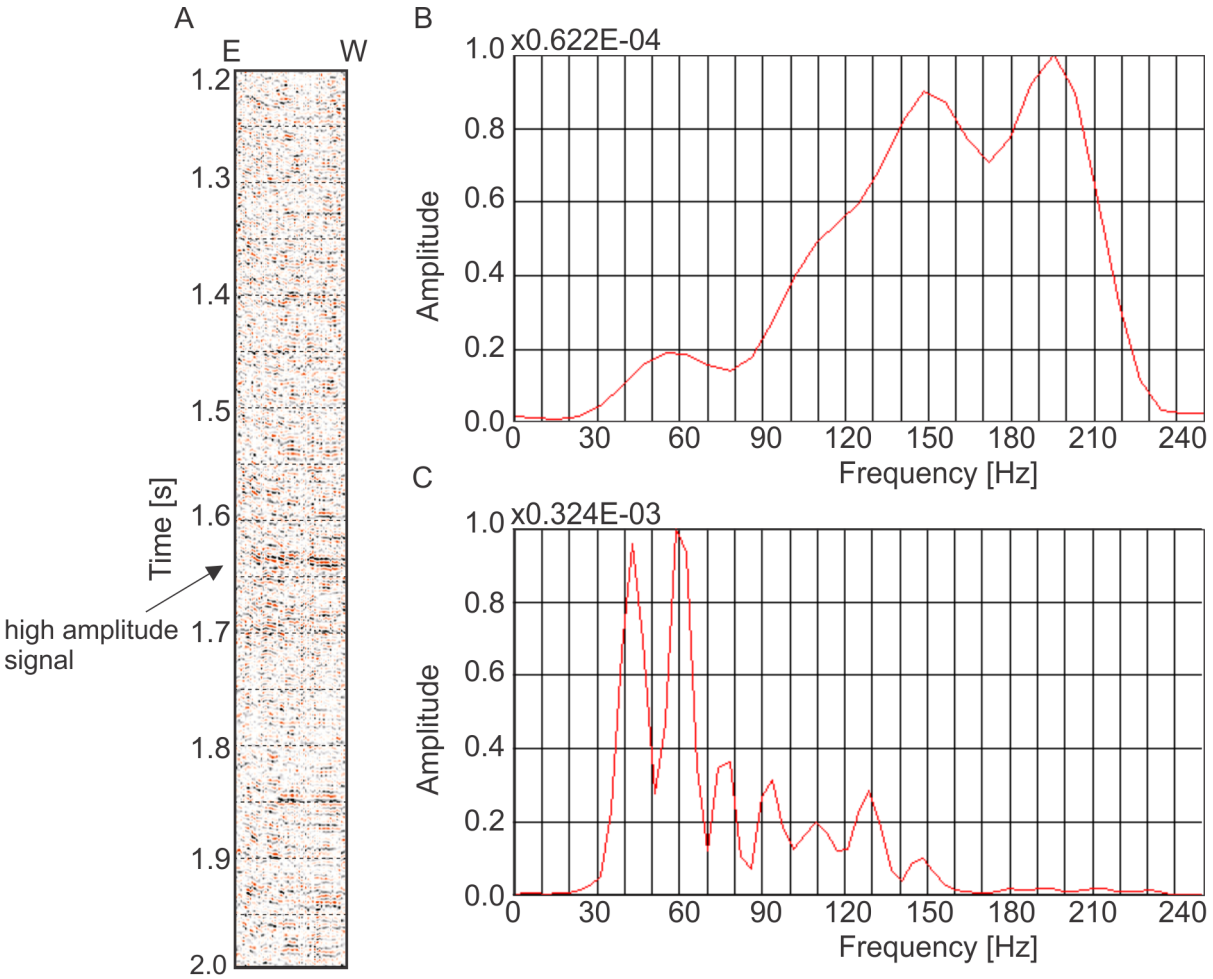

Figure 5.13.: A) Near offset stack of the NMO corrected P-wave CDP gathers recorded with the vertical component in the parallel profile. An amplitude increase can be seen at 1.63 s mTT. The stack with a wiggle display is shown in Figure A.8 in the Appendix. B) Amplitude spectrum of the high amplitude signal at 1.63 s traveltime. C) Amplitude spectrum for offsets larger 30 m at a mTT of 1.63 s.

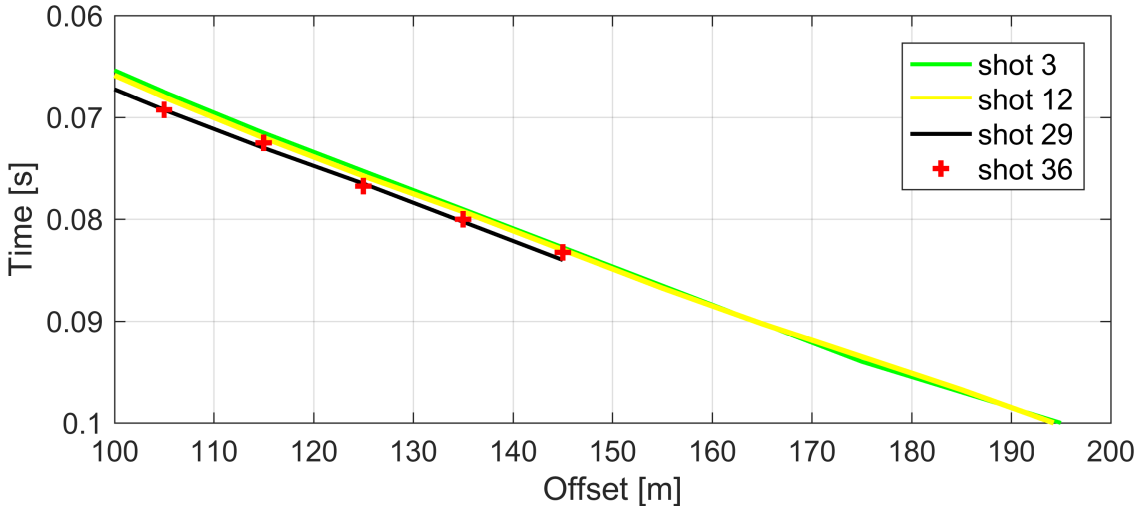

Figure 5.14.: Plot of offset-traveltime pairs for P-wave shot 3, 12, 29 and 36. Shots are labeled and taken from east to west (shot 3 represents offset-traveltime pairs of the east, likewise shot 36 of the west).

5.2. Diving wave analysis

During picking the diving wave first breaks small shifts from positive to negative phase could be observed in a few traces. Picking distortion during processing was prevented by picking raw data traveltimes.

Figure 5.14 shows five P-wave traveltime curves of the parallel profile. A gap in the traveltimes between shots on the west and east side of the seismic line as well as between far and near offset shots does not exist. The curves of the S-wave shots plot in a similar way, but at different traveltimes (Figure A.9 in the Appendix).

Figure 5.15 shows picked offset-traveltime pairs for all shots of both profiles. The picks of the SV wave (dark blue dots) do show a striking smaller traveltime (max. time difference 0.02 s for offset 70 m) when compared to the SH wave (red triangles and green dots). S- and P- wave data are clearly separated in this plot (max. time difference 0.025 s for offset 70 m). The comparison of the P-wave data of the parallel profile and the perpendicular profile shows generally smaller traveltime for shots of the perpendicular profile (max. time difference of 0.01 s for offset 60 m). The picks of the perpendicular profile scatter more at small offsets compared to the parallel profile. A difference between positive and negative offsets can be observed in shots within the geophone line (max. time difference of 0.004 s for offset 60 m). The difference is most dominant for shots of the perpendicular profile, where traveltimes for positive offsets (cyan dots) are plotted above (less traveltime) negative offsets (red dots, Figure 5.15). The differences are less significant in the parallel profile. Here the S-wave picks with positive offset seem to variate more with increasing offset. Traveltimes for negative offsets fit with traveltimes for positive offsets. This can also be seen in the P-wave data, although the P-wave picks show less variation.

Figure 5.16 shows a fit (black solid line) as well as the picked data of all SH-wave shots from the parallel profile (blue dots). The blue dashed line represent the fit within 68.3 % confidence bounds and a picking uncertainty of 0.002 s (respectively 0.0016 s for the P wave, not shown here). The fit to the picked data did not always converge. Therefore, red points display the scattering of constants a–e.

The fit for the perpendicular profile did show a lot of scattering, which did not result in satisfactory constants. Likewise, the fit of single shots, or only a range of shots did show a

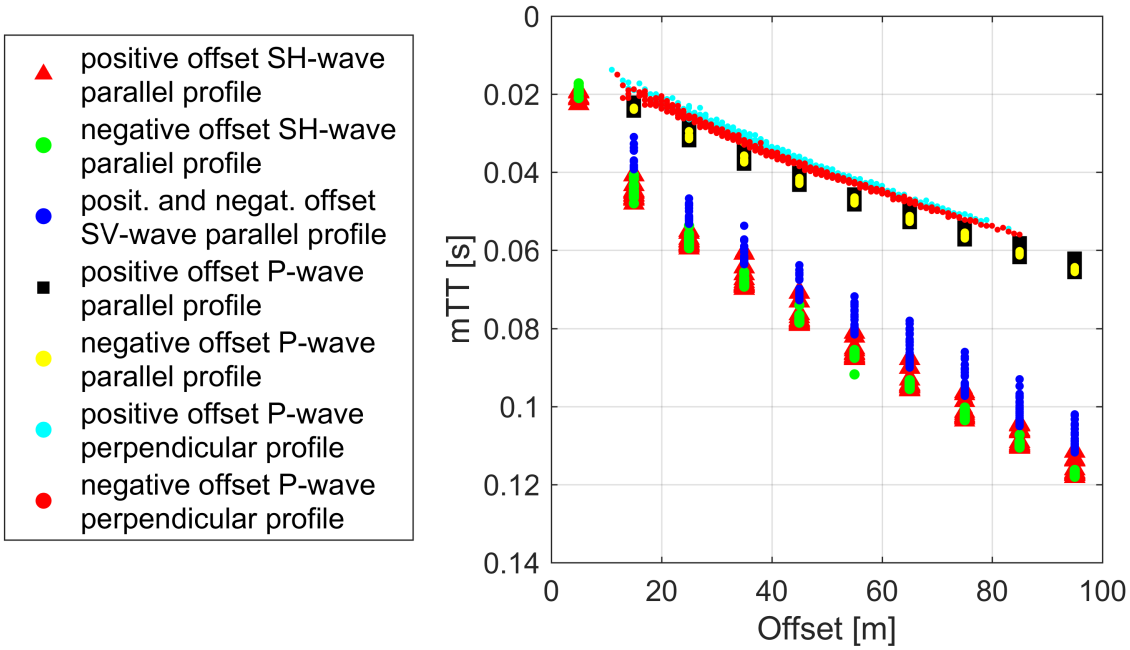

Figure 5.15.: Plot of all offset-traveltime pairs of the parallel and perpendicular profile. Negative offsets are denoted with a positive sign but a different colour to enhance visualization.

lot of scattering. Thus, a velocity profile could not have been derived for the perpendicular profile.

Uncertainty

The coloured area in the background of the following graphs indicate an one standard deviation error band for the velocity derived from diving wave inversion. The uncertainty of the traveltime-inversion velocity is thereby influenced by the variation of the constants (a–e), obtained by the fit of the traveltime curves to Equation 4.5, as well as the uncertainty in the pick. An uncertainty increase with depth can be observed for velocities derived from diving waves. The maximum uncertainty in a depth of 70 m is for the P wave 3.4 %, SV wave 7 % and for the SH wave 1.8 %. Error bars in the background indicate an one standard deviation error band for values derived from FEA. The uncertainty of this values depends on the uncertainty of the elastic properties in ice, assumed for the virtual experiments, uncertainties in the segmentation and spatial variations in density. Gerling (2016) investigated the uncertainty of the elastic tensor and postulates a maximal uncertainty of 18.2 % for the component c_{33}. This value was adopted to the other elastic tensors since all incorporate the same FEA and method. A better individual uncertainty could be received by the estimation and incorporation of lateral density variations and more accurate segmentation, for instance by analyzing more segments in one depth.

Calculated velocities and elastic moduli

Figure 5.17 shows the calculated seismic velocities with depth of the parallel profile (P-wave velocity=green, SH-wave velocity= red, SV-wave velocity=yellow). Additionally P-(cyan dots) and S-wave (black dots) velocities calculated from components of the elastic tensor are shown (Equation 2.12). The solid blue line represents velocity values derived from the XCT densities by the formula postulated by Kohnen (1972) (thick blue line) and Diez et al. (2013) (thin blue

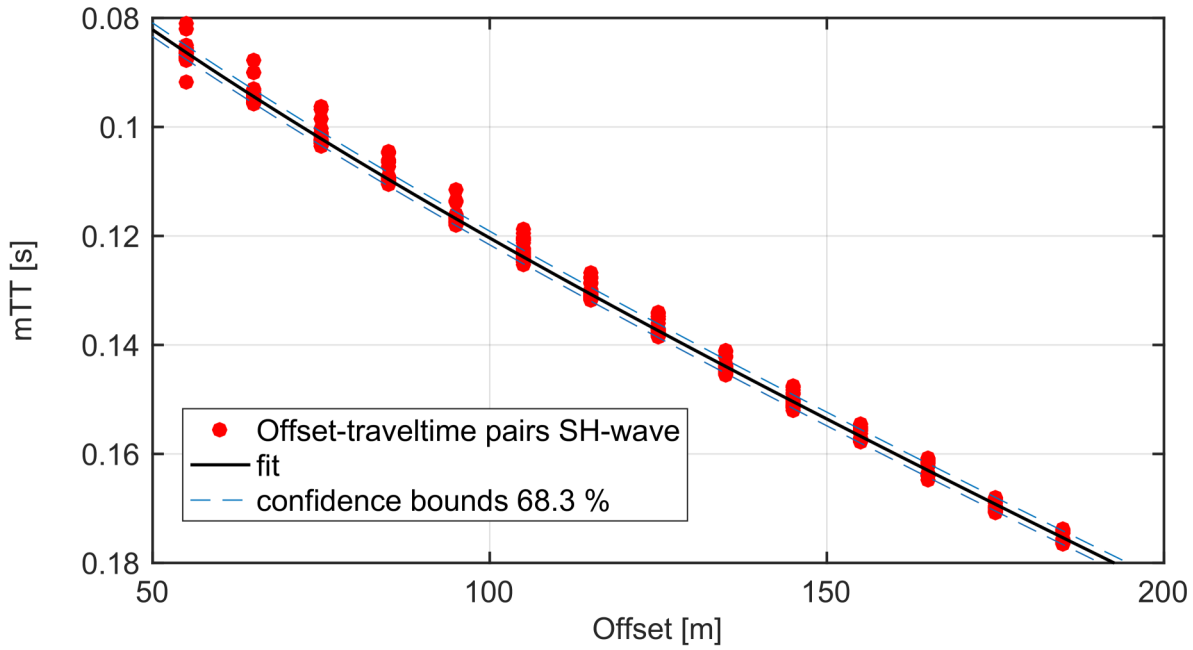

Figure 5.16.: Fit of the SH-wave data of the parallel profile. Black line show the fit of the data (red dots). Blue dashed line represent the fit with 68.3 % confidence bonds.

line). Data derived from diving-wave inversion shows a constant increase in S-wave velocities from 1250 m s^{-1} in 10 m depth to 1700 m s^{-1} in 77 m depth. The P-wave velocity increases from 2000 m s^{-1} in 10 m depth to 3400 m s^{-1} in 77 m depth. Difference in SH- and SV-wave velocities can be observed with a maximum of 140 m s^{-1} at a depth of 4.5 m and a difference of 41 m s^{-1} at a depth of 40 m. These differences are within the range of uncertainties. The S-wave velocity from diving-wave inversion (red and yellow line) seems to fit the S-wave velocity derived by the density-velocity relation (thin blue line), as well as with the velocity from FEA (black dots). P-wave velocities derived by Kohnen's formula (thick blue line) and the diving-wave inversion (green line) differ, especially in shallower areas. In contrast the velocities from diving-wave inversion (green line) and velocities from the FEA (cyan dots) are in good agreement for depth larger 30 m. The velocities above 30 m differ, considering the uncertainty range, for the P wave with 250 m s^{-1}.

The calculated elastic moduli from the FEA and diving-wave inversion SV-velocities with XCT densities are shown in Figure 5.18, again the coloured area in the background shows the uncertainty. Likewise, moduli calculated from SH-wave velocities and XCT densities are shown in Figure 5.19. The comparison of these two plots shows some deviations above 30 m. Again the uncertainty range of the SH-wave moduli is smaller when compared to the SV-wave moduli. The shear modulus calculated from XCT densities and diving-wave inversion increases from 0.66 GPa in 10 m depth until 2.35 GPa in 77 m depth. Values below 10 m depth derived from the FEA plot within the uncertainty range for the SV-wave shear modulus. The shear modulus in 10 m depth, derived from the FEA, differs by 1.1 GPa from the value derived by diving-wave inversion.

The bulk modulus calculated from XCT densities and diving-wave inversion increases from 1.117 GPa in 10 m depth to 5.8 GPa in 77 m depth. The values of the bulk modulus in 10–70 m depth fit with diving wave inversion results. The bulk modulus derived by the calculation with the elastic tensor c_{11} in 10 m depth does not plot within the uncertainty and differs by 0.427 GPa. The assumption of an isotropic medium would require that the elastic tensor c_{11} equals c_{33}. A difference in bulk moduli derived from the elastic tensor c_{33} and c_{11} can be seen

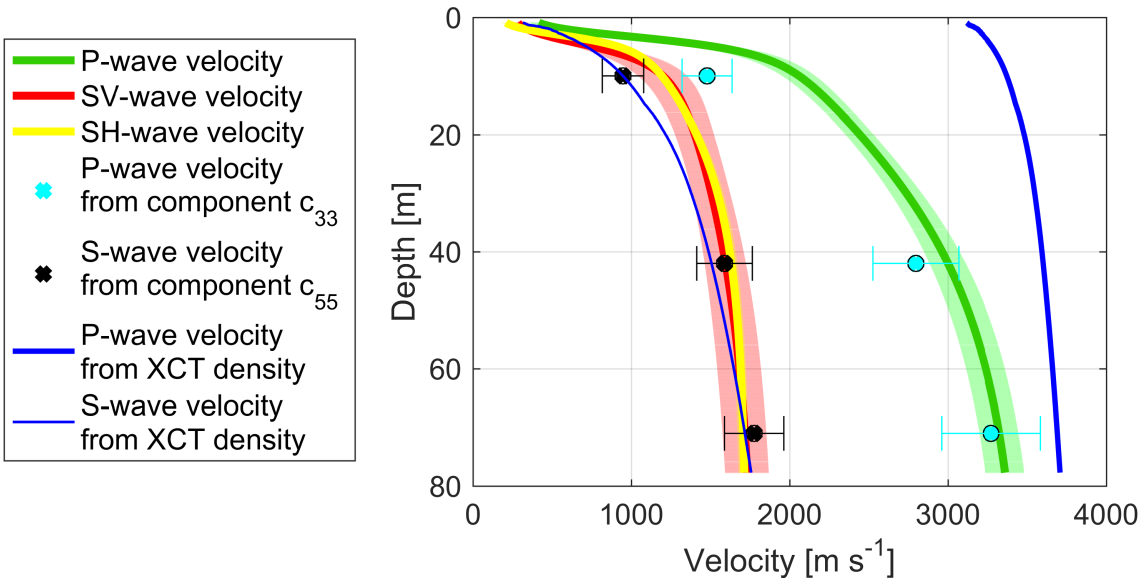

Figure 5.17.: Velocity-depth profile from the parallel profile. The red and yellow line show the SV- and SH-wave velocity with depth. The green line shows the P-wave velocity. Blue lines are velocities derived by XCT densities. Black and blue crosses are velocity values calculated from components of the elastic tensor (FEA). Coloured area in the background displays the range of uncertainty of the diving wave velocities. Error bars display the uncertainty range of FEA values.

for all values. The bulk modulus derived from the SH-wave velocity and the algorithm show similar results (Figure 5.19).

Values of the poisson's ratio are compared in Figure 5.20. The values derived from the algorithm lie within the uncertainty of the poisson's ratio calculated with SV-wave velocities. The uncertainty of the SH-wave is again smaller compared to the SV wave. Here the values of the algorithm do not plot in the uncertainty range for all depth. The comparison of poisson's ratio derived from SH- and SV-wave velocities show a striking difference of values in the upper 18 m. Below that depth both graphs show a increase in ratio from 0.24 to 0.319. The values derived from the algorithm show an increase from 0.15 in 10 m depth to 0.29 in 70 m depth.

Lateral velocity variations can be seen in velocities derived from diving waves (Figure 5.21 (B)). Figure 5.21 (A) shows a schematic drawing of the parallel profile with markers at three locations. The ray path below the locations show examples for the path of the diving wave, with the deepest point of the diving wave located below the locations. The P-wave velocity profile in the west (location 303) shows higher velocities, than in the east (location 112), with a maximal difference of 400 m s^{-1} at a depth of 70 m. The difference between P-wave velocities at location 267 and 122 is 100 m s^{-1} for a depth of 70 m. The differences for the SH-wave are similar to the differences of the P-wave. The SV-wave velocities show slightly higher differences of 120 m s^{-1} at a depth of 70 m between 122 and 276 and 100 m s^{-1} at a depth of 70 m. In shallower areas the S-wave velocity seems to be decreasing from east to west, while the O-wave velocity remains almost the same. The velocities derived by the algorithm represent the velocity at the location of the shallow ice core B34, and represents thus, a reference value.

Lateral variations in velocity also influence the elastic moduli. The moduli shown in Figure 5.22 are calculated from velocities at the three locations mentioned above and the XCT densities. A general increase in elastic moduli can be observed from east to west. The variation lies within the uncertainty range of the values derived by the algorithm for location 112 and 267. The bulk moduli at location 303 in a depth of 70 m diverge from the algorithm values.

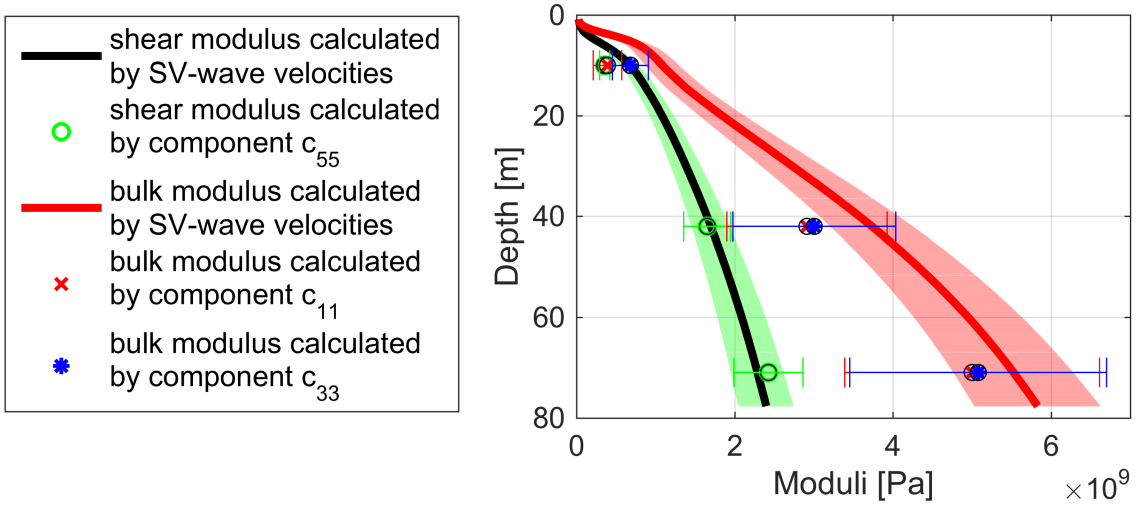

Figure 5.18.: Bulk (red line) and shear modulus (black line) derived from diving-wave inversion and the XCT densities. Green circles show the shear modulus from the algorithm. Red dots represent the bulk modulus derived from the elastic tensor c_{33}, red crosses the bulk modulus derived from the elastic tensor c_{11}. Coloured area in the background displays the range of uncertainty of the diving wave velocities. Error bars display the uncertainty range of FEA values.

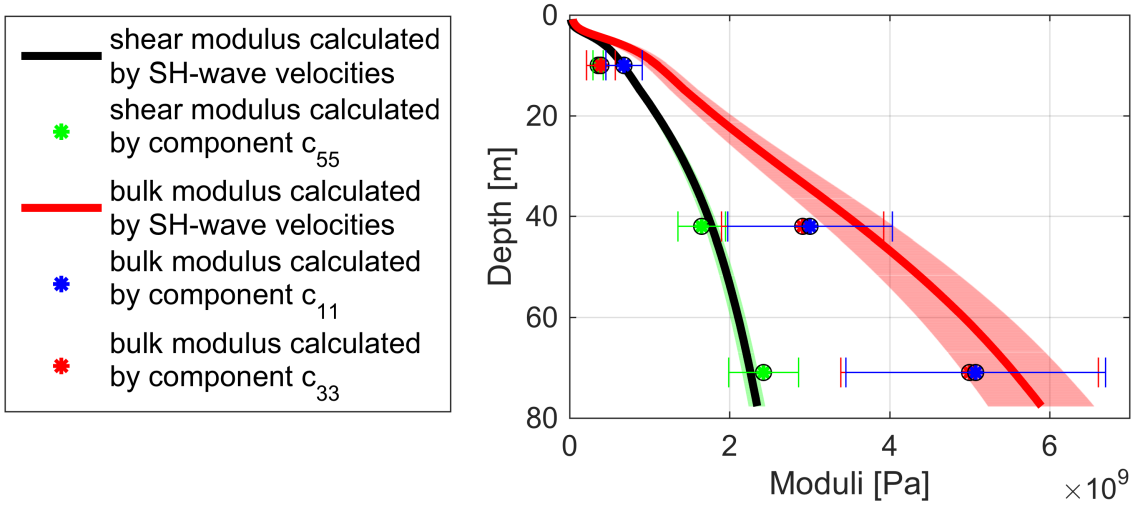

Figure 5.19.: Bulk (red line) and shear modulus (black line) derived from diving-wave inversion and the XCT densities. Green circles show the shear modulus from the algorithm. Red dots represent the bulk modulus derived from the elastic tensor c_{33}, red crosses the bulk modulus derived from the elastic tensor c_{11}. Coloured area in the background displays the range of uncertainty of the diving wave velocities. Error bars display the uncertainty range of FEA values.

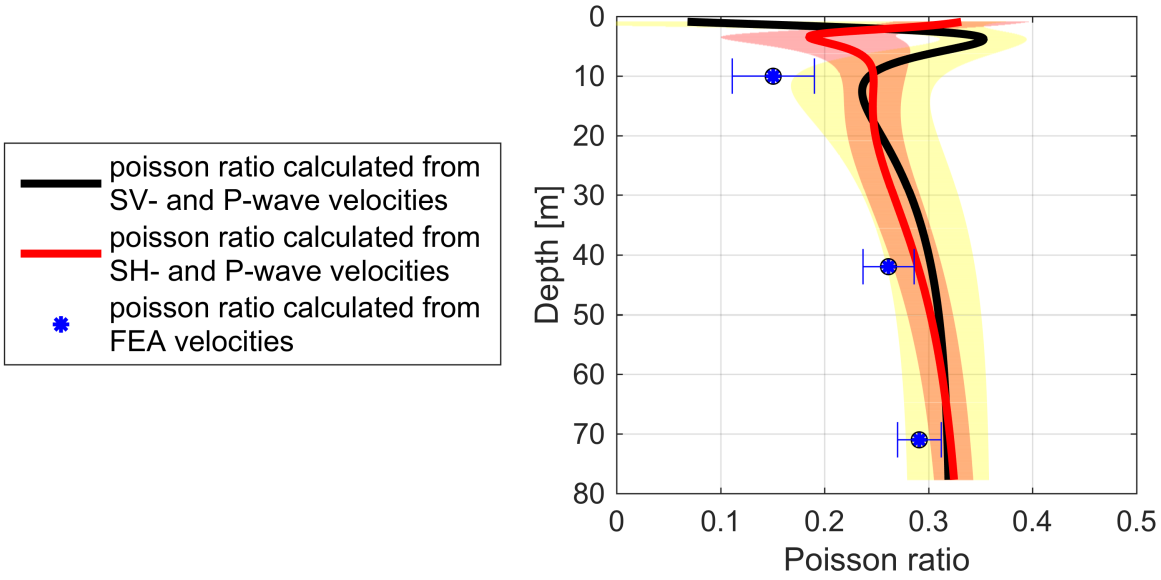

Figure 5.20.: Comparison of poisson's ratio derived from SH- and P-wave data (red line) and SV- and P-wave data (black line). Blue crosses display values calculated from the moduli derived by the FEA and the XCT densities. Coloured area in the background displays the range of uncertainty of the diving wave velocities. Error bars display the uncertainty range of FEA values.

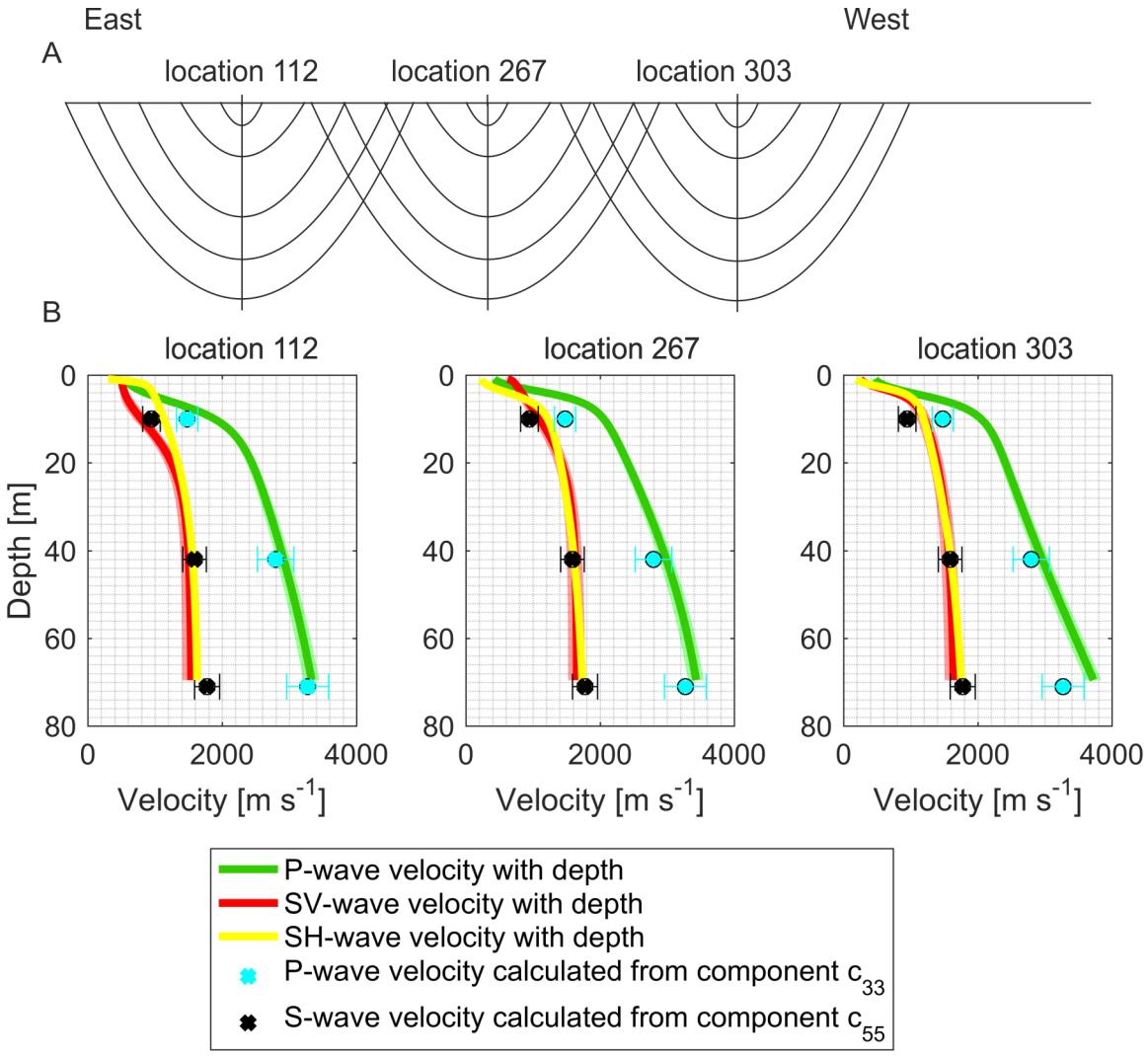

Figure 5.21.: Comparison of P-,SV- and SH- wave velocities at different locations. Blue and black crosses with the corresponding error bars represent the velocities derived from the algorithm. Coloured area in the background displays the range of uncertainty of the diving wave velocities. Error bars display the uncertainty range of FEA values.

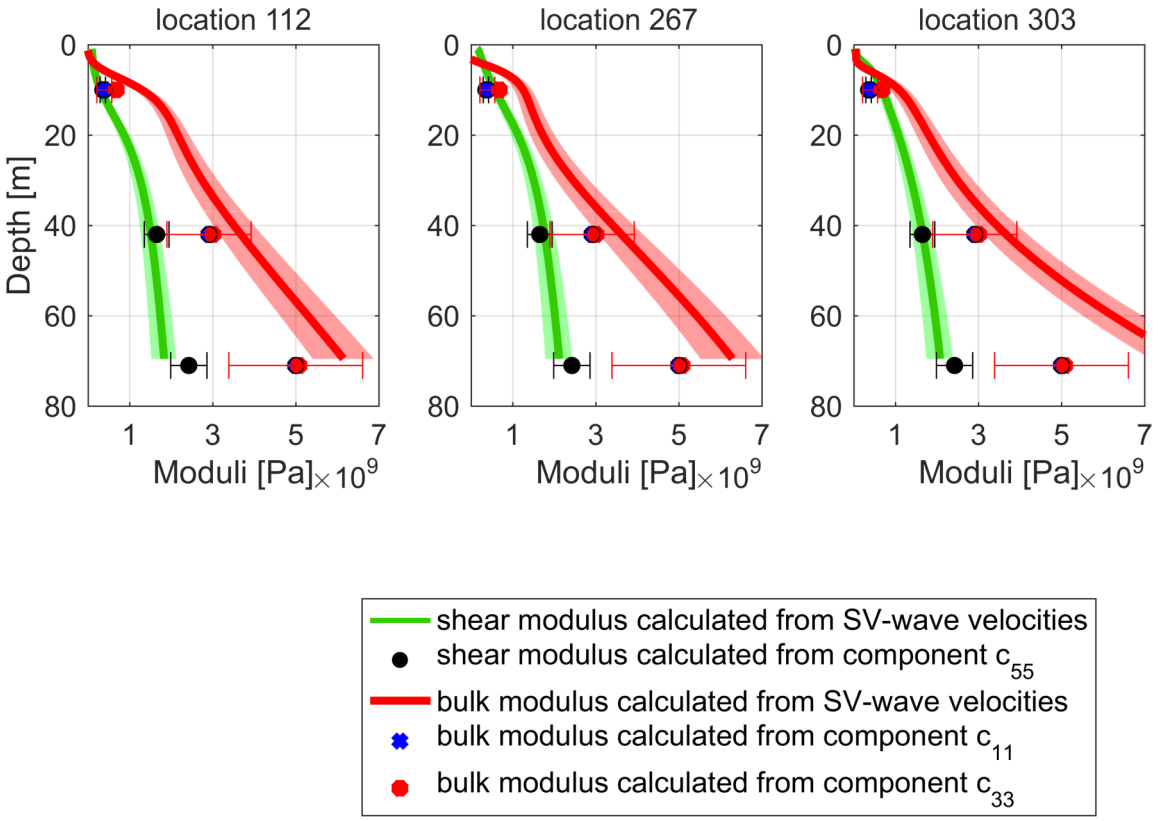

Figure 5.22.: Comparison of elastic moduli derived from SV- and P-wave data and the XCT densities at different locations. Red and green dots represent elastic moduli derived by the algorithm. Coloured area in the background displays the range of uncertainty of the diving wave velocities. Error bars display the uncertainty range of FEA values.

6. Interpretation

In the following I will discuss reasons for the presented results of processing. In addition the origin of the high amplitude signals seen in the shallow and deeper parts of the stacks are investigated and discussed. Furthermore, the velocity profile and elastic moduli derived from diving-wave inversion are evaluated by means of an error analysis. Moreover, the assumption of firn as an isotropic medium is analyzed. This chapter concludes with a joint interpretation of reflection seismics and diving-wave data.

6.1. Detection and evaluation of reflections

Circumstances such as the constant velocity increase with depth and the dominant groundroll made the processing of these data challenging. The surface wave velocity depends on frequency due to wave dispersion. The observed bending of the groundroll could be a possible reason for the partial failure of the K-L transformation. Potential reflections are not separated from noise in the f-k domain (Figure 4.7), probably because they contain only low amplitudes compared to the groundroll in the f-k spectrum.

Hofstede et al. (2013) reported that englacial reflections recorded during explosive measurements at Halvfarryggen mostly contain frequencies above 100 Hz. Therefore, the corresponding vibroseis source passband from 100-240 Hz is likely to visualize englacial reflections. The fact that the lowpass filter applied on the data from Kohnen Station could not suppress the groundroll, highlights the occurrence of groundroll over the whole frequency band.

The hyperbolic noise, seen in the first five shots in the perpendicular profile (Figure 5.6) is not caused by reflections of seismic signals, because the hyperbola apex is not located within the data. This noise could be caused by electromagnetic radiation of the automatic weather station constructed by University Utrecht or by Pistenbullys driving near Kohnen Station.

The observed polarity reverse for the first 30 shots of the P-wave was probably caused by turing the polarity switch at ElViS during data acquisition.

Due to the (on average) continuous density increase in firn (Figure 3.4) it is doubtful that a sufficient impedance contrast is given to cause reflections within the firn. An ice layer of several centimeters thickness could cause a significant impedance contrast. The annual mean temperature at Kohnen Station is below 0°C. Therefore the occurrence of ice layers in the firn column can be ruled out. Small-scale variations seen in the XCT densities with depth are therefore not caused by ice lenses. When I applied a smoothing function, containing a window size comparable to the vertical seismic resolution, to the measured XCT density (ice core B40), small scale variations disappeared and a continuous density increase can be seen. A sufficient impedance contrast can therefore not be caused by density variations. This leads to the assumption, that a possible impedance contrast is probably caused by a change in elastic moduli. The velocity and thus elastic-moduli determination via diving-wave inversion will be discussed later in this chapter.

Shallow high amplitude signals in the stacked parallel profile

According to Druivenga et al. (2005) the penetration depth of the ElViS is limited to 150 m, which corresponds to a TWT of 0.114 s (calculated from velocities derived from the ice-core

densities). On the other hand Polom et al. (2014) showed that the penetration depth in firn and ice is expected to be deeper due to the fairly small damping of seismic waves in ice. The deepest features are estimated to be in 150 m depth for the SH waves and 220 m for the P waves (Polom et al., 2014). Although this depth is only a rough estimate and depends on the material properties, it emphasizes the limitations of this system.

The high amplitude periodic signals in the stack of the parallel profile can be seen when stacking all offsets, but the signal gets stronger if only near offsets are stacked. These signals appear at similar mTT for P and S waves. The periodic event might be interpreted as the multiple of an initial reflection. A multiple is characterized by an event that has undergone more than one reflection, but containing a significantly lower amplitude compared to the reflection. In general multiples visible in the stack should also be visible as a hyperbola in the shot gather, respectively CDP gather. Reflection amplitudes, and thus also multiple amplitudes, decay proportional to the square reciprocal of the travel distance. Apart from the fact that no primary reflection can be detected, multiples should show a significantly damped amplitude with increasing mTT, which cannot be observed in this data. The periodic signal cannot be seen in the median stack, which highlights the occurrence of a few high amplitude signals instead of high amplitude signals in every trace.

I interpret the periodic high amplitude signal (Figure 5.9 and 5.11) as caused by a Rayleigh wave. All characteristics such as dispersion and amplitude decay (Shearer, 2009) can be seen in all three components.

I approximated the Rayleigh-wave velocity by fitting a tangent. This results in a velocity range of 210–220 $\mathrm{m\,s^{-1}}$ (for shots in the west). This value is just an approximation because the first breaks of the Rayleigh wave are not clearly visible. The Rayleigh-wave velocity can also be calculated by means of the P- and S-wave velocities (Equation A.3 in the Appendix). Therefore, velocities derived by diving-wave inversion are used, resulting in a Rayleigh wave velocity of 200–250 $\mathrm{m\,s^{-1}}$ for the upper meters of the firn. The two independently derived velocities are in good agreement. The observed inconsistency of the Rayleigh-wave velocities (Figure 5.12) along the profile indicates lateral inhomogeneities and results in a trough flank shape of the high amplitude signals.

The Rayleigh-wave signal can be seen in offsets smaller than 105 m and thus down to a mTT of 0.4 s (Figure 5.9 (B)). The first 30 shots mainly contain far offset traces, that is why only a part of the Rayleigh-wave signal is observed in these shots. This explains why the stack did not change significantly after the polarity reverse of the first 30 shots, since only a few amplitudes of the Rayleigh wave are affected by the polarity reverse. Another argument for the Rayleigh wave is the depth difference seen for the high amplitude signals after depth conversion of the P- and S-wave data. Reflections and multiples of the same reflector would be visible in the same depth for both wave types. S-wave shots were always taken twice, with alternating polarity to be able to cancel out the P-wave in the S-wave data during processing. Therefore the signal in the S-wave data does not show P-wave reflections or multiples and must be a wave that can be recorded by vertical and horizontal movement.

High amplitude signals at 1.63 s mTT

In the following only the high amplitude signal in the P wave of the parallel profile is considered, because the signal in the perpendicular profile is not as clear as in the parallel profile. The high amplitude signal at 1.63 s mTT was first interpreted as the reflection of the bedrock. Since this signal can only be seen in traces with an offset smaller than 30 m, no hyperbolic moveout, which would indicate a reflection, could be observed. Diez et al. (2015) performed an explosive and vibrator seismic study at Kohnen in 2013 to determine a velocity model for the ice column. Their wide-angle seismic profile covers inter alia the same area as the parallel

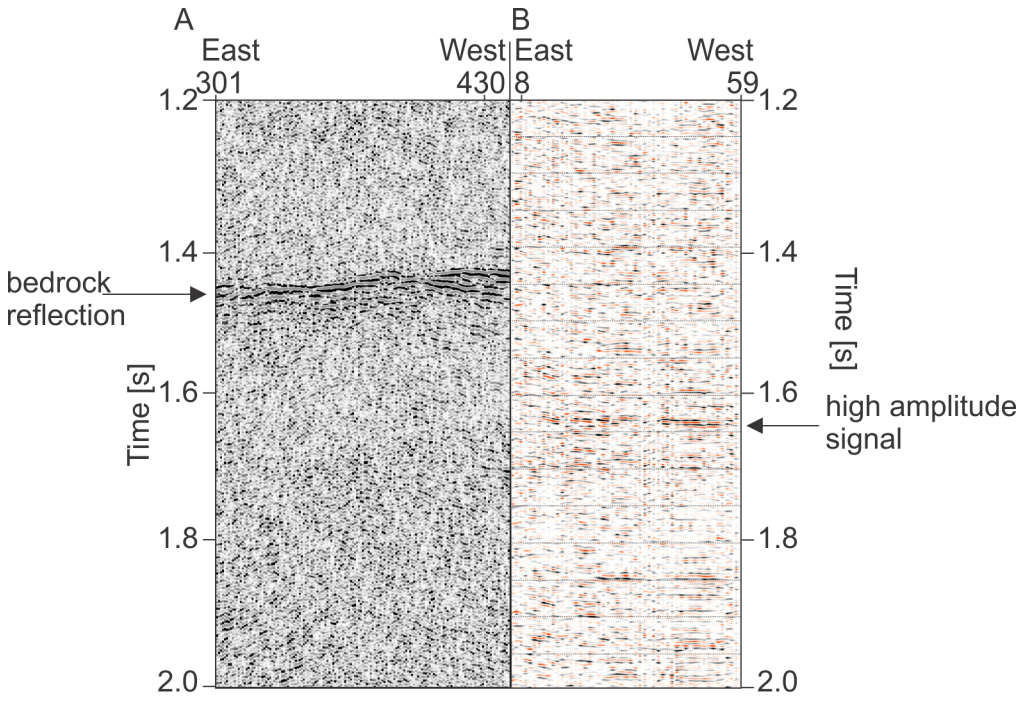

Figure 6.1.: A) Stack of wide-angle data from the survey in 2013. B) Stack of vibroseis P-wave data from the survey in 2011/12. Arrows mark the bed reflection in the 2013 data and the high amplitude event in the 2011/12 data. A) and B) cover approximately the same area.

profile in this study of 2011/12. The bedrock reflection in the wide-angle data is visible at 1.44 s TWT for P-wave data (Figure 6.1), which corresponds to a depth of 2700 m according to data shown by Diez et al. (2015). This depth is consistent with ice-core results and radar measurements in this area. Therefore, the bed reflection can be assumed to be at 1.44 s TWT.

Two different possibilities exist explaining the event seen at 1.63 s mTT in the 2011/12 data. First, the high amplitude signal in 2011/12 also shows the bed reflection. And the traveltime differences are caused by inaccuracies of the different recording systems. Second, the high amplitude signal is not caused by the bedrock reflection but by a reflection at surrounding objects.

Regarding the first possible reason, a traveltime difference between the 2011/12 and 2013 events could be caused by a triggering error. The triggering accuracy for the Geode used in 2011/12 is denoted as 1/32 of the sample interval (7.81 mus for a stacking interval of 0.25 ms) by the manufacturer Geometrics. No triggering accuracy was denoted for the StrataView, the seismic recorder used in 2013 with a sampling interval of 0.25 ms. With respect to the denoted triggering accuracy for the Geode a time difference of 0.15 s would result in a triggering inaccuracy of 9.21 % and thus an actual stacking interval of 0.226 ms for the StrataView. This inaccuracy of the two different recording systems would also affect the arrival times for other signals such as diving waves. The diving wave first breaks of the 2013 data fit the 2011/2012 data with a negligible deviation of 0.7 % (Figure 6.2).

Considering these observations I assume the traveltime difference between the two datasets is not caused by a triggering error and the high amplitude signal does not show the bed reflection. Additionally, the assessment of the penetration depth of the ElViS contradicts

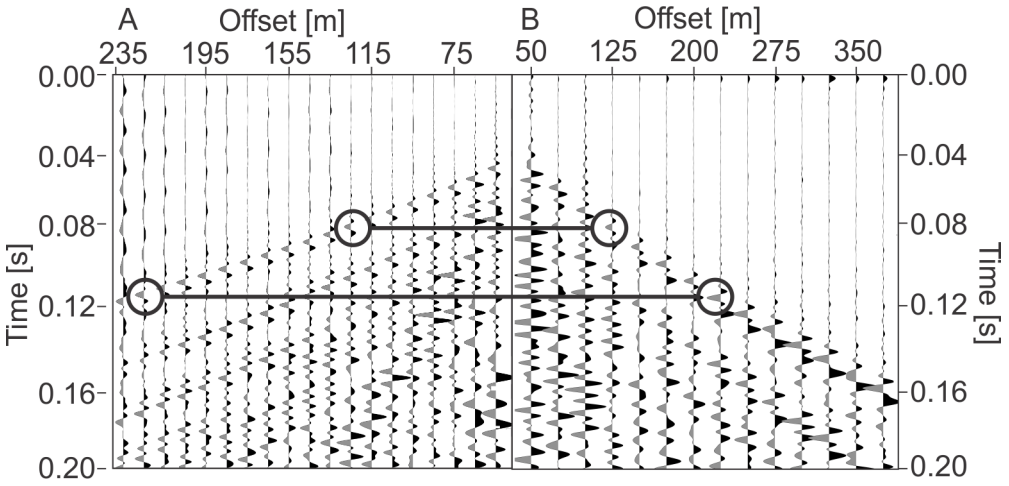

Figure 6.2.: Comparison of diving wave first breaks in the A) wide-angle data in 2013 and the B) vibroseis data in 2011/12. Lines and circles connect diving wave first breaks observed in 2013 and 2011/12 at the same offset

against a signal of the bed reflection. Therefore, possible reflection objects apart from the bedrock are under investigation in the following.

Potential sources for the 1.63 s event are, despite artefacts, reflections of different wave types at surrounding objects. Wave types that could be reflected at objects are sound, Rayleigh, or Love waves. Here I will focus on the analysis of the dominant waveforms in this data: Rayleigh and sound waves.

The high amplitude signal at 1.63 s mTT appears horizontally in the central part of the stack (Figure 5.13) and should thus be caused by an object that is located parallel to the profile. Towards the east of the profile an upward dip of the high amplitude signal can be seen, although the signal of the dip looks scattered. For the calculation of travel distances the TWT as well as the corresponding velocity is taken into account.

The temperature at Kohnen station ranges between -20°C and -45°C during the austral summer (December-February) which results in a sound speed range between 302.5–318.6 m s^{-1}, and thus, a radius of 240–255 m (purple ellipsoid in Figure 6.3). The already calculated Rayleigh-wave velocity (Chapter 5.1.2) of 208–230 m s^{-1} resulted in a radius of 170–180 m (black ellipsoid in Figure 6.3).

Figure 6.3 shows a satellite image of Kohnen Station and the surrounding area in December 2013. The Kohnen Station, the trench and cargo containers are shown in this map, as well as the location of the parallel (blue line) and perpendicular (red line) profile. The envelope of travel distance for the sound wave, calculated for CDP gather 8–59 with a lateral constant velocity are displayed by the purple, for the Rayleigh wave by the black dashed ellipsoid. Both calculated distances with constant velocities do not match with an object for both, the end and the beginning of the CDP line of the parallel profile.

On the one hand, potential reasons for this could be a slightly different position of the containers or the profiles and, on the other hand, some error in the velocity used for the calculation and lateral inhomogeneities. The first potential reason is a lack of accurate GPS positions for the cargo containers and profiles. Additionally, the exact orientation of Kohnen Station and the trench was adjusted by a satellite image. Only two positions, between which the profile is located, were determined from a GPS measurement. The second reason are the velocities used for the calculation of distances. Velocities used for the calculation of the distance did not include dispersion or lateral variations. Therefore, the Rayleigh waves were

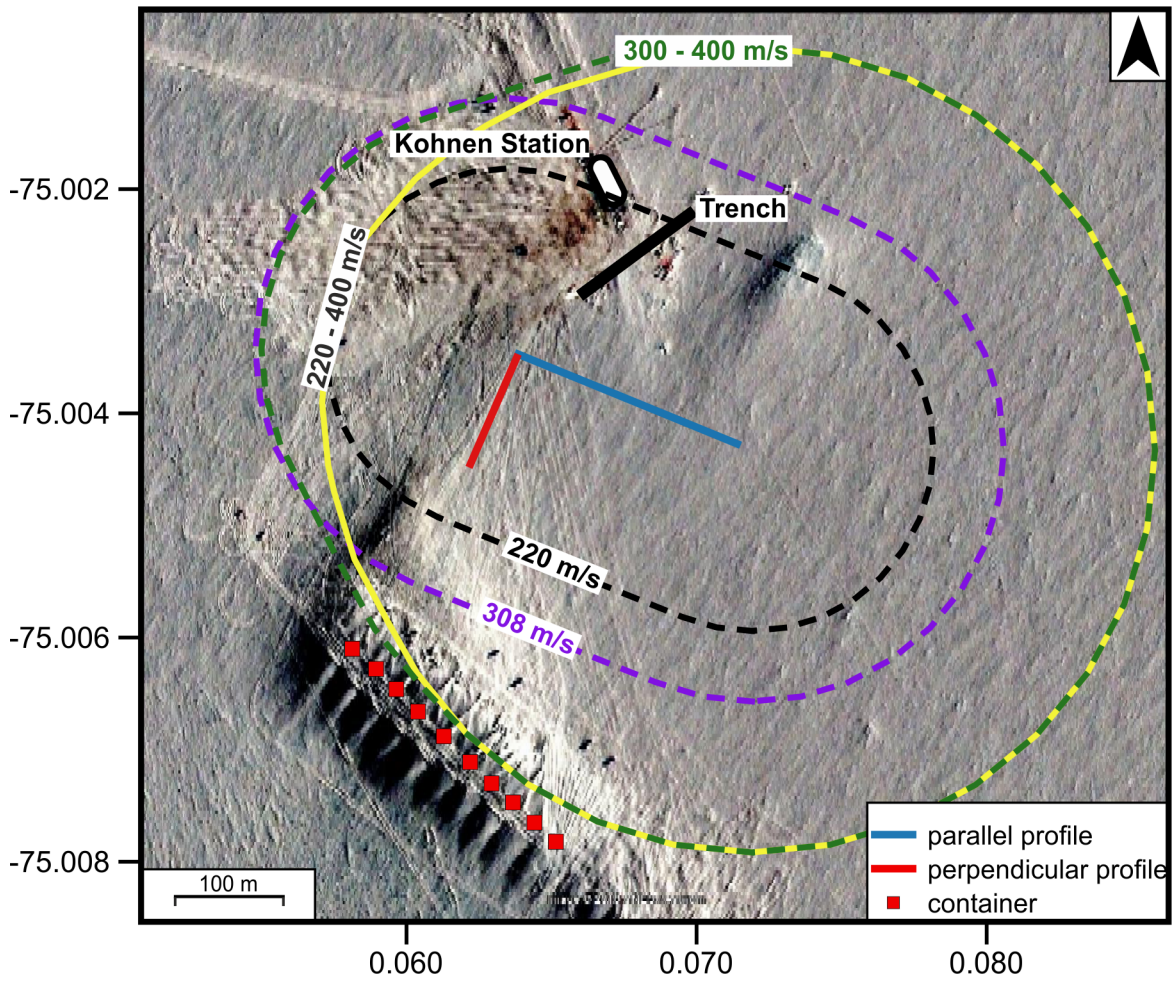

Figure 6.3.: Satellite image of Kohnen Station in December 2013. Possible objects on which sound (purple ellipsoid) or Rayleigh waves (black ellipsoid) could be reflected at, causing the high amplitude signal at 1.63 s mTT, seen in Figure 5.13. An interpretation of the Rayleigh-wave spread under consideration of the lateral inhomogeneities observed before is displayed by the yellow dashed ellipsoid. The green dashed ellipsoid displays the Rayleigh-wave spread including lateral variations in Rayleigh-wave velocity but under the assumption of a deeper penetration depth and thus higher velocity in the west (Satellite image: Google, (NESI/Astrium)).

assumed to travel with a constant velocity within the first meters of the firn. However, the constant velocity increase with depth could lead to a greater penetration depth and thus higher velocity of the Rayleigh wave.

Since distances calculated for lateral homogenous velocities did not fit with any objects in Figure 6.3, I investigated the possibility of lateral inhomogeneities influencing the velocity. Lateral variations in sound speed can be ruled out. The similarity of the shape of the high amplitude signal in 1.63 s mTT to the shallow high amplitude signals seen in the upper part of the stack (Figure 5.9) is conspicuous. I interpret the shallow high amplitude signal to be caused by the Rayleigh wave that has experienced lateral inhomogeneities. A Rayleigh wave causing the high amplitude signal at 1.63 s mTT is also influenced by lateral inhomogeneities, which results in the upwards dip of the high amplitude signal towards the east. Therefore, I calculated the travel distances of a Rayleigh wave with increasing velocity towards the east. The lateral difference in Rayleigh-wave velocity was denoted as 260–490 m s^{-1} (west to east) before. The envelope of these travel distances did fit with the containers in the eastern part of the profile (yellow dashed ellipsoid). The dashed green ellipsoid shows the travel distances

of the Rayleigh wave under the assumption of a velocity increase of 300–490 m s^{-1} (west to east). For this velocity range the travel distance reaches the location of the containers and could therefore be reflected there, subsequently received by the geophones. A Rayleigh wave containing a higher wavelength would penetrate into deeper layers. Due to the density, and thus, velocity gradient in firn these Rayleigh waves could travel with a faster velocity, compared to waves with higher frequency content. This frequency content for the high amplitude event can be seen in Figure 5.13 (B)), the Rayleigh-wave frequency content in the shallow part can be seen in Figure 5.12 (B). The signal in 1.63 s depth contains generally higher frequencies. Therefore, the Rayleigh wave causing the high amplitude signal in 1.63 s mTT penetrates deeper into the firn, and thus, is less influenced by lateral inhomogeneities caused by layering.

At this point I cannot clearly identify the origin of the signal observed within the stacked data of the parallel profile at about 1.63 s mTT. The Rayleigh wave causing this signal under the assumption of lateral inhomogeneities comprises a high uncertainty. The Rayleigh wave being the origin of the observed signal at 1.63 s mTT cannot be refuted without further investigation.

6.2. Diving wave analysis

The differences between SV-wave mTT and SH-wave mTT (Figure 5.15), and thus higher velocity, could indicate anisotropy. The SH-wave particle motion oscillates purely in the horizontal plane, while the SV wave induces an up- and downward particle oscillation in the vertical plane, i.e., perpendicular to the SH wave (Bormann, 2002). The particle velocity in radial direction is faster than in tangential direction ($V_{SV} > V_{SH}$), which is referred to as S-wave splitting (Bale et al., 2009). In an isotropic medium these waves are supposed to travel with the same velocity and should thus comprise the same offset-traveltime pairs. The difference between mTT of the perpendicular P-wave data and the parallel P-wave data could indicate a non-horizontal topography. The topography at Kohnen station shows an increase in elevation around objects like containers or Kohnen station itself. This snow accumulation, also seen in the satellite image in Figure 6.3 is caused by wind-induced snow drift. The perpendicular profile was taken towards the containers and the elevation increased with offset to the parallel profile. This change of geometry could be a reason for the enhanced scattering of mTT of the P-wave data of the perpendicular profile.

The comparison of XCT densities and the conversion of P-wave velocities into density by Kohnen's formula showed a bad fit and highlights the need for an advancement of this relation like aspired by Kiya Riverman, PhD student working with Penn State Ice and Climate Exploration (Kiya Riverman, pers. comm.). In contrast the relation postulated by Diez et al. (2013) showed a good fit for the converted S-wave velocities and the XCT densities.

Traveltimes were only picked for offsets larger than 15 m. Velocities calculated from diving waves for depths less than 10 m should not be considered, since these values are not based on measurements but on the fitted curve. Small variations like seen for the SH- and SV-wave velocities (Figure 5.17) can result in strong deviations of the elastic moduli, like seen in the poisson's ratio (Figure 5.20). The fit of the exponential curves (Equation 4.5) to the SH-wave data did converge, which also resulted in a smaller uncertainty range, when compared to the SV-wave uncertainty. The lateral variability seen in the S and P wave data between location 112 and 302 indicate lateral inhomogeneity. The difference in 70 m depth observed for location 267 and 303 is probably caused by an insufficient fit of the exponential curve (Equation 4.5). Pathways of diving waves at location 303 and 267 should cross each other with depth (Figure 5.21 (A)). A significant increase in velocity with depth, like seen for location 303 should, thus, also be seen in the velocity profile at location 267. The lateral variability of velocities along the profile is striking with the observations made for the variability of

Rayleigh-wave velocities. For the P waves an increase in velocity towards the west and for the surface waves an increase in velocity towards the east were observed. The Rayleigh-wave velocity is mostly influenced by the S-wave velocity. The S-wave velocity varied less laterally, when compared to the P-wave velocity below 40 m. A higher variation in S-wave velocity can be observed for the upper 30 m of the firn, where the S-wave velocity decreases towards the west, and thus, indicated for a Rayleigh-wave velocity increase towards the west. But values above 10 m, and at location 303 and 112 above approximately 20 m are not based on mTT picked for the diving waves but on the values derived from the exponential curve. Therefore, I only interpreted the trend of the velocity.

Accuracy of an isotropic medium

The elastic moduli were calculated under the assumption of an isotropic medium. In case of isotropy, the component (derived from the FEA) c_{33} would equal c_{11} as well as the component c_{12} would equal c_{13} of the elastic tensor. This is not the case and highlights the inaccuracy of the assumption of an isotropic medium. Therefore, the anisotropy of firn is investigated and interpreted in the following. Under the assumption of isotropy the components c_{33} respectively c_{11} and c_{44} respectively c_{55} can be calculated from seismic velocities and the XCT densities (Equation 2.7). The components derived from diving wave velocities and the XCT densities are shown together with components derived by the FEA in Figure 6.4. The yellow and red dots show the elastic tensor c_{44} respectively c_{55} derived from S-wave velocities, and the green dots the component c_{11} respectively c_{33} derived from P-wave velocities. The differences in components derived under the assumption of an isotropic and TI medium is within the uncertainty range for depth between 40–77 m. The difference between components at a depth of 10 m indicates anisotropy. To further investigate the anisotropy with depth, Thomsen parameters (Equation 2.13) are calculated from components of the elastic tensor derived from the FEA (Figure 6.5).

Values for the Thomsen parameter smaller than 0.01, like seen for depth larger than 40 m are referred as to weak anisotropy, whereas values in depth in the range 10–40 m are higher than 0.01 and indicate an anisotropic medium (Tsvankin, 1997; Yilmaz, 2001). This is in good agreement with the observations made by comparing the isotropic tensors derived from velocities and the TI tensors from the FEA (Figure 6.5). It has to be kept in mind that only three point measurements down to a depth of 70 m are available (Figure 6.5). Thomsen parameters derived for a depth of 10 m could be influenced by an artefact in the 3D XCT measurement or the FEA. Ice lenses in the firn could lead to an artefact, but this can be ruled out at Kohnen Station, due to the annual temperature below zero. Additionally, an erroneous measurement of the 3D XCT should also be visible within the density data derived from the 3D XCT, which cannot be seen for this depth. Another explanation for this high value could be stratigraphic noise in the upper meters of the firn. This would mean that the horizontal alignment, and thus, smoothing of the fluctuations of the accumulation and coarse layers develops with depth (Münch et al., 2015). Another option would be the so called backus average for anisotropic layering. Due to that thin layers, like annual layers (smaller thickness than the seismic wavelength) with different densities influence the recorded seismic signal (Gelinsky and Shapiro, 1997). The observed anisotropy at 10 m depth is possibly not caused by crystal orientation but layering. Furthermore, the method of the FEA in combination with 3D XCT images is new and reliability of the results for firn with a very low density not yet well known.

The deviations observed between the different components indicate an anisotropic medium. Under the assumption of a VTI medium especially c_{11} and c_{33} are influenced and describe together with the density the horizontal and vertical P-wave velocity. Diez et al. (2015)

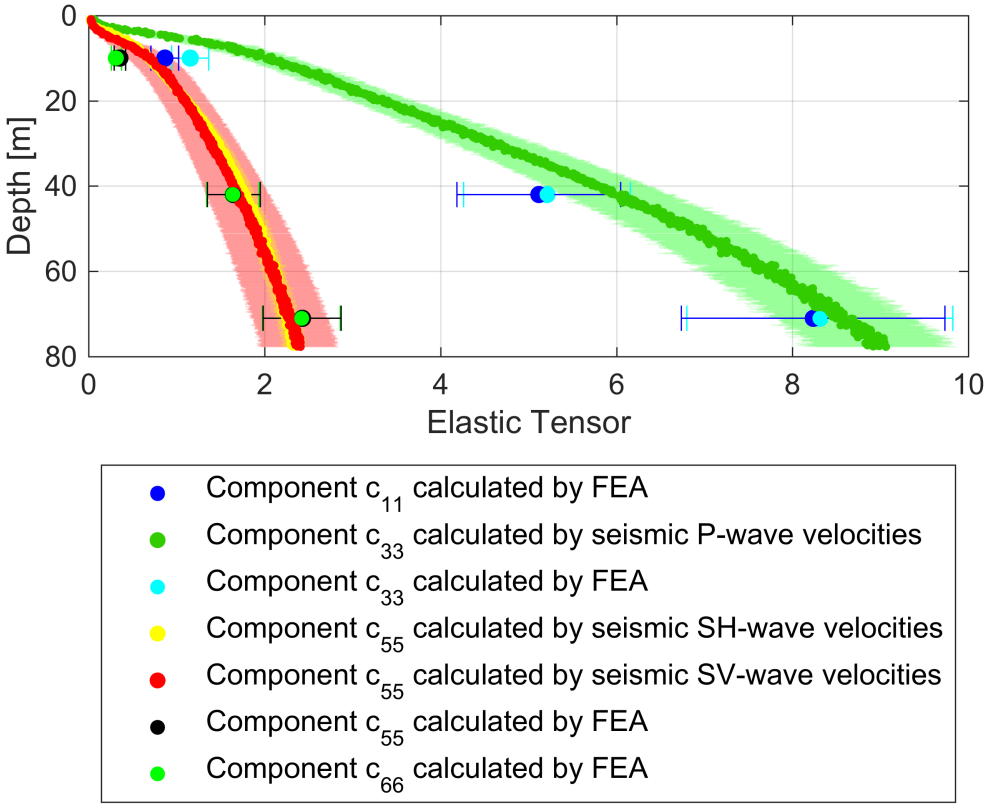

Figure 6.4.: Calculated elastic tensors from P-(green dots), SH-(yellow dots) and SV-wave (red dots) velocities. Dots with corresponding error bars represent the tensors derived from the FEA. Coloured area in the background displays the range of uncertainty of the diving wave velocities. Error bars display the uncertainty range of FEA values.

calculated COF distributions for the EDML ice core for depths larger 50 m. The COF does not show abrupt changes in depths between 50–100 m.

6.3. Joint interpretation of reflection seismics and diving wave inversion

So far, neither abrupt changes in density nor in elastic moduli could be detected. Calculations of COF and the elastic tensor indicate weak anisotropy at a depth of 10 m, but no abrupt changes as well. The impedance contrast resulting from these changes is insufficient to generate strong reflections or generates weak reflections which are superimposed by groundroll. Reflections within the firn would be recorded at TWT less than 0.1 s and would therefore be plotted in the area of diving wave first breaks and the high amplitude groundroll. Furthermore, an impedance contrast causing an englacial reflection in seismics should in most cases also be visible in data of other geophysical methods (like radar). Diez et al. (2015) investigated englacial reflections recorded during the wide-angle measurement at Kohnen Station in 2013. The reflections under investigation are located below the FIT and are interpreted as caused by changes in COF.

Phase-sensitive radar (pRES) data were acquired in 2015 and 2016 at Kohnen Station. The

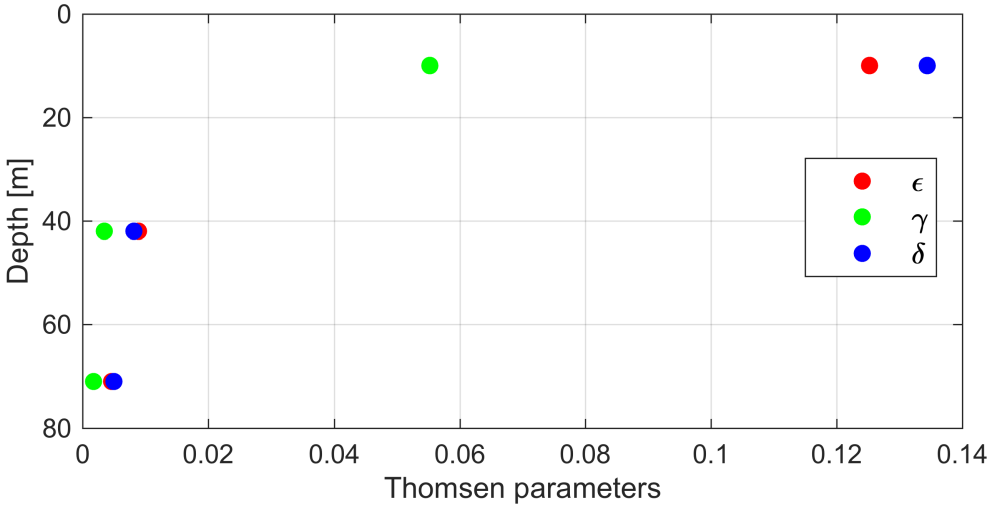

Figure 6.5.: Calculated Thomsen parameter from components of the elastic tensor derived from the FEA.

propagation of radar waves is mainly influenced by the density, COF, conductivity and the temperature. A visible reflection within the firn in radar data could therefore give evidence for an abrupt change in density (Diez et al., 2015). The backscatter with depth indicates a decrease in backscatter energy after an approximate depth of 90 m, which corresponds to the FIT. Energy spikes in the backscatter, which indicate reflections, can be seen for the whole depth. pRES data from different locations at Kohnen Station are not consistent. A stack of these data would thus result in no clear reflections within the firn (Tobias Binder, pers. comm.; Binder et al., 2016).

Taking the results of these two surveys and this thesis into account I doubt the presence of a sufficient impedance contrast to generate detectable reflections in the firn at Kohnen Station.

7. Conclusion and summary

The combination of reflection detection, diving wave analysis and ice-core analysis is unique. So far ice cores were mostly analyzed and interpreted below the FIT, since an accurate sampling of thin sections above that depth is very time consuming and not possible for some depth. Measurements of 3D structural data enables statements about firn structures without sampling thin sections. For many studies tracking of reflectors over a huge area is of interest and the exact velocity determination in firn is neglected or derived by the ice-core analysis. A reasonable velocity profile as well as ice properties detached from ice-core information, are found up to a depth of 77 m. Therefore, this study highlights the ability to derive information about physical properties of firn in absence of an ice core.

The visualization of reflections within the firn was not possible during processing. The problem with this data was, that the groundroll generated by the ElViS is overlaying possible reflections. The continuous increase in density within the firn pack results in bending of the rays, and thus, diving waves are generated. Diving waves with a small angle of incidence are reflected at the firn-air interface and are recorded as multiple diving waves. This resulted in a signal of the diving waves in at least three different times.

The second problem was the high amplitude groundroll like Love and Rayleigh waves. These waves contain lower velocities, when compared to diving waves and overlap a different area in the t-x domain. Additionally, the energy level of the groundroll is high enough to activate the parasitic resonance which can be seen as ringing in traces. Furthermore, the high amplitude of the groundroll is superimposed on other signals, impossible to be removed by frequency filters. The f-k filter and K-L transformation did not successfully remove groundroll which can be attributed to the dispersion and low velocity.

The high amplitude signal at 1.63 s mTT could be caused by a Rayleigh wave. A lateral velocity increase from west to east can be seen in the Rayleigh-wave data as well as in S-wave velocities.

The arrival of diving waves could be used to derive information about physical ice properties. The comparison of XCT densities and the conversion of P-wave velocities into density by Kohnen's formula showed a bad fit and highlights the need for an advancement of this relation. In contrast the relation found by Diez et al. (2013) showed a good fit for the converted S-wave velocities and the XCT densities.

The elastic moduli derived from inversion velocities and the XCT densities are in good agreement with the values derived by the FEA and highlight the applicability of the Herglotz-Wiechert inversion in firn. The comparison of the elastic tensors and Thomsen parameters show a weak anisotropy for a depth of 40–70 m. Above this depth a higher anisotropy is observed. COF distributions calculated for the EDML ice core below 50 m depth used in Diez et al. (2015) show no abrupt changes between 50–100 m depth. Anisotropy derived for depths less than 100 m is referred to as anisotropic layering. Only the part above 40 m shows a higher anisotropy. The assumption of a VTI medium and thus the calculation of the elastic tensor of a VTI medium is a good approach for this data. A calculation of NMO velocities for this anisotropic medium using Thomsen parameters would probably change the velocity-depth profiles insignificantly due to the low anisotropy and high uncertainty.

No abrupt changes in density, velocity, elastic moduli or anisotropy could be detected which could be an indication for an insufficient impedance contrast to cause a reflection. Small

changes in diving-wave velocities would be smoothed by the curve the data is fitted to, but variations in traveltime would cause a shift that would be visible in the data. The anisotropic layering or the smooth changes in velocity or density could probably cause sufficient impedance contrast, but no englacial reflections were observed within the firn in seismic data at Kohnen station. This could also be explained by insufficient changes in elastic properties or by the high amplitude groundroll that is superimposed on possible weak reflections. Reflections within a depth of 100 m would contain TWT smaller than 0.1 s and therefore would be located in the same traveltime range of the diving wave first breaks and the high amplitude groundroll. Former studies in other areas complemented seismic measurements with radar (for instance airborne radar measurements) to investigate the origin of reflections. Phase-sensitive radar (pRES) data recorded in 2015 and 2016 at Kohnen Station shows no continuous energy spikes in the backscatter over larger areas in the firn (Tobias Binder, pers. comm.). This indicates that no continuous reflections and thus no spatially continuous sufficient impedance contrast can be found at Kohnen Station within the firn.

I conclude that the impedance contrast at Kohnen Station is insufficient to make reflections within the firn detectable under the influence of the high amplitude groundroll. Velocities as well as elastic moduli derived from diving-waves velocities and XCT densities are in good agreement with values from the FEA. Even lateral velocity variations could be determined within the firn by diving-wave inversion. This study demonstrates the adaptability of the ElViS to achieve information about physical properties of firn. Especially the simple handling and the short preparation time of an ElViS measurement enables the user to derive a detailed velocity depth profile for the subsurface within a few days (depending on the measurement setup).

8. Outlook

The following list represents suggestions for further processing of the data or similar data as well as suggestions for further surveys.

Larger offsets during the measurement would enable diving-wave penetration until the FIT and even deeper. Additionally, far offset shots contain less ringing and high amplitude groundroll which improves the SNR.

Comparison of shots in the west and in the east of the profile with larger offsets would enable a statement of the lateral inhomogeneities as well as anisotropy.

Analysis of Rayleigh and Love waves would enable more detailed investigations of lateral inhomogeneities. The analysis of Rayleigh and Love waves in firn and ice was already introduced by Diez et al. (2016); Picotti et al. (2015). Furthermore, velocities of Rayleigh and Love waves could be converted into P- and S-wave velocities and could then be compared to velocities from diving-wave inversion.

Further investigation of the high amplitude event in 1.63 s mTT would hopefully make a statement about the origin of this signal possible. Therefore, the horizontal components of the P wave as well as components of the other modes should be processed and the possibility of a high amplitude signal in these components should be analyzed.

Ray tracing of multiple diving waves would probably result in detailed information about lateral variabilities in the upper meters of the firn.

Additional 3D-XCT measurements would decrease the uncertainty of single maximum values as seen for the Thomsen parameters in a depth of 10 m. An additional measurement in for instance 25 m depth would enable the calculation of a trend of the parameter and would probably support the increase of the Thomsen parameter with decreasing depth. Moreover, values of COF could be calculated from elastic tensors.

Intensive processing of the perpendicular profile could probably remove the wavy structure seen in the stack and enable the detection of clear events.

Bibliography

Al-Yahya, K. M. (1991). Application of the partial Karhunen-Loève Transform to suppress random noise in seismic sections. *Geophysical Prospecting*, 39(1):77–93.

Arnaud, L., Bamola, J. M., and Duval, P. (2000). Physical modeling of the densitication of snow / firn and ice in the upper part of polar ice sheets. (c).

Bader, H. (1960). Theory of Densification of Dry Snow on High polar Glaciers. *U.S. Snow, Ice and Permafrost Research Establishment. Research Report 769*, pages 1–8.

Baeten, G. (1989). *Theoretical and practical aspects of the Vibroseis method*. Dissertation, Delf University of Technology.

Bale, R., Gratacos, B., Mattocks, B., Roche, S., Poplavskii, K., and Lil, X. (2009). Shear wave splitting applications for fracture analysis and improved imaging: Some onshore examples. *First Break*, 27(9):73–83.

Benson, C. S. (1962). Stratigraphic studies in the snow and firn of the Greenland Ice Sheet. *Folia Geographica Danica*, 70(August):13–37.

Binder, T., Eisen, O., Helm, V., Humbert, A., and Steinhage, D. (2016). Phase-sensitive radar on thick Antarctic ice – how well does it work? *Geophysical Research Abstracts*, 18:17840.

Biot, M. a. and Lowrie, W. (2007). *Fundamentals of geophysics*, volume 28. Cambridge University Press.

Bormann, P. (2002). New Manual of Seismological Observatory Practice (NMSOP). In Bormann, P., editor, *Seismic signals and noise*, volume 1, chapter chapter, pages 1–34. GFZpublic Deutsches GeoForschungsZentrum GFZ, IASPEI, GFZ German Research Centre for Geosciences, Potsdam;.

Brittle, K. F., Lines, L. R., and Dey, A. K. (2001). Vibroseis deconvolution: A comparison of cross-correlation and frequency-domain sweep deconvolution. *Geophysical Prospecting*, 49(6):675–686.

Church, J. A., eterU. Clark, P., Cazenave, A., Gregory, J. M., Jevrejeva, S., Levermann, A., Merrifield, M. A., Milne, G. A., Nerem, R., Nunn, P. D., Payne, A. J., Pfeffer, W. T., Stammer, D., and Unnikrishnan, A. S. (2013). Sea level change. *Climate Change 2013: The Physical Science Basis. Contribution of Working Group I to the Fifth Assessment Report of the Intergovernmental Panel on Climate Change*, pages 1137–1216.

Cuffey, K. and Paterson, W. (2010). *The physics of glaciers*, volume 2. Academic Press, 4th editio edition.

Dewart, G. (1970). Seismic Investigation of Ice Properties and Bedrock Topography at the Confluence of the North and Central Arms of the Kaskawulsh Glacier. *Icefield Ranges Research Project Scientific Results: Volume 2*, pages 77–102.

Diez, A. (2013). *Effects of cold glacier ice crystal anisotropy on seismic data*. PhD thesis.

Diez, A., Bromirski, P. D., Gerstoft, P., Stephen, R. A., Anthony, R. E., Aster, R. C., Cai, C., Nyblade, A., and Wiens, D. A. (2016). Ice shelf structure derived from dispersion curve analysis of ambient seismic noise, Ross Ice Shelf, Antarctica. *Geophysical Journal International*, 205(2):785–795.

Diez, A., Eisen, O., Hofstede, C., Bohleber, P., and Polom, U. (2013). Joint interpretation of explosive and vibroseismic surveys on cold firn for the investigation of ice properties. *Annals of Glaciology*, 54(64):201–210.

Diez, A., Eisen, O., Hofstede, C., Lambrecht, A., Mayer, C., Miller, H., Steinhage, D., Binder, T., and Weikusat, I. (2015). Seismic wave propagation in anisotropic ice - Part 2: Effects of crystal anisotropy in geophysical data. *Cryosphere*, 9(1):385–398.

Diez, A., Eisen, O., Weikusat, I., Eichler, J., Hofstede, C., Bohleber, P., Bohlen, T., and Polom, U. (2014). Influence of ice crystal anisotropy on seismic velocity analysis. *Annals of Glaciology*, 55(67):97–106.

dos Santos, Q. C. and Porsani, M. J. (2013). Ground roll attenuation using shaping filters and band limited sweep signals. *Revista Brasileira de Geofisica*, 30(4):545–554.

Drücker, C., Wilhelms, F., Oerter, H., Frenzel, A., Gernandt, H., and Miller, H. (2002). Design, transport, construction, and operation of the summer base Kohnen for ice-core drilling in Dronning Maud Land. *Memoirs of National Institute of Polar Research*, 56(Special Issue):302–312.

Druivenga, G., Grossmann, E., Grüneberg, S., Polom, U., and Rode, W. (2005). Transportabler Scherwellenvibrator. Deutsches Patent- und Markenamt.

Eisen, O., Hofstede, C., Diez, A., Kristoffersen, Y., Lambrecht, A., Mayer, C., Blenkner, R., and Hilmarsson, S. (2015). On-ice vibroseis and snowstreamer systems for geoscientific research. *Polar Science*, 9(1):51–65.

Eisen, O., Hofstede, C., Miller, H., Kristoffersen, Y., Blenkner, R., Lambrecht, A., and Mayer, C. (2010). A new Approach for Exploring Ice Sheets and Sub-Ice Geology. *EOS, Transactions american geophysical union*, 91(46).

Eisen, O., Rack, W., Nixdorf, U., and Wilhelms, F. (2005). Characteristics of accumulation around the EPICA deep-drilling site in Dronning Maud Land, Antarctica. *Annals of Glaciology*, 41:41–46.

Etris, E., Crabtree, N., and Dewar, J. (2001). True depth conversion: More than a pretty picture. *CSEG recorder*, 26(9):11–21.

Faber, K. and Maxwell, P. W. (1997). Geophone spurious frequency: WHat is it and how does it affect seismic data quality? *Canadian Journal of Exploiration Geophysics*, 33:46–54.

Freitag, J., Kipfstuhl, S., and Faria, S. H. (2008). The connectivity of crystallite agglomerates in low-density firn at Kohnen station, Dronning Maud Land, Antarctica. *Annals of Glaciology*, 49(1):114–120.

Freitag, J., Kipfstuhl, S., and Laepple, T. (2013). Core-scale radioscopic imaging: A new method reveals density-calcium link in Antarctic firn. *Journal of Glaciology*, 59(218):1009–1014.

Freitag, J., Wilhelms, F., and Kipfstuhl, S. (2004). Microstructure-dependent densification of polar firn derived from X-ray microtomography. *Journal of Glaciology*, 50(169):243–250.

Gadallah, M. R. and Fisher, R. (2009). *Exploration geophysics*. Springer Berlin Heidelberg, Berlin, Heidelberg.

Gelinsky, S. and Shapiro, S. A. (1997). Poroelastic Backus averaging for anisotropic layered fluid- and gas-saturated sediments. *Geophysics*, 62(6):1867.

Gerling, B. (2016). *Determination of the elastic modulus of snow by acoustic methods and comparison to penetrometer measurements and numerical simulations*. PhD thesis.

Goujon, C. (2003). Modeling the densification of polar firn including heat diffusion: Application to close-off characteristics and gas isotopic fractionation for Antarctica and Greenland sites. *Journal of Geophysical Research*, 108(D24):1–18.

Goupillaud, P. L. (1976). Signal design on the "Vibroseis"Technique. *Geophysics*, 41(6):1291–1304.

Greenhalgh, S. A. and King, D. W. (2001). Curved Raypath Interpretation of Seismic Refraction Data. *Geophysical Pro*, 29(April 1982):542–543.

Hatton, L., Worthington, M., and Makin, J. (1991). *Seismic Data Processing*. Wiley-Blackwell, first edition.

Hearst, J. R., Nelson, P. H., and Paillett, F. L. (2000). *Well logging for physical properties*. Number 12. John Wiley & Sons, Ltd., Chichester, New York, Weinheim, second edition.

Herron, M. M. and Langway, C. C. (1980). Firn densification: an empirical model. *Journal of Glaciology*, 25(93):373–385.

Hobbs, P. (1968). The metamorphism of dry snow at a uniform temperature. *Union de Giodisie et Giophysique Intemationale. Association Intemationale d'Hydrologie Scientijique. Assemblie ginerale de Berne*, pages 392–402.

Hoerhold, M. W., Kipfstuhl, S., Wilhelms, F., Freitag, J., and Frenzel, A. (2011). The densification of layered polar firn. *Journal of Geophysical Research: Earth Surface*, 116(1):1–15.

Hofstede, C., Eisen, O., Diez, A., Jansen, D., Kristoffersen, Y., Lambrecht, A., and Mayer, C. (2013). Investigating englacial reflections with vibro-and explosive-seismic surveys at Halvfarryggen ice dome, Antarctica. *Annals of Glaciology*, 54(64):189–200.

Kaselow, A. (2004). *The Stress Sensitivity Approach: Theory and Application*. PhD thesis, Freie Universität Berlin.

Kearey, P., Brooks, M., and Hill, I. (2002). *Introduction To Geophysical Exploration*, volume 67. Blackwell Science, Oxford.

Keydar, S., Koren, Z., Kosloff, D., and Landa, E. (1989). Optimal time-to-depth conversion. *Geophysics*, 54(08):1001–1005.

Kirchner, J. F. and Bentley, C. R. (1990). RIGGS III: seismic short-refraction studies using an analytical curve- fitting technique. *The Ross Ice Shelf: glaciology and geophysics,American Geophysical Union,Washington, DC*, 42(5):109–126.

Klikauer, T. (2016). *Reflections on phishing for phools: The economics of manipulation and deception*. PhD thesis, Bremen.

Kohnen, H. (1972). Über die Beziehung zwischen seismischen Geschwindigkeiten und der Dichte in Firn und Eis. *Zeitschrift für Geophysik*, 38(5):925–935.

Londoño, E. G., López, L. C., Kazmierczak, T. D. S., and Kazmierczak, S. (2005). Using the Karhunen-Loève Transform To Suppress Ground Roll in Seismic Data. *Earth Sciences Research Journal*, 9(2):139–147.

Mavko, G., Mukerji, T., and Dvorkin, J. (2009). *The Rock Physics Handbook, Second Edition*. Cambridge University Press.

Meier, M. F., Dyurgerov, M. B., Rick, U. K., O'Neel, S., Pfeffer, W. T., Anderson, R. S., Anderson, S. P., and Glazovsky, A. F. (2007). 'Glaciers dominate Eustatic sea-level rise in the 21st century'. *Science*, 317(5841):1064–1067.

Mitrovica, J. X., Tamisiea, M. E., Davis, J. L., and Milne, G. A. (2001). Recent mass balance of polar ice sheets inferred from patterns of global sea-level change. *Nature*, 409(6823):1026–9.

Montagnat, M., Azuma, N., Dahl-Jensen, D., Eichler, J., Fujita, S., Gillet-Chaulet, F., Kipfstuhl, S., Samyn, D., Svensson, A., and Weikusat, I. (2014). Fabric along the NEEM ice core, Greenland, and its comparison with GRIP and NGRIP ice cores. *Cryosphere*, 8(4):1129–1138.

Münch, T., Kipfstuhl, S., Freitag, J., Meyer, H., and Laepple, T. (2015). Regional climate signal vs . local noise : a two-dimensional view of water isotopes in Antarctic firn at Kohnen station ,. *Climate of the Past Discussions*, 11:5605–5649.

Naderpajouh, N., Riahi, M. A., and Hashemi, H. (2011). Sensitivity of Eigen-value analysis based on K-L transform for seismic linear noise attenuation. *Iamg 2011*.

Nelson, S. A. (2010). *Glaciers and Glaciation*. Routledge, second edi edition.

Oerter, H., Drücker, C., Kipfstuhl, S., and Wilhelms, F. (2009). Kohnen Station - The drilling camp for the EPICA deep ice core in dronning maud land. *Polarforschung*, 78(1-2):1–23.

Okrusch, M. and Matthes, S. (2010). *Mineralogie*. Springer-Lehrbuch. Springer Berlin Heidelberg, Berlin, Heidelberg.

Picotti, S., Vuan, A., Carcione, J. M., Horgan, H. J., and Anandakrishnan, S. (2015). Anisotropy and crystalline fabric of Whillans Ice Stream (West Antarctica) inferred from multicomponent seismic data. *Journal of Geophysical Research B: Solid Earth*, 120(6):4237–4262.

Polom, U., Hofstede, C., Diez, A., and Eisen, O. (2014). First glacier-vibroseismic experiment - Results from cold firn of Colle Gnifetti. *Near Surface Geophysics*, 12(4):493–504.

Porsani, M. and Silva, M. (2010). SVD filtering applied to ground-roll attenuation. *Journal of Geophysics ...*, 7(3):284–289.

Pritchard, H., Ligtenberg, S., Fricker, H., Vaughan, D., van den Broeke, M., and Padman, L. (2012). Antarctic ice-sheet loss driven by basal melting of ice shelves. *Nature*, 484(7395):502–505.

Raper, S. C. B. and Braithwaite, R. J. (2013). Low sea level rise projections from mountain glaciers and icecaps under global warming. *Nature*, 439(January):311–313.

Reynolds, J. M. (2011). *An Introduction to Applied and Environmental Geophysics.*, volume 1. second edition.

Robin, G. D. Q. (1958). Seismic shooting and related investigations: Norwegian-British-Swedish Antarctic Expedition,1949–1952. *Scientific Results*, 5(Norsk Polarinstitutt, Oslo).

Rotschky, G., Holmlund, P., Isaksson, E., Mulvaney, R., Oerter, H., Van den Broeke, M. R., and Winther, J. G. (2007). A new surface accumulation map for western Dronning Maud Land, Antarctica, from interpolation of point measurements. *Journal of Glaciology*, 53(182):385–398.

Schulson, E. M. and Duval, P. (2009). *Creep and Fracture of Ice*. Cambridge University Press, 1 edition.

Schulz, I. (2013). *Bearbeitung von Vibroseis-Messungen zur Erkundung des Firns an der Kohnen Station , Antarktis Inna Schulz*. PhD thesis.

Shearer, P. M. (2009). *Introduction to Seismology*. Cambridge University Press.

Sheriff, R. E. and Geldart, L. P. (1995). *Exploration Seismology — Solid Earth Geophysics*. Cambridge University Press, second edition.

Slichter, L. B. (1932). The theory of the interpretation of seismic travel-time curves in horizontal structures. *Journal of Applied Physics*, 3(6):273–295.

Stanikova, D., Surova, M., Ticha, L., Petrasova, M., Virgova, D., Huckova, M., Skopkova, M., Lobotkova, D., Valentinova, L., Mokan, M., Stanik, J., Klimes, I., and Gasperikova, D. (2015). Melanocortin-4 receptor gene mutations in obese slovak children. *Physiological Research*, 64(6):883–890.

Steinhage, D., Nixdorf, U., Meyer, U., and Miller, H. (1999). New maps of the ice thickness and subglacial topography in Dronning Maud Land, Antarctica, determined by means of airborne radio-echo sounding. *Annals of Glaciology*, 29(1):267–272.

Taner, M.T. & Koehler, F. (1969). Velocity spectra – digital com- puter derivation and applications of velocity functions. *Geophysics*, 34(6):859–881.

Tatham, R. H. and McCormack, M. D. (1991). *3. Rock Physics Measurements. Multicomponent Seismology in Petroleum Exploration*. Society of Exploration Geophysicists.

Telford, W. M., Geldart, L. P., and Sheriff, R. E. (1990). *Applied Geophysics — Solid Earth Geophysics — Cambridge University Press*. second edition.

Thomsen, L. (1986). Weak elastic anisotropy. *Geophysics*, 51(10):1954.

Thomsen, L., Society of Exploration Geophysicists., and European Association of Geoscientists and Engineers. (2002). *Understanding seismic anisotropy in exploration and exploitation*. Society of Exploration Geophysicists. European Association of Geoscientists and Engineers.

Tipler, P. A. and Mosca, G. (2009). *Physik für Wissenschaftler und Ingenieure Physics for scientists and engineers <dt.>*. Spektrum Akademischer Verlag, 2 edition.

Torquato, S., Gibiansky, L., Silva, M., and Gibson, L. (1996). Effective mechanical and transport properties of cellular solids. *International Journal of Mechanical Sciences*, 40(1):71–82.

Tsvankin, I. (1997). Anisotropic parameters and P-wave velocity for orthorhombic media. *Geophysics*, 62(4):1292.

von Hartmann, H., Beilecke, T., Buness, H., Musmann, P., and Schulz, R. (2015). *Seismische Exploration für tiefe Geothermie*, volume B 104. Schweizerbart'sche Verlagsbuchhandlung.

Weiler, K. (2008). *On the Composition of Firn Air and its Dependence on Seasonally Varying Atmospheric Boundary Conditions and the Firn Structure*. PhD thesis, University of Bern.

Yilmaz, Ö. (2001). *Seismic data analysis*, volume 10.

Abbreviations and nomenclature

AWI	*Alfred-Wegener-Institut*
CDP	*Common Depth Point*
CMP	*Common MidPoint*
COF	*Crystal Orientation Fabric*
CVS	*Constant Velocity Stack*
DML	*Dronning Maud Land*
EDML	*EPICA Dronning Maud Land (ice core and borehole)*
EPICA	*European Project of Ice Coring in Antarctica*
ElViS	*Electrodynamic-Vibrator System*
f	*frequency*
FEA	*Finite Element Algorithm*
FIT	*Firn-Ice Transition*
f-k filter	*frequency-wavenumber frequency filter*
f-k domain	*frequency-wavenumber domain*
HVA	*Horizon Velocity Analysis*
ICE-CT	*X-ray microfocus Computed Tomograph*
k	*wavenumber*
mTT	*measured Traveltime*
NMO	*Normal MoveOut*
p	*ray parameter*
P wave	*compressional wave*
RMS	*Root Mean Square*
S wave	*shear wave*
SNR	*Signal-to-Noise Ratio*
SH wave	*horizontal shear wave*
SV wave	*vertical shear wave*

t-x domain *time-space domain*

TWT *Two-Way Traveltime*

vibroseis *vibrator seismic*

VTI *Vertical Transversely Isotropic*

x *offset*

XCT *X-ray Computed Tomography*

z *depth*

Thomsen parameter:

ε

γ

δ

List of Figures

List of Tables

Danksagung

An dieser Stelle möchte ich all jenen danken, die mich im Rahmen dieser Masterarbeit begleitet haben.

Zuerst gebührt mein Dank Herrn Prof. Olaf Eisen.
Danke für die Betreung, Themenstellung und schnelle Beantwortung von Fragen. Auch wenn es doch ein sehr holpriger Start war, habe ich sehr viel aus dieser Arbeit gelernt.

Herrn PD Karsten Gohl, danke für die Begutachtung dieser Arbeit.

Herrn Prof. Wilfried Jokat, danke ich für die wertvollen Beantwortungen meiner Fragen.

Vielen Dank gilt außerdem meinen Freunden und Kollegen am AWI: Anna Winter, Katharina Hochmuth, Tanja Fromm, Christoph Schaller, Johannes Freitag, Martin Rückamp, Matthias Hühter und Tetsuro Taranczewski - vielen Dank für eure Korrekturen, Kommentare und eure stetige Hilfsbereitschaft.

Ein großes Dankeschön an meinen Eltern und meiner Schwester, die mich nicht nur während der Masterarbeit, sondern während meines gesamten Studiums tatkräftig unterstützt und ermutigt haben.

Ein ganz besonderer Dank gilt meinem Honki.
Danke für die Unterstützung während der Arbeit. Auch wenn du vermutlich bis heute nicht verstehst was genau ich gemacht habe, hast du immer versucht mich bestmöglichst zu unterstützen.

Nicht zuletzt möchte ich mich bei Anja Diez bedanken. Vielen Dank, dass du dir so spontan Zeit genommen hast meine Arbeit zu lesen. Außerdem danke ich dir für die Beantwortung meiner Fragen.

Auch all denen, die hier nicht namentlich genannt wurden, gilt mein herzlicher Dank.

A. Appendix

In the following additional figures and equation referred to in the Chapters above are given. Moreover two used Matlab scripts are attached. The first is given with values for the velocity calculation by diving wave inversion. The second is given without example values, since the second script refers to the results of the first script.

A.1. Supplementary figures

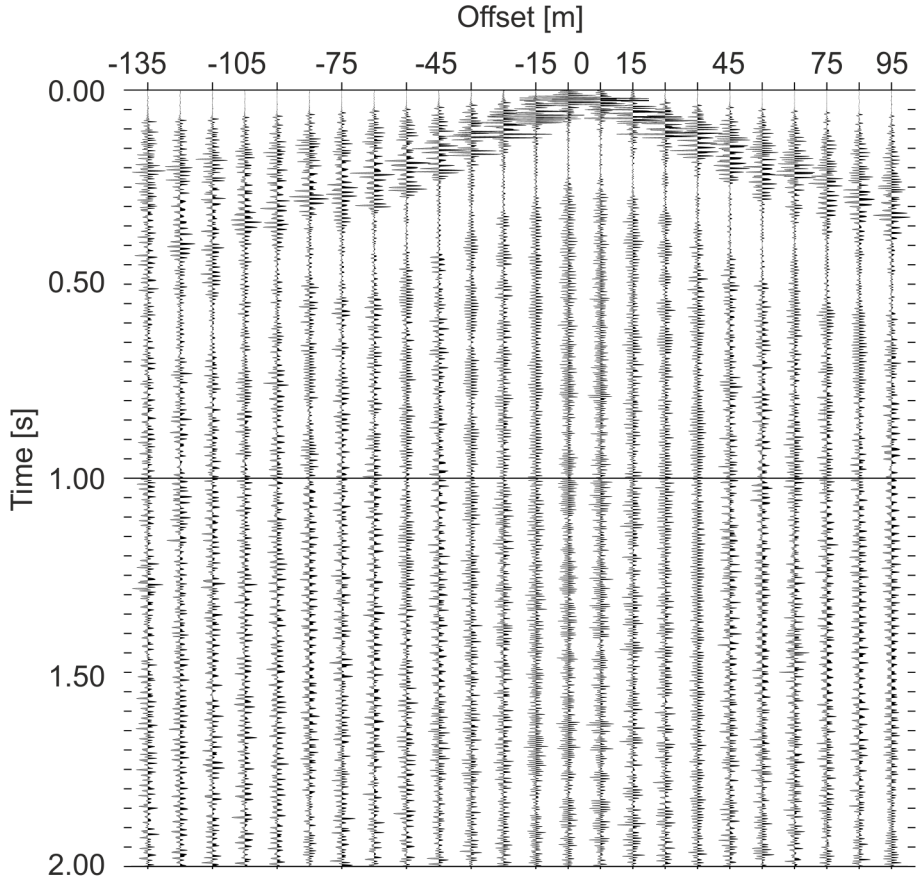

Figure A.1.: Vertical component of P-wave shot 70 of the parallel profile displayed in full recording length.

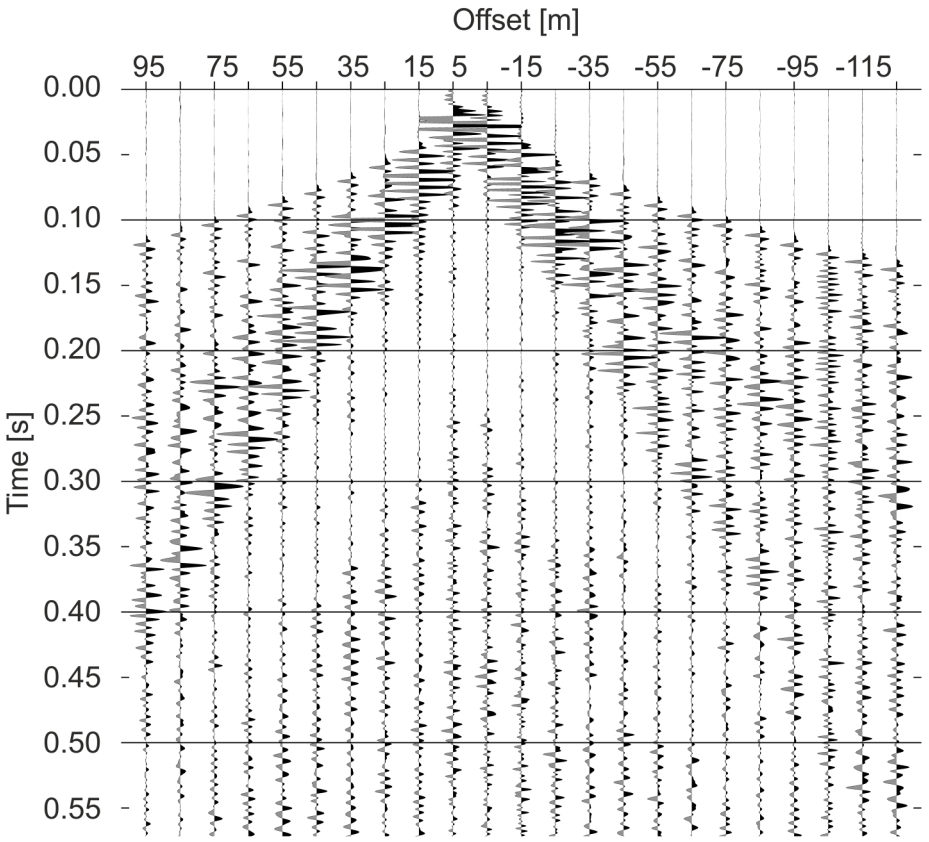

Figure A.2.: Horizontal component of SH-wave shot 24 of the parallel profile. Only the upper part of the seismogram is displayed.

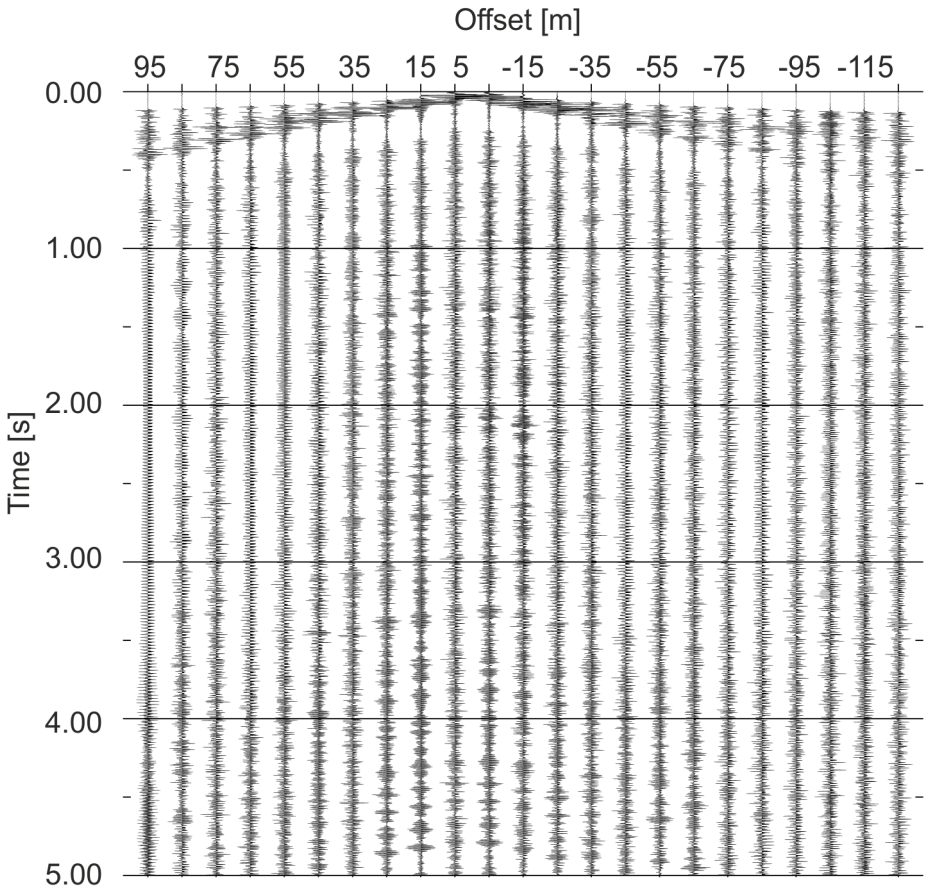

Figure A.3.: Horizontal component of SH-wave shot 24 of the parallel profile displayed in full recording length.

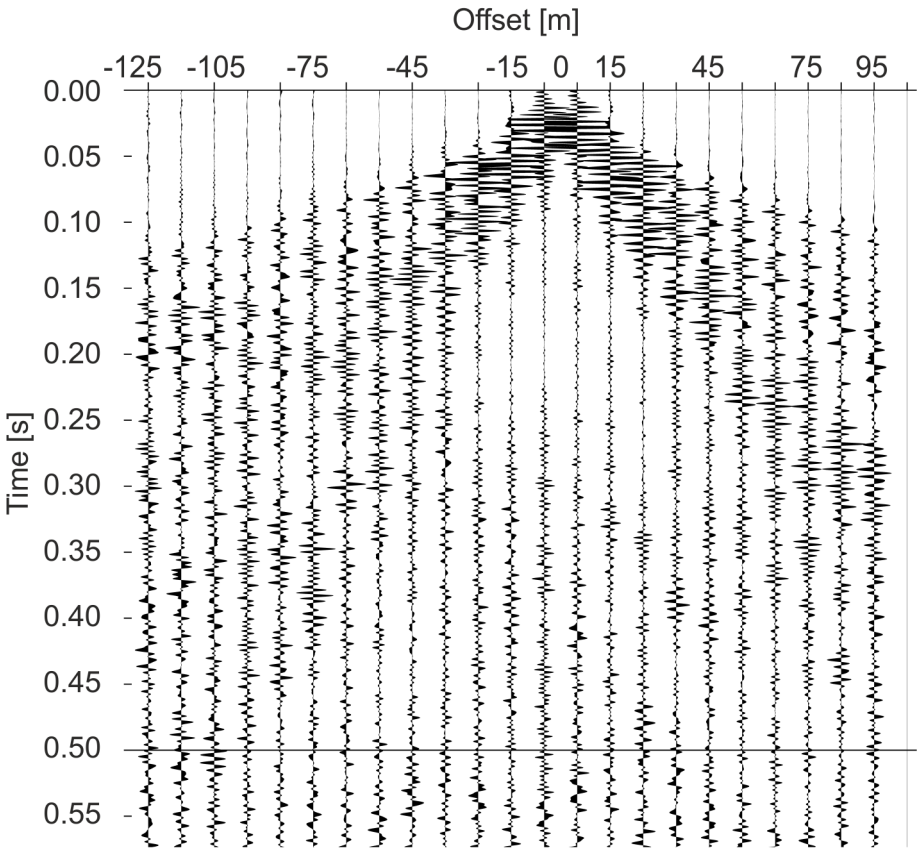

Figure A.4.: Horizontal component of SV-wave shot 20 of the parallel profile displayed in full recording length.

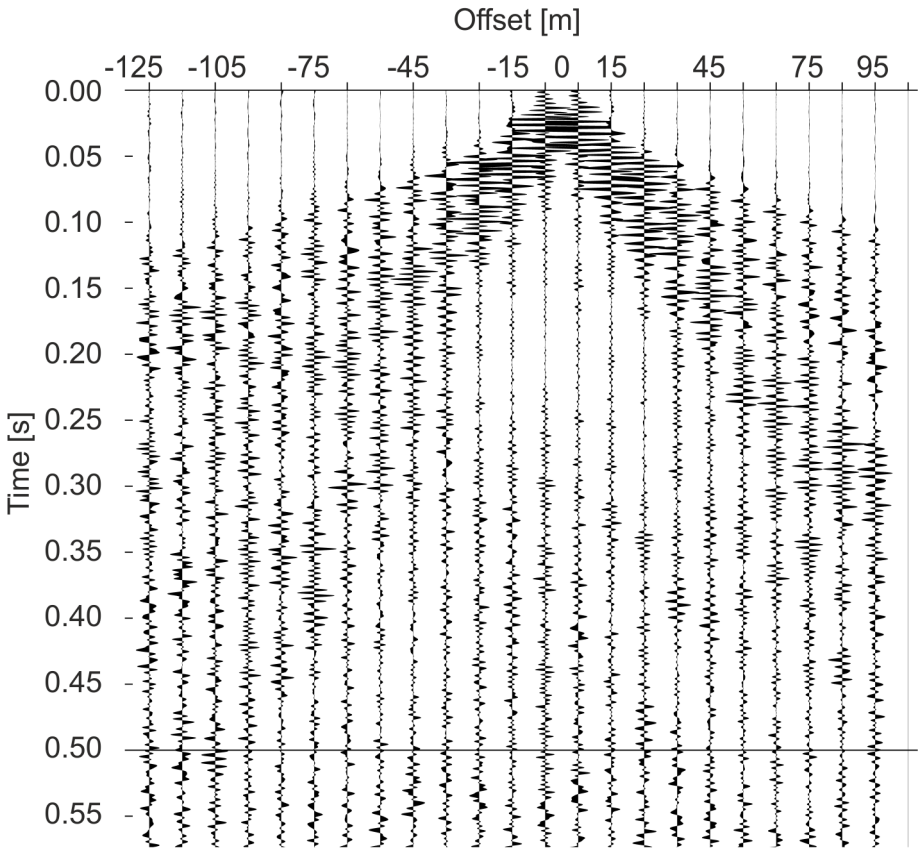

Figure A.5.: Horizontal component of SV-wave shot 20 of the parallel profile displayed in full recording length.

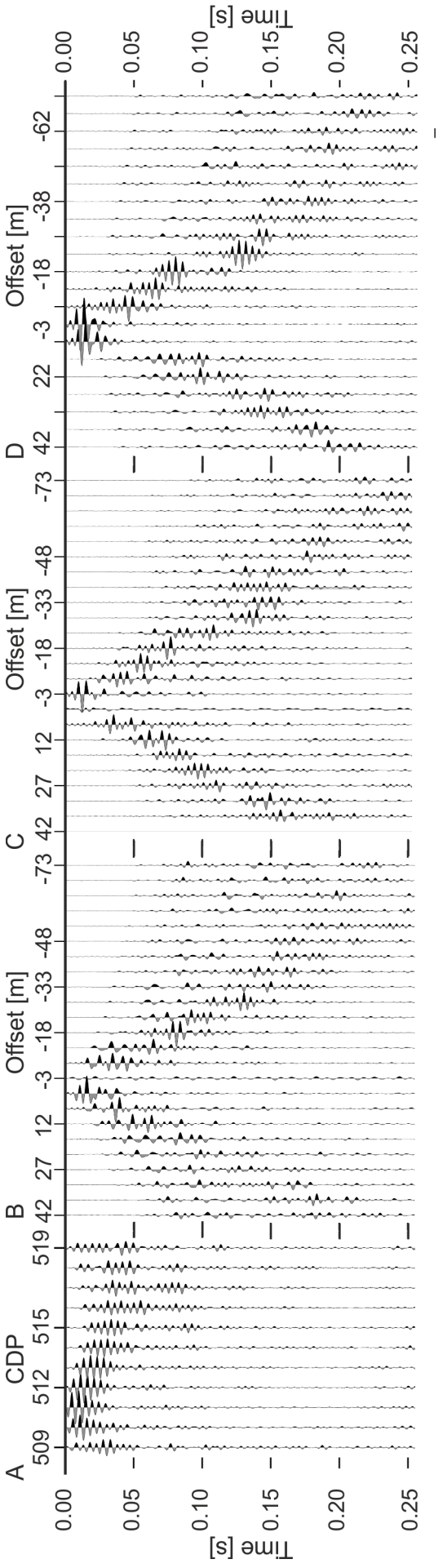

Figure A.6.: Stack and shot in three different components of the P-wave, perpendicular profile.

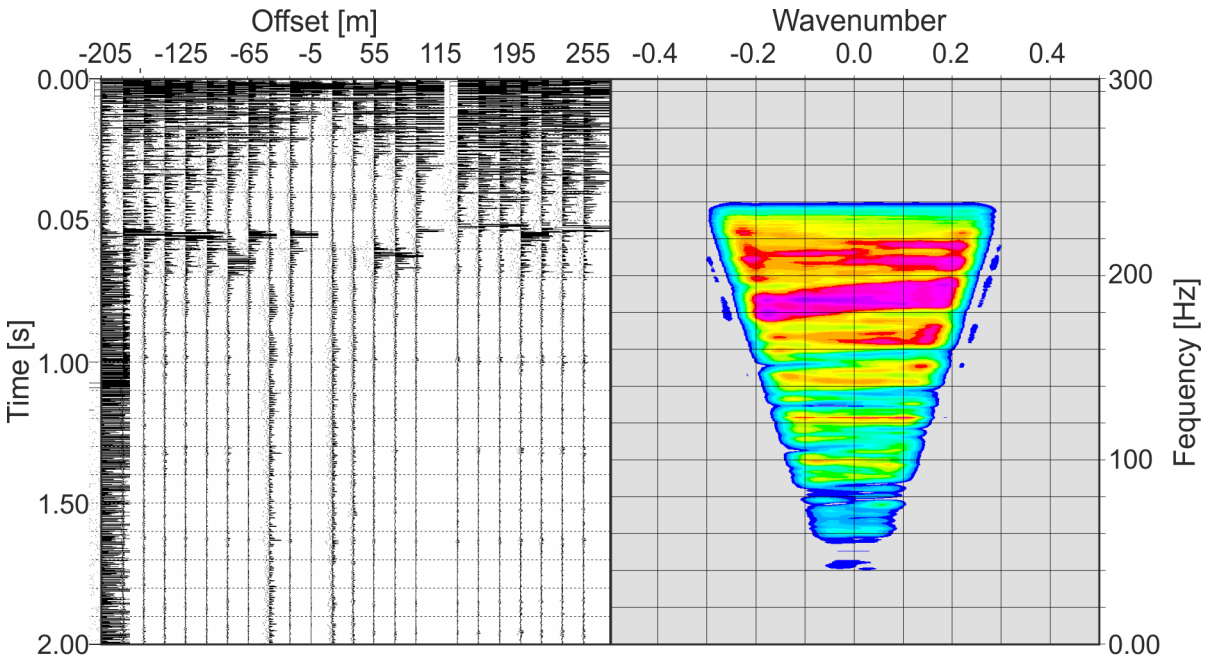

Figure A.7.: Results of the application of a dip-f-kfilter on P-wave shots of group three.

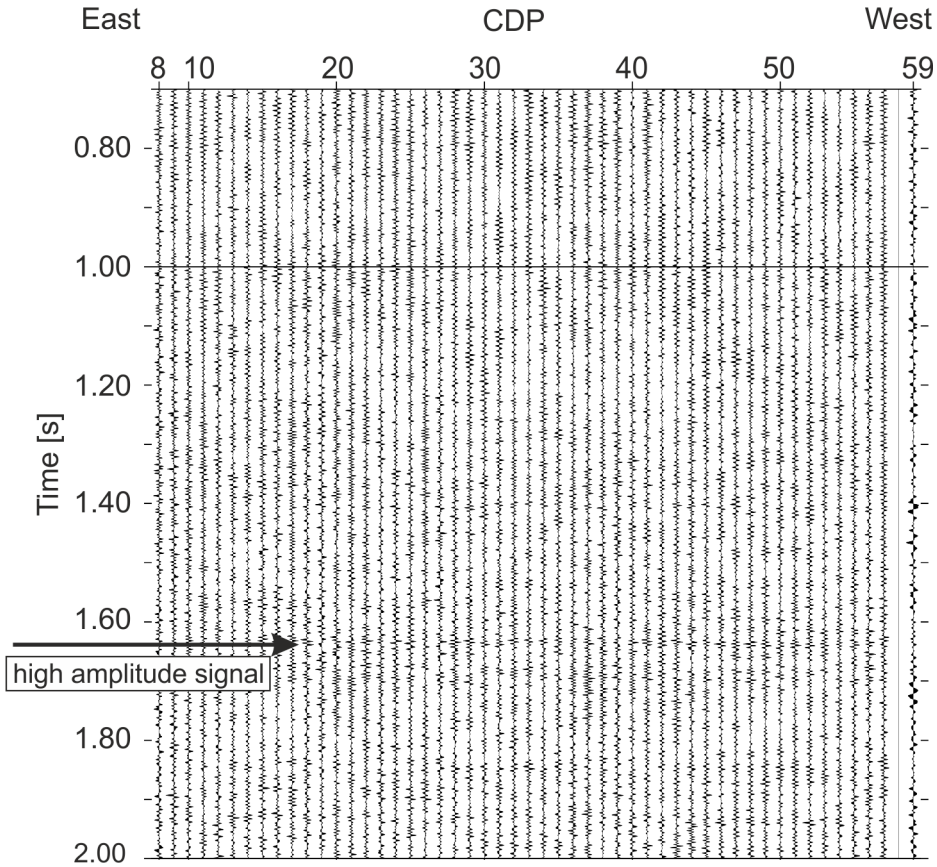

Figure A.8.: Stack of P-wave data parallel to the ice divide in the wiggle-mode. A higher amplitude can be observed along the profile at 1.63 s mTT

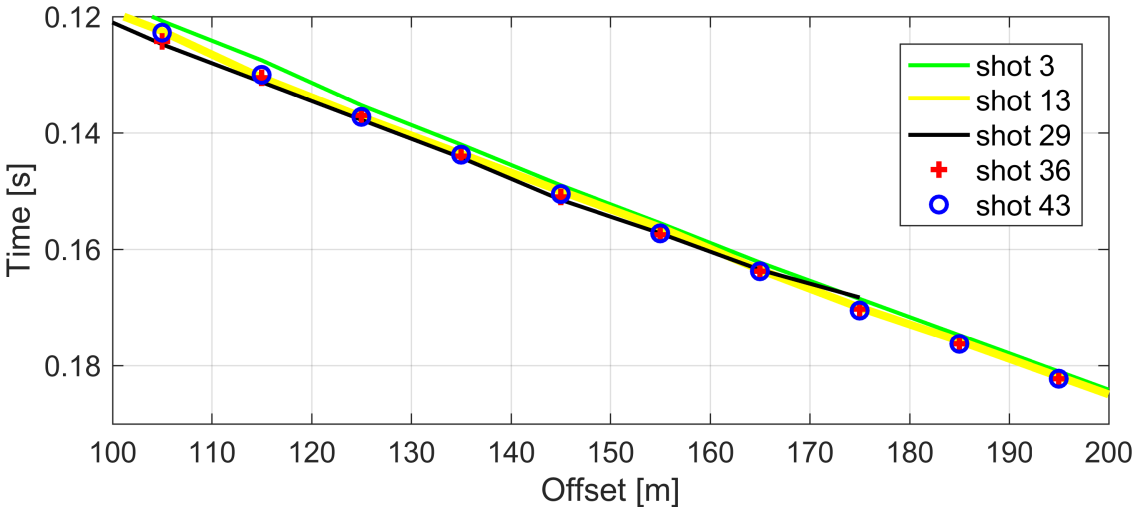

Figure A.9.: Plot of offset-traveltime pairs for SH-wave shot 3, 13, 29, 36 and 43. Shots are labeled and taken from east to west (shot 3 represents offset-traveltime pairs of the east, likewise shot 43 of the west).

A.2. Supplementary equations

A.2.1. Calculation of speed velocity

According to Drücker et al. (2002) the air temperature at Kohnen station ranges between $-20°C$ and $-45°C$ during the austral summer (December-February). The speed of sound in fluids is proportional to the temperature of the liquid. The velocity can be calculated by the following formula:

$$V_{sound} = \sqrt{\frac{\gamma \cdot R \cdot T}{m_{Mol}}} \tag{A.1}$$

where γ is a constant, dependent on the type of gas, for air it is determined to be 1.4. R is the gas constant with a value of $8.314 \mathrm{J\,mol^{-1}\,K^{-1}}$, T the temperature in Kelvin and m_{Mol} is the molecular weight, for air defined to be $29 \cdot 10^{-3} \mathrm{\,kg\,mol^{-1}}$ (Tipler and Mosca, 2009).

A.2.2. Calculation of Rayleigh-wave velocity

The following equation is defined as the Rayleigh function (Shearer, 2009):

$$(2r^2 - \frac{1}{v_s(z)^2})^2 - 4r^2\sqrt{(r^2 - \frac{1}{v_p(z)^2})}\sqrt{(r^2 - \frac{1}{v_s(z)^2})} = 0 \tag{A.2}$$

the horizontal slowness r is dependent on the P-wave velocity v_p and the S-wave velocity v_s. The phase velocity of the Rayleigh wave $v_{rayleigh}$ is defined as:

$$v_{rayleigh}(z) = \frac{1}{r} \tag{A.3}$$

A.3. Matlab scripts

```
%--------------------------------------------------------------------------
% Plotting Figures Master Thesis Rebecca Schlegel
%--------------------------------------------------------------------------

% Author: Rebecca Schlegel
% schlegel-rebecca@gmx.de

% Matlab 2016a
% Skript Version 1.1
% 2016 07 14

% calculation of elastic moduli and components of the elastic tensor
from
% diving wave velocities and XCT densities.
%inpit: components as well as elasrtic moduli from FEA. Velocities
derived
%by Skrip 'Herglotz-Wiechert-Inversion' and XCT densities.


%--------------------------------------------------------------------------
% velo_depth_P = matrix with velocity-depth values derived for the P
wave
% velo_depth_SH = matrix with velocity-depth values derived for the SH
wave
% velo_depth_SV = matrix with velocity-depth values derived for the SV
wave
% rho_depth_P = matrix with density-depth values derived for the P wave
% rho_depth_SH = matrix with density-depth values derived for the SH
wave
% rho_depth_SV = matrix with density-depth values derived for the SV
wave

%vp_FEA & vs_FEA = velocities derived from values of the algorithm for
depth_FEA

%vp_core&vs_core = velocities calculated by Kohnen's and Diez's formula
%from XCT densities

%c_11-c_66 = components of the elastic tensor derived from the FEA

%K_sv&K_sh = bulk modulus derived from XCT density, P- and SV,
respectively
%SH-wave velocities

%mu_sv&mu_sh = shear modulus derived from XCT density, P- and SV,
respectively
%SH-wave velocities

%poi_sv&poi_sh= poisson ratio derived from P- and SV-, respectively SH-
wave
%velocities
%--------------------------------------------------------------------------
```

```
clear all
close all
clc
format long


% Loading Variables
load('workspace_Herglotz_wiechert.mat')



velo_p_i=velo_depth_P(:,1);
z_p_i=velo_depth_P(:,2);
velo_sh_i=velo_depth_SH(:,1);
z_sh_i=velo_depth_SH(:,2);
velo_sv_i=velo_depth_SV(:,1);
z_sv_i=velo_depth_SV(:,2);
delta_vp_i=delta_velo_depth_P(:,1);
delta_vsh_i=delta_velo_depth_SH(:,1);
delta_vsv_i=delta_velo_depth_SV(:,1);
%% Calculation of elastic moduli from SH-wave velocities and XCT
densities

%calculation poisson ratio
poi_sh=((velo_p_i.^2)-(2*velo_sh_i.^2))./(2*((velo_p_i.^2)-
(velo_sh_i.^2)));
delta_poi_sh=sqrt((((1./(velo_p_i.^2-
velo_sh_i.^2).^2).*(velo_p_i.*velo_sh_i.^2.*delta_vp_i)).^2)+((1./(velo
_p_i.^2-velo_sh_i.^2).^2).*(-velo_p_i.^2.*velo_sh_i.*delta_vsh_i)).^2);

% calculation mu; shear modulus
mu_sh=(velo_sh_i.^2).*meanDen_i;
delta_mu_sh=sqrt((2*velo_sh_i.*meanDen_i.*delta_vsh_i).^2+(velo_sh_i.^2
.*delta_mean_den_i).^2);

% calculation K; bulk modulus
K_sh=((velo_p_i.^2).*meanDen_i)-((4/3)*mu_sh);
delta_K_sh=sqrt((2*velo_p_i.*meanDen_i.*delta_vp_i).^2+(velo_p_i.^2.*de
lta_mean_den_i).^2+(4/3*delta_mu_sh).^2);

%% Calculation of elastic moduli from SV-wave velocities and XCT
densities

%calculation poisson ratio
poi_sv=((velo_p_i.^2)-(2*velo_sv_i.^2))./(2*((velo_p_i.^2)-
(velo_sv_i.^2)));
delta_poi_sv=sqrt((((1./(velo_p_i.^2-
velo_sv_i.^2).^2).*(velo_p_i.*velo_sv_i.^2.*delta_vp_i)).^2)+((1./(velo
_p_i.^2-velo_sv_i.^2).^2).*(-velo_p_i.^2.*velo_sv_i.*delta_vsv_i)).^2);

%calculation mu; shear modulus
mu_sv=(velo_sv_i.^2).*meanDen_i;
```

```
delta_mu_sv=sqrt((2*velo_sv_i.*meanDen_i.*delta_vsv_i).^2+(velo_sv_i.^2
.*delta_mean_den_i).^2);

%calculation K; bulk modulus
K_sv=((velo_p_i.^2).*meanDen_i)-((4/3)*mu_sv);
delta_K_sv=sqrt((2*velo_p_i.*meanDen_i.*delta_vp_i).^2+(velo_p_i.^2.*de
lta_mean_den_i).^2+(4/3*delta_mu_sv).^2);
%% Calculation of components of the elastic tensor from diving wave
inversion velocities
c_66_FEA=(-c_12_FEA+c_11_FEA)/2
c_33_P=((velo_p_i/1000).^2).*(Density_i/1000);
delta_c_33_P=sqrt((2.*velo_p_i/(1000^2).*delta_vp_i).^2+((Density_i*0.0
2).*(velo_p_i/1000).^2./1000).^2)
c_44_sh=((velo_sh_i/1000).^2).*(Density_i/1000);
delta_c_44_SH=sqrt((2.*velo_sh_i/(1000^2).*delta_vsh_i).^2+((Density_i*
0.02).*(velo_sh_i/1000).^2./1000).^2)
c_44_sv=((velo_sv_i/1000).^2).*(Density_i/1000);
delta_c_44_SV=sqrt((2.*velo_sv_i/(1000^2).*delta_vsv_i).^2+((Density_i*
0.02).*(velo_sv_i/1000).^2./1000).^2)


%% Figure Ice Core Density
fig1=figure(1); %Figure 3.4,density with depth at Kohnen Station

plot(Density_i,Depth_i,'b')

grid on

h1_legend=legend('density ice core B40');
h1_legend.Location='southwest';

xlabel('Density [kg m^{-3}]','FontSize', 11);
ylabel('Depth [m]','FontSize', 11);
axis([200 1000 0 90])
set(gca,'YDir','reverse','FontSize', 11)

fig1.Units='centimeters';
fig1.Position=[20 10 10 8];
fig1.PaperPositionMode='auto';
print('Density','-dpng','-r500')


 %% Figure SH-wave Shear and Bulk Modulus
fig2=figure(2); %Figure 5.19,elastic moduli with SH-and P-wave
velocities

filler=fill([mu_sh'-
delta_mu_sh';mu_sh'+delta_mu_sh'],[z_sh_i';z_sh_i'],'b','edgecolor','g'
,'edgealpha',0.08)
hold on
filler=fill([K_sh'-
delta_K_sh';K_sh'+delta_K_sh'],[z_sh_i';z_sh_i'],'y','edgecolor','r','e
dgealpha',0.08)
```

```
p21=plot(mu_sh,z_sh_i,'k','LineWidth',3)

p22=plot(G_FEA,depth_FEA,'*g','LineWidth',3)

p_ttt=errorbarxy(G_FEA,depth_FEA, (G_FEA'*0.18)',[],{'ko', 'g', 'r'})

p25=plot(K_sh,z_sh_i,'r','LineWidth',3)

p23=plot(K_FEA,depth_FEA,'*r','LineWidth',3)

p_tt=errorbarxy(K_FEA,depth_FEA, (delta_K_FEA')',[],{'ko', 'r', 'r'})

p24=plot(K_FEA_c33,depth_FEA,'*b','LineWidth',3)

p_tttt=errorbarxy(K_FEA_c33,depth_FEA, (delta_K_FEA_c_33')',[],{'ko',
'b', 'r'})

grid on
xlabel('Moduli [Pa]','FontSize', 11);
ylabel('Depth [m]','FontSize', 11);
axis([0 7000000000 0 80])
set(gca,'YDir','reverse','FontSize',11,'FontName','arial')

h2_legend=legend([p21,p22,p25,p24,p23],['shear modulus calculated' 10
'by SH-wave velocities'],...
     ['shear modulus calculated' 10 'by component c_{55}'],...
     ['bulk modulus calculated' 10 'by SH-wave velocities'],...
     ['bulk modulus calculated' 10 'by component c_{11}'],...
     ['bulk modulus calculated' 10 'by component c_{33}']);

set(h2_legend,'FontSize',11);
h2_legend.Location='westoutside';

fig2.Units='centimeters';
fig2.Position=[20 10 17 7];
fig2.PaperPositionMode='auto';

print('moduli_SH','-dpng','-r500')


 %% Figure SV-wave Shear and Bulk Modulus

fig3=figure(3); %Figure 5.18, elastic moduli with SV-and P-wave
velocities

filler=fill([mu_sv'-
delta_mu_sv';mu_sv'+delta_mu_sv'],[z_sv_i';z_sv_i'],'b','edgecolor','g'
,'edgealpha',0.08)
hold on
filler=fill([K_sv'-
delta_K_sv';K_sv'+delta_K_sv'],[z_sv_i';z_sv_i'],'y','edgecolor','r','e
dgealpha',0.08)
```

```
p3=plot(mu_sv,z_sv_i,'k','LineWidth',3)

p4=plot(G_FEA,depth_FEA,'og','LineWidth',3)

p_ttt=errorbarxy(G_FEA,depth_FEA, (G_FEA'*0.18)',[],{'ko', 'g', 'r'})

p_ttt=errorbarxy(G_FEA,depth_FEA, (G_FEA'*0.18)',[],{'ko', 'g', 'r'})

p6=plot(K_sv,z_sv_i,'r','LineWidth',3)

p7=plot(K_FEA,depth_FEA,'xr','LineWidth',3)

p_tt=errorbarxy(K_FEA,depth_FEA, (delta_K_FEA')',[],{'ko', 'r', 'r'})

p8=plot(K_FEA_c33,depth_FEA,'*b','LineWidth',3)

p_tttt=errorbarxy(K_FEA_c33,depth_FEA, (delta_K_FEA_c_33')',[],{'ko',
'b', 'r'})


grid on
xlabel('Moduli [Pa]','FontSize', 11);
ylabel('Depth [m]','FontSize', 11);
axis([0 7000000000 0 80])
set(gca,'YDir','reverse','FontSize',11,'FontName','arial')

h3_legend=legend([p3,p4,p6,p7,p8],['shear modulus calculated' 10 'by
SV-wave velocities'],...
     ['shear modulus calculated ' 10 'by component c_{55}'],...
     ['bulk modulus calculated' 10 'by SV-wave velocities'],...
     ['bulk modulus calculated' 10 'by component c_{11}'],...
     ['bulk modulus calculated' 10 'by component c_{33}']);

set(h3_legend,'FontSize',11);
h3_legend.Location='westoutside';

fig3.Units='centimeters';
fig3.Position=[20 10 17 7];
fig3.PaperPositionMode='auto';

print('moduli_SV','-dpng','-r500')
%% Figure Poisson Ratio

fig4=figure(4); %Figure 5.20, poisson's ratio

filler=fill([poi_sv'-
delta_poi_sv';poi_sv'+delta_poi_sv'],[z_sv_i';z_sv_i'],'y','edgecolor',
'y','edgealpha',0.08)
hold on
filler=fill([poi_sh'-
delta_poi_sh';poi_sh'+delta_poi_sh'],[z_sh_i';z_sh_i'],'r','edgecolor',
'r','edgealpha',0.08)
```

```
p10=plot (poi_sv,z_sv_i,'k','LineWidth',3);

p11=plot (poi_sh,z_sh_i,'r','LineWidth',3);

p12=plot (Poi_FEA,depth_FEA,'*b','LineWidth',3);

p_vp=errorbarxy(Poi_FEA,depth_FEA, (delta_poi_FEA),[],{'ko', 'b', 'r'})


grid on
xlabel('Poisson ratio','FontSize', 11);
ylabel('Depth [m]','FontSize', 11);
axis([0 0.5 0 80])
set(gca,'YDir','reverse','FontSize',11,'FontName','arial')


h4_legend=legend([p10,p11,p12],['poisson ratio calculated from' 10 'SV-
and P-wave velocities'],...
     ['poisson ratio calculated from' 10 'SH- and P-wave
velocities'],...
     ['poisson ratio calculated from ' 10 'FEA velocities']);

set(h4_legend,'FontSize',11);
h4_legend.Location='westoutside';

fig4.Units='centimeters';
fig4.Position=[20 10 17 8];
fig4.PaperPositionMode='auto';

print('poisson_ratio','-dpng','-r500')


 %% Figure Velocities

fig5=figure(5);%Figure 5.17; velocities

filler=fill([velo_p_i'-
delta_vp_i';velo_p_i'+delta_vp_i'],[z_p_i';z_p_i'],'g','edgecolor','g',
'edgealpha',0.08)
hold on
filler=fill([velo_sv_i'-
delta_vsv_i';velo_sv_i'+delta_vsv_i'],[z_sv_i';z_sv_i'],'r','edgecolor'
,'r','edgealpha',0.08)

filler=fill([velo_sh_i'-
delta_vsh_i';velo_sh_i'+delta_vsh_i'],[z_sh_i';z_sh_i'],'y','edgecolor'
,'y','edgealpha',0.08)

p30=plot(velo_p_i,z_p_i,'Color',[0.2 0.8 0],'LineWidth',3)

p31=plot(velo_sv_i,z_sv_i,'r','LineWidth',3)
```

```
p32=plot(velo_sh_i,z_sh_i,'y','LineWidth',3)

p33=plot(vp_FEA,depth_FEA,'xc','LineWidth',3)

p_vp=errorbarxy(vp_FEA,depth_FEA, (delta_vp_FEA),[],{'ko', 'c', 'c'})

p34=plot(vs_FEA,depth_FEA,'xk','LineWidth',3)

p_vs=errorbarxy(vs_FEA,depth_FEA, (delta_vs_FEA),[],{'ko', 'k', 'k'})

p35=plot(v_p_core,Depth_i,'b','LineWidth',2)

p36=plot(v_s_core,Depth_i,'b','LineWidth',1)


grid on
xlabel('Velocity [m s^{-1}]','FontSize', 11);
ylabel('Depth [m]','FontSize', 11);
axis([0 4000 0 80])
set(gca,'YDir','reverse','FontSize',11,'FontName','arial')


h5_legend=legend([p30,p31,p32,p33,p34,p35,p36],['P-wave velocity'],...
     ['SV-wave velocity'],...
     ['SH-wave velocity'],...
     ['P-wave velocity' 10 'from component c_{33}'],...
     ['S-wave velocity' 10 'from component c_{55}'],...
     ['P-wave velocity' 10 'from XCT density'],...
     ['S-wave velocity' 10 'from XCT density']);

set(h5_legend,'FontSize',11);
h5_legend.Location='westoutside';

fig5.Units='centimeters';
fig5.Position=[20 10 17 8];
fig5.PaperPositionMode='auto';

print('velocity','-dpng','-r500')


%% Figure Components of the Elastic Tensor

fig6=figure(6); %Figure 6.4, components of the elastic moduli

filler=fill([c_33_P'-
delta_c_33_P';c_33_P'+delta_c_33_P'],[Depth_i';Depth_i'],'g','edgecolor
','g','edgealpha',0.08)
hold on
filler=fill([c_44_sv'-
delta_c_44_SV';c_44_sv'+delta_c_44_SV'],[Depth_i';Depth_i'],'r','edgeco
lor','r','edgealpha',0.08)
```

```
filler=fill([c_44_sh'-
delta_c_44_SH';c_44_sh'+delta_c_44_SH'],[Depth_i';Depth_i'],'y','edgeco
lor','y','edgealpha',0.08)

p_15=errorbarxy(c_66_FEA,depth_FEA, (c_66_FEA*0.182),[],{'go', 'g',
'g'})

p_11=errorbarxy(c_33_FEA,depth_FEA, (c_33_FEA*0.182),[],{'co', 'c',
'c'})

p_11=errorbarxy(c_11_FEA,depth_FEA, (c_11_FEA*0.182),[],{'bo', 'b',
'b'})

p_11=errorbarxy(c_44_FEA,depth_FEA, (c_44_FEA*0.182),[],{'ko', 'k',
'k'})

p1=scatter(c_33_P,Depth_i,10,'MarkerFaceColor',[0.2 0.8 0],
'MarkerEdgeColor','none')

p4=scatter(c_44_sh,Depth_i,10,'MarkerFaceColor',[1 1 0],
'MarkerEdgeColor','none')

p6=scatter(c_44_sv,Depth_i,10,'MarkerFaceColor',[1 0 0],
'MarkerEdgeColor','none')


p5=plot(c_44_FEA,depth_FEA,'k.','Markersize',19)

p9=plot(c_66_FEA,depth_FEA,'g.','Markersize',19)

p2=plot(c_11_FEA,depth_FEA,'b.','Markersize',19)

p3=plot(c_33_FEA,depth_FEA,'c.','Markersize',19)



grid on
xlabel('Elastic Tensor','FontSize', 11);
ylabel('Depth [m]','FontSize', 11);
axis([0 10 0 80])
set(gca,'YDir','reverse','FontSize',11,'FontName','arial')

%++++++++++++++++++++++++++++++++++++++++++++++++++++++++++++++++++++++
+++
% Variante A Legend beneath Plot
%++++++++++++++++++++++++++++++++++++++++++++++++++++++++++++++++++++++
+++

h6_legend=legend([p2,p1,p3 ,p4,p6, p5, p9],'Component c_{11} calculated
by FEA','Component c_{33} calculated by seismic P-wave
velocities','Component c_{33} calculated by FEA','Component c_{55}
calculated by seismic SH-wave velocities','Component c_{55} calculated
```

```
by seismic SV-wave velocities', 'Component c_{55} calculated by
FEA','Component c_{66} calculated by FEA');
set(h6_legend,'FontSize',11);
h6_legend.Location='southoutside';

fig6.Units='centimeters';
fig6.Position=[20 10 15 12];
fig6.PaperPositionMode='auto';

%++++++++++++++++++++++++++++++++++++++++++++++++++++++++++++++++++++++++
% Variante B Legend beneath Plot
%++++++++++++++++++++++++++++++++++++++++++++++++++++++++++++++++++++++++

% h6_legend=legend([p2,p1,p3,p4,p6,p5,p9],['Component c_{11}
calculated' 10 'by FEA'],...
%      ['Component c_{33} calculated by' 10 'seismic P-wave
velocities'],...
%      ['Component c_{33} calculated' 10 'by FEA'],...
%      ['Component c_{55} calculated by' 10 'seismic SH-wave
velocities'],...
%      ['Component c_{55} calculated by' 10 'seismic SV-wave
velocities'],...
%      ['Component c_{55} calculated' 10 'by FEA'],...
%      ['Component c_{66} calculated' 10 'by FEA']);
%
% set(h6_legend,'FontSize',11);
% h6_legend.Location='westoutside';
%
% fig6.Units='centimeters';
% fig6.Position=[20 10 18 8];
% fig6.PaperPositionMode='auto';

print('component_elastic_tensor','-dpng','-r500')
%% Figure Thomsen Parameter

fig7=figure(7);%Figure 6.5, Thomsen parameter

% Calculations
c_66_FEA=(-c_12_FEA+c_11_FEA)/2;
e=(c_11_FEA-c_33_FEA)./(2*c_33_FEA);
gamma=(c_66_FEA-c_44_FEA)./(2*c_44_FEA);
delta=((c_13_FEA+c_44_FEA).^2-(c_33_FEA-
c_44_FEA).^2)./(2*c_33_FEA.*(c_33_FEA-c_44_FEA));

% Plotting
plot(abs(e),depth_FEA,'r.','Markersize',22)
hold on
plot(abs(gamma),depth_FEA,'g.','Markersize',22)

plot(abs(delta),depth_FEA,'b.','Markersize',22)


grid on
```

```
xlabel('Thomsen parameters','FontSize', 11);
ylabel('Depth [m]','FontSize', 11);
axis([0 0.14 0 80])
set(gca,'YDir','reverse','FontSize',10,'FontName','arial')

h7_legend=legend('\bf\epsilon','\bf\gamma','\bf\delta');

set(h7_legend,'FontSize',11);
h7_legend.Location='east';


fig7.Units='centimeters';
fig7.Position=[20 10 15 7];
fig7.PaperPositionMode='auto';

print('Thomsen_parameter','-dpng','-r500')
```

```
%-------------------------------------------------------------------------
% Calculation of velocities and Plotting Figures Master Thesis Rebecca
Schlegel
%-------------------------------------------------------------------------

% Author: Rebecca Schlegel
% schlegel-rebecca@gmx.de

% Matlab 2016a
% Skript Version 1.1
% 2016 07 14


% calculate veolcity-depth and density-depth function using
% Herglotz-Wiechert inversion
% Script modified after Anja Diez
%Input: Traveltimes and Offsets of diving waves as well as
%'workspace_Herglotz_wiechert.mat' for comparison with other data
%Traveltime in sec and offset in m!!
%fit the following function to this curve and adopte the values of a-e
in
%the following script
% y=a*(1 - exp(-b*x)) + c*(1 - exp(-d*x)) + e*x
%-------------------------------------------------------------------------
% velo_depth_P=Matrix with velocity-depth values derived for the P wave
% velo_depth_SH=Matrix with velocity-depth values derived for the SH
wave
% velo_depth_SV=Matrix with velocity-depth values derived for the SV
wave
% rho_depth_P=Matrix with density-depth values derived for the P wave
% rho_depth_SH=Matrix with density-depth values derived for the SH wave
% rho_depth_SV=Matrix with density-depth values derived for the SV wave

%vp_FEA & vs_FEA=velocities derived from values of the algorithm for
depth_FEA

%vp_core&vs_core=velocities calculated by Kohnen's and Diez's formula
from
%XCT densities
%-------------------------------------------------------------------------


clear all, close all;
clf;

load('workspace_Herglotz_wiechert.mat')
%variables
deltax      = 0.01;              % steps in m for calculation of depth
and velocity
stop        = 320;              % should not be longer than biggest
offset
```

```
% Matrix with results, depth - velocity
res=zeros(stop+1,2);
rho=zeros(stop+1,1);


       a =     0.02056                    %(-0.5052, 0.5692)
       b =     0.0837                    %(-0.1819, 0.226)
       c =     0.08868                    %(-0.847, 1.013)
       d =    0.00406                      %(-0.1065, 0.1167)
       e =   0.0001661                    %(-0.001714, 0.002638)
% % vector with veolcities for different offsets
%
for i=1:1:(stop/deltax+1)
    j           = (i-1)*deltax;         % calculate j=offset to be able
to start at surface j=0
    offset(i)   = j;
    v(i)        = (a*b*exp(-b*j)+c*d*exp(-d*j)+e)^-1;
    % calculate apperent velocity from fitted curve
    av(i)       = j/(a*(1-exp(-b*j))+c*(1-exp(-d*j))+e*j);
    av(1) = 0;
end


% calculate depth z(v)

for i=1:1:(stop/deltax+1)
    Z       = 0;                % start depth for every ray
    % Summing up depth parts for one ray
    % only go to i-1
    for x=1:1:i-1
        dz      = (acosh(v(i)/av(x)))^-1*deltax;
        Z       = Z+dz;
    end
    z(i)        = 1/pi*Z;          % vector with results for depth
    % Matrix with velocity - depth pairs
    res(i,1)    = v(i);
    res(i,2)    = z(i);

    % calculate density rho(z)
    %rho(i,1)        = 0.915/(1+((1.96-v(i)/1000)/0.950)^1.17);
% using Anja Diez
     rho(i,1)        = 0.915/(1+((3.8-v(i)/1000)/2.25)^1.22);        %
using Kohnen
%     rholin(i,1)     = 0.221*v(i)/1000+0.059;
%using Robin linear
end

%%

%% Plot of velocities: The just calculated velocity is plotted together
with velocities calculated for Figure 5.17 on page 56
```

```
fig5=figure(5); %Figure 5.17; velocities
filler=fill([velo_depth_P(:,1)'-
delta_velo_depth_P(:,1)';velo_depth_P(:,1)'+delta_velo_depth_P(:,1)'],[
velo_depth_P(:,2)';velo_depth_P(:,2)'],'g','edgecolor','g','edgealpha',
0.08)
hold on
filler=fill([velo_depth_SV(:,1)'-
delta_velo_depth_SV(:,1)';velo_depth_SV(:,1)'+delta_velo_depth_SV(:,1)'
],[velo_depth_P(:,2)';velo_depth_P(:,2)'],'r','edgecolor','r','edgealph
a',0.08)

filler=fill([velo_depth_SH(:,1)'-
delta_velo_depth_SH(:,1)';velo_depth_SH(:,1)'+delta_velo_depth_SH(:,1)'
],[velo_depth_P(:,2)';velo_depth_P(:,2)'],'y','edgecolor','y','edgealph
a',0.08)

p30=plot(velo_depth_P(:,1),velo_depth_P(:,2),'Color',[0.2 0.8
0],'LineWidth',3)

p31=plot(velo_depth_SV(:,1),velo_depth_SV(:,2),'r','LineWidth',3)

p32=plot(velo_depth_SH(:,1),velo_depth_SH(:,2),'y','LineWidth',3)

p33=plot(vp_FEA,depth_FEA,'xc','LineWidth',3)

p_vp=errorbarxy(vp_FEA,depth_FEA, (delta_vp_FEA),[],{'ko', 'c', 'c'})

p34=plot(vs_FEA,depth_FEA,'xk','LineWidth',3)

p_vs=errorbarxy(vs_FEA,depth_FEA, (delta_vs_FEA),[],{'ko', 'k', 'k'})

p35=plot(v_p_core,Depth_i,'b','LineWidth',2)

p36=plot(v_s_core,Depth_i,'b','LineWidth',1)

p37=plot(v,z,'*','LineWidth',3)
grid on
xlabel('Velocity [m s^{-1}]','FontSize', 11);
ylabel('Depth [m]','FontSize', 11);
axis([0 4000 0 80])
set(gca,'YDir','reverse','FontSize',11,'FontName','arial')


h5_legend=legend([p30,p31,p32,p33,p34,p35,p36,p37],['P-wave
velocity'],...
     ['SV-wave velocity'],...
     ['SH-wave velocity'],...
     ['P-wave velocity' 10 'from component c_{33}'],...
     ['S-wave velocity' 10 'from component c_{55}'],...
     ['P-wave velocity' 10 'from XCT density'],...
     ['S-wave velocity' 10 'from XCT density'],...
     ['P-wave velocity' 10 'just derived']);
```

```
set(h5_legend,'FontSize',11);
h5_legend.Location='westoutside';

% fig5.Units='centimeters';
% fig5.Position=[20 10 17 8];
% fig5.PaperPositionMode='auto';
%
% print('velo_mit_legende','-dpng','-r500')
%%
figure(4)
plot(Density_i(:,1)/1000,Depth_i(:,1),'g','LineWidth',3)
hold on
plot(rho_depth_53(:,1),rho_depth_53(:,2),'k.','LineWidth',3)
plot(rho_depth_63(:,1),rho_depth_63(:,2),'r.','LineWidth',3)
plot(rho_depth_73(:,1),rho_depth_73(:,2),'b','LineWidth',3)
plot(rho,z,'b*','Markersize',3)
grid on
axis([0.2 0.9 0 80])
%title('Density with Depth')
xlabel('Density [g/cm^3]','FontSize', 11);
ylabel('Depth [m]','FontSize', 11);
legend('smoothed density XCT measurement','Density calculated from P-
wave velocity','Density calculated from SH-wave velocity','Density
calculated from SV-wave velocity','new calculated
density','location','southwestoutside')
set(gca,'YDir','reverse','FontSize', 11)
```